NATIONAL TECHNICAL UNIVERSITY OF ATHENS

SCHOOL OF CIVIL ENGINEERING

DEPARTMENT OF STRUCTURAL ENGINEERING

LABORATORY OF STRUCTURAL ANALYSIS AND ANTISEISMIC RESEARCH

SEISMIC PROTECTION OF STRUCTURES WITH NEGATIVE STIFFNESS DEVICES AND INERTANCE ELEMENTS

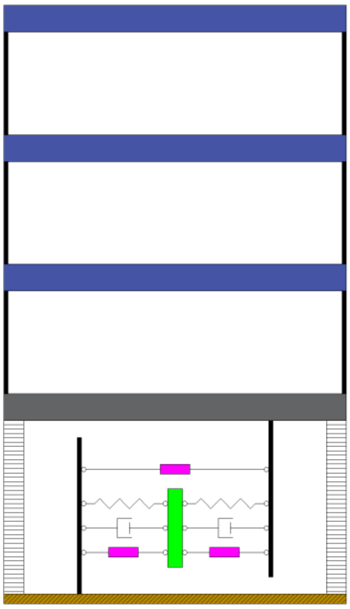

Postgraduate Thesis

Dimitrios N. Theodorou

Supervisor: Evangelos J. Sapountzakis, Professor and Vice Rector at NTUA

Co-supervisor: Konstantinos A. Kapasakalis, Postdoctoral Researcher at NTUA

Athens, June 2023

Δημήτριος Ν. Θεοδώρου

«Σεισμική προστασία των κατασκευών με συσκευές αρνητικής στιβαρότητας και στοιχεία αδρανείας»

Μεταπτυχιακή Εργασία

Εργαστήριο Στατικής και Αντισεισμικών Ερευνών, Εθνικό Μετσόβιο Πολυτεχνείο

Αθήνα, Ιούνιος 2023

Dimitrios N. Theodorou

“Seismic protection of structures with negative stiffness devices and inertance elements”

Postgraduate Thesis

Laboratory of Structural Analysis and Antiseismic Research, National Technical University of Athens

Athens, June 2023

Copyright © Δημήτριος Ν. Θεοδώρου, 2023
Με επιφύλαξη παντός δικαιώματος

Απαγορεύεται η αντιγραφή, αποθήκευση σε αρχείο πληροφοριών, διανομή, αναπαραγωγή, μετάφραση ή μετάδοση της παρούσας εργασίας, εξ ολοκλήρου ή τμήματος αυτής, για εμπορικό σκοπό, υπό οποιαδήποτε μορφή και με οποιοδήποτε μέσο επικοινωνίας, ηλεκτρονικό ή μηχανικό, χωρίς την προηγούμενη έγγραφη άδεια του συγγραφέα. Επιτρέπεται η αναπαραγωγή, αποθήκευση και διανομή για σκοπό μη κερδοσκοπικό, εκπαιδευτικής ή ερευνητικής φύσης, υπό την προϋπόθεση να αναφέρεται η πηγή προέλευσης και να διατηρείται το παρόν μήνυμα. Ερωτήματα που αφορούν στη χρήση της εργασίας για κερδοσκοπικό σκοπό πρέπει να απευθύνονται προς τον συγγραφέα. Η έγκριση της μεταπτυχιακής εργασίας από τη Σχολή Πολιτικών Μηχανικών του Εθνικού Μετσοβίου Πολυτεχνείου δεν υποδηλώνει αποδοχή των απόψεων του (Ν. 5343/1932, Άρθρο 202).

Copyright © Dimitrios N. Theodorou, 2023
All Rights Reserved

Neither the whole nor any part of this diploma thesis may be copied, stored in a retrieval system, distributed, reproduced, translated, or transmitted for commercial purposes, in any form or by any means now or hereafter known, electronic or mechanical, without the written permission from the author. Reproducing, storing and distributing this thesis for non-profitable, educational or research purposes is allowed, without prejudice to reference to its source and to inclusion of the present text. Any queries in relation to the use of the present thesis for commercial purposes must be addressed to its author. Approval of this postgraduate thesis by the School of Civil Engineering of the National Technical University of Athens (NTUA) does not constitute in any way an acceptance of the views of the author contained herein by the said academic organization (L. 5343/1932, art. 202).

"We can do little to reduce the hazard embodies in an active fault or a major earthquake, but we can do a lot about the risk to the structures that we design and build. It is important to remember the frequently quoted observation that earthquakes do not kill, but collapsed buildings and facilities do."

Professor Thomas Denis O'Rourke, Cornell University

ACKNOWLEDGEMENTS

The writing of this thesis marks the end of my postgraduate studies at the School of Civil Engineering of the National Technical University of Athens. Throughout the two years of my studies, I came into contact with professors, who taught very interesting courses and instilled me the value of the civil engineering profession and the important role it plays in shaping and maintaining the function of our society. I feel obliged to acknowledge all those people who helped me complete my studies.

First of all, I would like to express my heartfelt gratitude to Professor and Vice Rector at the National Technical University of Athens, Dr. Sapountzakis Evangelos for his invaluable guidance and unwavering support throughout my thesis journey. His expertise, profound knowledge and insightful feedback have been instrumental in shaping the direction of my research. Dr. Sapountzakis' dedication to academic excellence and his passion for the subject I investigated have been truly inspiring. His mentorship has, not only enriched my understanding of the field, but has also encouraged me to push the boundaries of my own capabilities. I am immensely grateful for the time and effort he has invested in me, providing valuable guidance, encouragement and constructive criticism that have greatly contributed to the successful completion of this thesis.

I would also like to express my sincere appreciation to Konstantinos Kapasakalis, Postdoctoral Researcher at the National Technical University of Athens, for his valuable contributions and collaboration throughout my research journey. His expertise, enthusiasm and willingness to share knowledge have been instrumental in enhancing the quality and depth of my work. His insightful discussions, constructive feedback, and technical assistance have significantly contributed to the advancement of my research. I am grateful for his willingness to spare his time and share his expertise, which has played a crucial role in the success of this thesis.

I would also desire to acknowledge the two members of the examination committee. I am sincerely grateful to Dr. Savvas Triantafyllou, Assistant Professor at the National Technical University of Athens, for his expertise and valuable insights. I am honored to have had the opportunity to benefit from his extensive knowledge and guidance and have fruitful conversations that assisted my overall academic course. Moreover, I would like to appreciate the effort of Dr. Ioannis Antoniadis, Professor at the National Technical University of Athens, for the initial conceptualization of the KDamper, which stood the key point for the takeover and completion of this thesis.

I am profoundly grateful to my friends for their unwavering support, encouragement, and invaluable presence throughout my thesis journey.

Finally, I would like to express my deepest gratitude to my family for their unconditional support, love and belief in me throughout this thesis journey. Their constant encouragement, understanding and sacrifices have been the foundation of my success and I am forever grateful.

CONTENTS

LIST OF FIGURES

LIST OF TABLES

ΠΕΡΙΛΗΨΗ

Στην παρούσα μεταπτυχιακή εργασία, προτείνονται διάφορες διευρυμένες εκδόσεις του συστήματος Stiff Base Absorber (SBA), το οποίο βασίζεται στον ταλαντωτή KDamper, οι οποίες ενσωματώνουν στοιχεία αδρανείας σε διάφορες θέσεις, εκτός άλλων στοιχείων θετικής και αρνητικής στιβαρότητας και τεχνητών αποσβεστήρων. Οι βέλτιστες παράμετροι του συστήματος, σε κάθε περίπτωση, προσδιορίζονται με την επίλυση ενός προβλήματος βελτιστοποίησης και την αξιολόγηση των περιορισμών με βάση μηχανικά κριτήρια. Τα προτεινόμενα συστήματα απορρόφησης ταλαντώσεων σχεδιάζονται ως διευρυμένες εκδόσεις σεισμικής βάσης απορρόφησης ταλαντώσεων (ESBA) και προστίθεται ένα φίλτρο επιτάχυνσης ως περιορισμός για την καλύτερη παρατήρηση της απόδοσης του συστήματος. Έτσι, οι βέλτιστες παράμετροι επιλέγονται με βάση τη μέγιστη επιτάχυνση της κατασκευής, εκφρασμένη ως ποσοστό της μέγιστης εδαφικής επιτάχυνσης (PGA). Για τον καθορισμό του φίλτρου επιτάχυνσης, δημιουργείται μια βάση δεδομένων τεχνητών επιταχυνσιογραφημάτων συμβατών με τα φάσματα απόκρισης του EC8. Στη συνέχεια χρησιμοποιούνται πραγματικές καταγραφές σεισμών για την αξιολόγηση της δυναμικής συμπεριφοράς ενός μονοβαθμίου συστήματος (SDoF). Το μονοβάθμιο σύστημα συγκρίνεται με ένα αντίστοιχο σύστημα συμβατικής μόνωσης βάσης χαμηλής και υψηλής απόσβεσης. Στη συνέχεια, το πιο αποδοτικό από τα προτεινόμενα συστήματα ελέγχου ταλαντώσεων επεκτείνεται για εφαρμογή ως σεισμική βάση για πολυώροφες κατασκευές. Οι παράμετροι του συστήματος επιλέγονται από το προαναφερθέν πρόβλημα βελτιστοποίησης. Πιο συγκεκριμένα, ορίζονται και συγκρίνονται οι δυναμικές αποκρίσεις ενός τριώροφου και ενός πενταώροφου κτιρίου, που μοντελοποιούνται ως διατμητικά πλαίσια, στα ακόλουθα σενάρια: τα κτίρια θεωρούνται αρχικά πακτωμένα στο έδαφος, στη συνέχεια εδράζονται στην προτεινόμενη βάση απορρόφησης ταλαντώσεων και αργότερα, αντιπαραβάλλονται με το σενάριο να εδράζονται σε συμβατική μόνωση βάσης χαμηλής και υψηλής απόσβεσης, με την ίδια ή διαφορετική ιδιοσυχνότητα, ώστε να αποδειχθεί η αποτελεσματικότητα του προτεινόμενου συστήματος σεισμικής βάσης. Όλα τα κτίρια πολλαπλών βαθμών ελευθερίας (MDoF) υποβάλλονται σε τεχνητές και πραγματικές κοντινές ή απόμακρες σεισμικές διεγέρσεις. Πραγματοποιούνται αναλύσεις ευαισθησίας, εξετάζοντας, πρώτον, τη μεταβολή μιας παραμέτρου κάθε φορά και, δεύτερον, δύο παραμέτρων ταυτόχρονα, για να διερευνηθεί κατά πόσον το προτεινόμενο σύστημα ελέγχου ταλαντώσεων είναι ευάλωτο ή όχι σε φαινόμενα αποσυντονισμού. Τέλος, υιοθετείται μια ρεαλιστική διαμόρφωση εξαρτώμενη από τη μετατόπιση για την υλοποίηση του στοιχείου αρνητικής στιβαρότητας και συγκρίνεται η μη γραμμική δυναμική συμπεριφορά του συστήματος με την αρχικά αναμενόμενη γραμμική. Παρατίθεται ένας ενδεικτικός σχεδιασμός του προτεινόμενου συστήματος απορρόφησης ταλαντώσεων όσον αφορά τα στοιχεία που περιλαμβάνει. Εξάγονται διάφορα συμπεράσματα σχετικά με την αποτελεσματικότητα των προτεινόμενων συστημάτων απορρόφησης ταλαντώσεων.

ABSTRACT

In this postgraduate thesis, several extended versions of the Stiff Base Absorber system (SBA), which relies on the KDamper oscillator, are proposed that incorporate inerter elements in various locations. The optimal system parameters, in each case, are determined by solving an optimization problem and evaluating the constraints based on engineering criteria. The proposed dynamic vibration absorbers are designed as extended seismic base absorbers (ESBA) and an acceleration filter is added as a constraint to better observe the system's efficiency. Thus, the optimal parameters are selected based on the maximum structure acceleration expressed as a percentage of PGA. To define the acceleration filter, a data-base of artificial accelerograms compatible with the EC8 response spectra is generated. Real earthquake records are then used to evaluate the SDOF system dynamic behavior. The SDoF system is compared to a corresponding SDoF system of a conventional low and high damping base isolation system. Subsequently, the most efficient of the proposed vibration control systems is extended for implementation as a stiff seismic base absorber for multistory structures. The system parameters are selected from the previously stated optimization problem. More specifically, the dynamic responses of a three-story and a five-story buildings, modeled as shear frames, are defined and compared in the following scenarios: the buildings are firstly considered fixed on the ground, then they lie on the proposed vibration absorption base and finally, are contrasted with the scenario of them being mounted on a low and high damping conventional seismic isolation bases, with the same or different natural frequency, to prove the efficiency of the proposed extended stiff seismic base absorber. All the multi degree of freedom (MDoF) buildings are subjected to the artificial and the real near-fault and far-fault earthquake excitations. Sensitivity analyses are performed, by considering: i) the variation of one parameter at a time and secondly, and ii) two parameters simultaneously, to investigate whether the proposed vibration control system is vulnerable or not to detuning phenomena. Finally, a realistic displacement-dependent configuration for the realization of the NS element is adopted and the non-linear dynamic behavior of the system is compared with the initially expected linear one. An indicative design of the proposed vibration absorption system is presented concerning its comprising elements. Several conclusions are drawn regarding the efficiency of the proposed extended stiffness base absorbers.

1 INTRODUCTION

1.1 Statement of the problem

This thesis focuses on protecting civil engineering structures against environmental excitations. The research primarily investigates the absorption of vibrations resulting from environmental excitations, such as seismic events and wind loads. The objective is to enhance the dynamic behavior of each structural system, ensuring its resilience and preventing collapse under extreme conditions that exceed its load-bearing capacity or due to fatigue, caused by seismic events or aerodynamic loads.

In recent years, the devastating impact of seismic events, especially in densely populated areas located in earthquake-prone regions, has prompted revisions in the anti-seismic codes and regulations for buildings (Warn & Ryan, 2012), (Reggio & Angelis, 2015) and (Kangda & Bakre, 2020), bridges (Kunde & Jangid, 2003) and infrastructure or industrial facilities (De Angelis, Giannini, & Paolacci, 2010), (Paolacci, Giannini, & De Angelis, 2013) and (WHITTAKER & KUMAR, 2014). The revised approach emphasizes designing structures with superior seismic performance. Concerning the horizontal component of seismic excitations, seismic base isolation has emerged as a favorable alternative to conventional anti-seismic techniques (Kelly J. M., 1986). Unlike traditional approaches that focus on strengthening structures, seismic isolation aims to mitigate seismic loads by introducing a laterally low-stiffness flexible layer between the structure and its foundation. By doing so, the fundamental period of the seismically isolated system significantly increases, leading to reduced forces and accelerations affecting the structure. This can be clearly observed through (Fig. 1.1(a)), as the acceleration (and subsequently the earthquake induced loads) decrease with an increase of the period. The structure, with its lowered fundamental period lies on the descending branch of the acceleration response spectrum. Various types of isolation devices, ranging from simple elastomeric bearings or laminated rubber bearings with or without lead core (Naeim & Kelly, 1999) to more complex configurations including sliding/frictional bearings (Fenz & Constantinou, 2006) have been developed over time to achieve effective seismic isolation, as depicted in (Fig. 1.2(a) and (b)).

However, it is important to note that implementing seismic isolation at the base of structures unavoidably results in significant displacements during seismic events, as it can be seen in (Fig. 1.1(b)). By providing flexibility at the base of the structure, this leads on the increase of the period, which results in the increase of the displacements, as the structure, now, is located on the ascending branch of the equivalent-to-the-acceleration displacement response spectrum. This characteristic may not be desirable in all cases due to factors such as the sensitivity of seismically isolated structures to wind loads, specific requirements for water supply, heating and drainage systems or gas fittings or electrical conduits within the structures, as well as the need for adequately sized seismic joints to prevent collisions between neighboring buildings. Consequently, the application of seismic isolation might not be suitable for existing structures, as a retrofitting technique. Nevertheless, there have been successful implementations of devices that provide protection against the horizontal seismic forces in various construction projects.

Increasing the damping coefficient ζ of the base isolation system or introducing additional dampers within the structure to mitigate excessive displacements is not commonly considered as a primary alternative (Symans et al., 2008). This is due to the significant technological demands imposed on the corresponding devices in terms of the size requirements. Furthermore, directly augmenting the damping coefficient leads to amplified interstory drifts and floor accelerations (Kelly J. M., 1999).

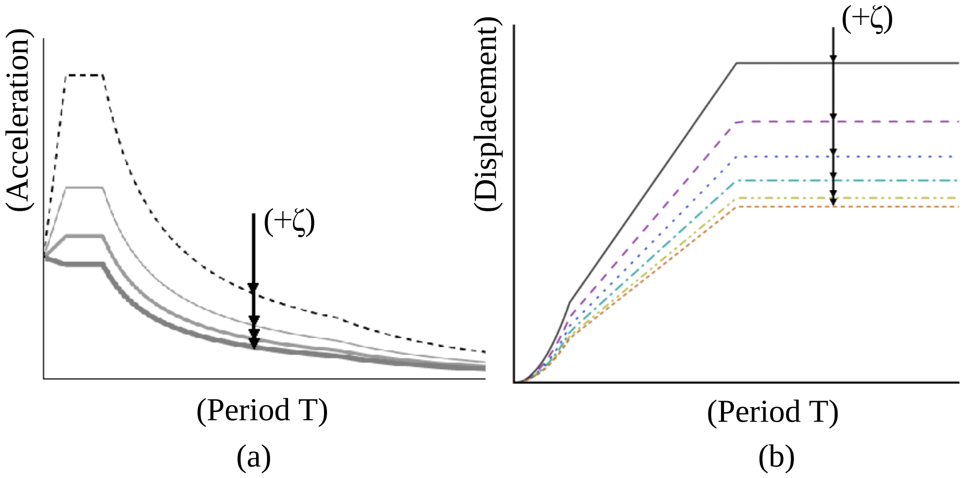

Figure 1.1: Schematic representation of the response spectra in terms of (a) acceleration and (b) displacement and their variation due to damping increase

(a) (b)

Figure 1.2: Base isolation including (a) elastomeric bearings and (b) sliding bearings

In an attempt to overcome the drawbacks of the conventional base isolation and simultaneously maintain the beneficial characteristics of it, various vibration absorption systems have been proposed that are based on the following concepts:

- Quasi Zero Stiffness oscillators (QZS)
- Tuned Mass Dampers (TMD) (Fig. 1.3(a))
- Inerters
- Negative Stiffness vibration systems (KDamper) (Fig. 1.3(b))

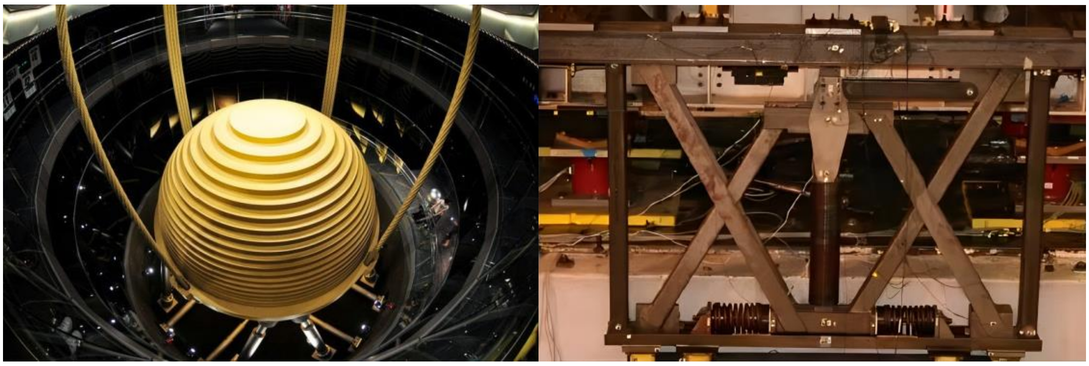
(a) (b)

Figure 1.3: (a) Tuned Mass Damper and (b) KDamper configuration

1.2 Scope of the thesis and methodology

In the present thesis a novel vibration absorption system is proposed, that is based on previous KDamper designs. More specifically, three extended versions of the Stiff Base Absorber (SBA) from (Kapasakalis, Antoniadis, & Sapountzakis, 2022), (ESBA1 to ESBA3) are investigated, which incorporate multiple inerter elements located in various positions, in an attempt to maximize the dynamic performance of these systems. Moreover, the proposed configurations include positive and negative stiffness elements, damping coefficients that are parallel to the stiffness elements and an additional oscillating mass. Thus, the equations of motion, in each case, emerge with their respective free design variables and the formation of an optimization procedure is imperative in order to select the best values that fit to the parameters of the systems. The optimization is configured in a way to follow some imposed constraints and limitations so that a technologically feasible design of the proposed vibration absorption systems can be implemented and their components can lie within realizable limits that can meet engineering and constructional criteria. In this procedure, the variation of all the stiffness elements is foreseen to lead to a realistic design of the proposed systems. The earthquake input motion is selected to be in accordance with the current antiseismic codes, via artificial accelerograms that are compatible with the EC8 acceleration response spectra. Then, a single degree of freedom system (SDoF), controlled by the most efficient vibration absorption system, as indicated by the optimization process, is chosen to be evaluated by an artificial acceleration and real earthquake excitations. The same configuration can be eventually considered as a vibration absorption base for multistory structures. The dynamic performance of both the superstructure and the base can be assessed from the same artificial and real earthquake motions. At the same time, the dynamic performance of the SDoF system and the multistory structure is compared with that of a low damping and high damping conventional base isolation. In addition, sensitivity analyses can be performed to check whether the proposed system is susceptible to detuning phenomena or not. A displacement-based configuration is adopted for the realization of the negative stiffness element and the non-linear dynamic behavior of the system is compared with the initially expected linear one. Finally, an indicative design of the proposed vibration absorption system is listed in terms of all the consisting elements.

A more thorough explanation of the concepts concerning the existing and the proposed vibration absorption systems is involved in the next chapters. Various MATLAB (The MathWorks Inc., 2022) scripts, containing algorithms, regarding the optimization process and the solving of equations of motion, were formed.

1.3 Thesis outline

After this introduction, the present thesis is structured as follows:

- Chapter 1 includes the statement of the problem, regarding the advantages and drawbacks of the conventional base isolation system and the proposal of novel vibration absorption systems in an attempt to maintain the advantages and mitigate the disadvantages of it.
- Chapter 2 involves a brief overview of the Quasi Zero Stiffness (QZS) oscillator, the Tuned Mass Damper (TMD) and the Tuned Mass Damper with Inerters (TMDI)
- Chapter 3 contains a short outline of the negative stiffness vibration absorption systems of the KDamper, an extended version of it (EKD) and a further extension of it with an inerter, the Stiff Base Absorber (SBA)
- Chapter 4 covers the proposal of three extended versions of the Stiff Base Absorber (ESBA1 to ESBA3), in terms of the formation of the equations of motion, the statement of the optimization problem with the corresponding algorithm, the imposed constraints, the artificial earthquake excitation and the algorithm that solves the equations of motion, the results of the optimization procedure and the dynamic performance of an SDoF, system controlled by the most efficient system of the proposed configurations, by an artificial and real earthquake excitations, compared to low and high damping conventional base isolation systems
- Chapter 5 encompasses the dynamic performance of a three-story and five-story building, at first, considered fixed on the ground and subsequently mounted on the same, as in Chapter 4, proposed vibration absorption base system and is compared to that of the low and high damping conventional base isolation
- Chapter 6 includes the sensitivity analyses, with respect to one at a time or two simultaneously altering parameters, to check the detuning phenomena, the negative stiffness element configuration that generates a nonlinear response and

a comparison of it with the initial expected linear one and the realization of the proposed vibration absorption base

- Chapter 7 list the conclusions of this work and mentions some future research extensions of the present thesis

2 OVERVIEW OF CONVENTIONAL VIBRATION ABSORBERS

2.1 Quasi Zero Stiffness (QZS) oscillators

True negative stiffness refers to a force that assists motion rather than opposing it, similar to a positive stiffness spring. This can be schematically seen in the figure (2.1) below.

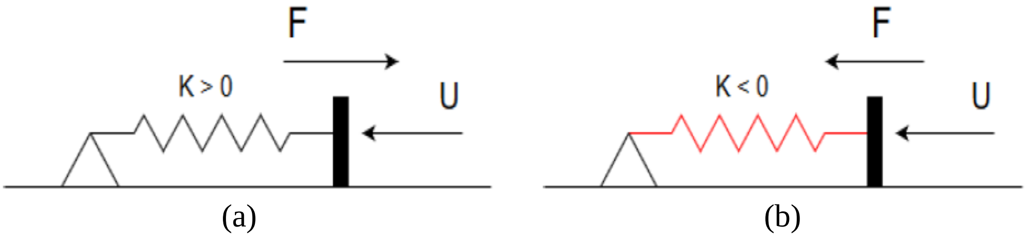

(a) (b)

Figure 2.1: Schematic presentation of (a) a positive stiffness element and (b) a negative stiffness element

The utilization of negative stiffness elements, also known as anti-springs, for vibration isolation was initially introduced by (Molyneux, 1957) and further developed by (Platus, 1992). These approaches revolve around the idea of significantly reducing the stiffness of the isolator, leading to a decrease in the system's natural frequency (resulting in an increase of the natural period), even approaching near-zero levels as demonstrated in (Carrella, Brennan, & Waters, 2007). Such systems are referred to as Quasi Zero Stiffness (QZS) oscillators. This design approach enhances vibration absorption by reducing transmissibility for frequencies above the natural frequency. Numerous researchers have validated the effectiveness of these devices through numerical simulations and experimental testing, as comprehensively reviewed by (Ibrahim, 2008).

(Nagarajaiah et al., 2013) introduced a novel structural modification approach for seismic protection, employing an adaptive negative stiffness device that reduces dynamic forces imposed on the structure. To mitigate the concurrent growth of structural displacements, a damper is placed in parallel with the negative stiffness device.

Achieving negative stiffness behavior primarily involves special mechanical designs that incorporate conventional pre-stressed elastic elements with positive stiffness, such as post-buckled beams, plates, shells and pre-compressed springs. (Winterflood, Blair, & Slagmolen, 2002) and (Virgin, Santillan, & Plaut, 2008) describe some interesting designs in this regard. However, in addition to elastic forces, other physical forces, such as gravitational (Dyskin & Pasternak, 2012), magnetic (Robertson, Kidner, Cazzolato, & Zander, 2009) or electromagnetic (Zhou & Liu, 2010) forces can be utilized to create an equivalent negative stiffness effect. However, for seismic mitigation in buildings or bridge structures that require substantial negative stiffness values, elastic forces appear to be the most viable choice. Quasi-Zero Stiffness (QZS) oscillators have found extensive applications in seismic isolation (Attary, Symans, & Nagarajaiah, 2015), automotive suspensions (Lee & Goverdovskiy, 2012) and torsional vibrations (Zhou, Xu, & Bishop, 2015).

Moreover, materials containing a negative stiffness phase (Lakes, 2001) have also demonstrated significant damping capabilities, both at the material (Jaglinski, Kochmann, Stone, & Lakes, 2007) and in macroscopic devices (Dong & Lakes, 2013). This behavior can be combined with high stiffness properties.

Considering a structure with mass m, stiffness k and damping coefficient c_D, the concept of a simple QZS oscillator, presented in Figure (2.2), is to add a negative stiffness (NS) element k_N in parallel to the conventional positive stiffness element k. The equation of motion of the Quasi Zero Stiffness (QZS) oscillator becomes:

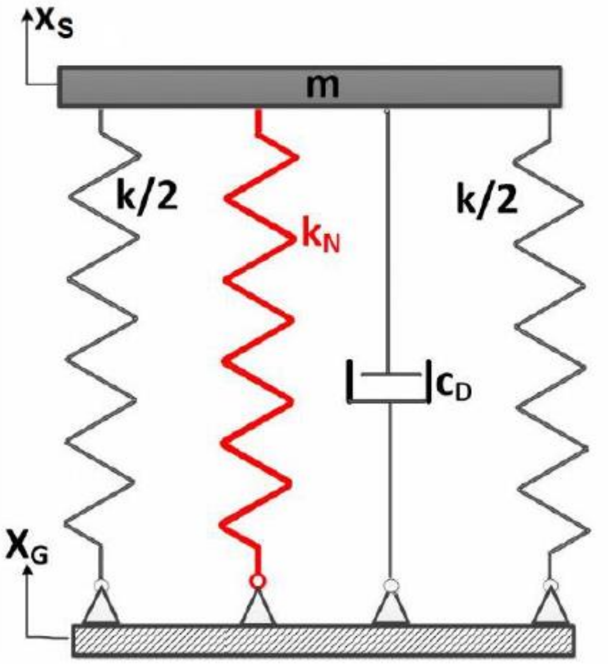

Figure 2.2: Schematic presentation of a Quasi Zero Stiffness oscillator (QZS)

$$m\ddot{u}_S + c_D\dot{u}_S + (k + k_N)u_S = m\ddot{u}_S + c_D\dot{u}_S + k_{QZS}u_S = -m\ddot{x}_g \qquad (2.1)$$

where $u_S = x_S - x_g$ is the relative to the ground displacement and x_g is the ground excitation. From equation (2.1), it is obvious that the overall static stiffness of the system is reduced, since the negative stiffness element has a negative value ($k_{QZS} < k$ since $k_N < 0$). This correspondingly reduces the natural frequency of the system (or equivalently increases its natural period). As a result, the seismic forced and subsequently the accelerations are reduced. However, this limits the static loading capacity of the structure, which may result to unsolvable problems, especially for vertical vibration isolation.

2.2 Tuned Mass Dampers (TMD)

Among the various control techniques for vibration mitigation, one widely utilized and well-established approach is the incorporation of an additional mass known as a Tuned Mass Damper (TMD). A TMD, also referred to as a dynamic vibration absorber, consists of a mass, a spring, and a viscous damper. Typically, it is installed on a vibrating primary system to suppress undesirable vibrations caused by wind and seismic loads. The concept of TMD was initially introduced by (FRAHM, Patent No. 0989958, 1911) and after the optimization theory for designing TMD systems, proposed by (Den Hartog, 1956), it has been extensively employed in numerous systems. Notably, TMDs have found application in skyscrapers, with examples including the renowned Taipei 101 Tower in Taiwan (Haskett, Breukelman, Robinson, & Kottelenberg, 2003), one of the tallest buildings globally (Fig. 2.3).

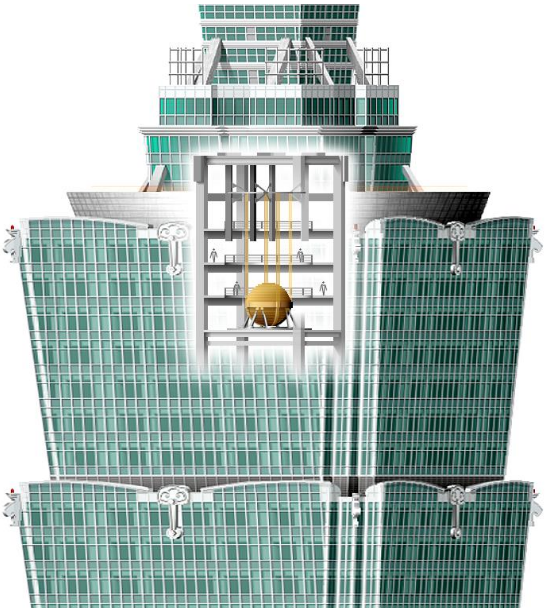

Figure 2.3: Tuned Mass Damper (TMD), installed on top of the Taipei 101 Tower in Taiwan

The basic principle of operation of TMDs is to reduce the displacements of a structure by transferring energy to a vibrating system consisting of an additional mass, designed with appropriate characteristics and placed at a suitable location within the structure. The TMD, as mentioned before, typically consists of an additional mass (which constitutes a small percentage of the total mass) and a spring combined with an artificial damper. The values and parameters related to the design of such devices depend on both the desired results in the final dynamic response of the structure and the tuning of the TMD frequency to match the fundamental frequency of the original structure. This characteristic allows a significant amount of the structural vibration energy, due to seismic motion, to pass through the structure into the additional mass of the device and then dissipate through the damper.

Despite being known for their effectiveness and reliability, the main drawback of these devices is their sensitivity to the parameters that characterize them. Environmental and other external factors can easily disrupt these parameters, negatively affecting the device's performance and consequently, the response of the structure. The difficulty in constructing and placing the large additional masses required to achieve significant reduction in imposed seismic vibrations further limits their usage. The concept of TMD is illustrated in the following figure (2.4).

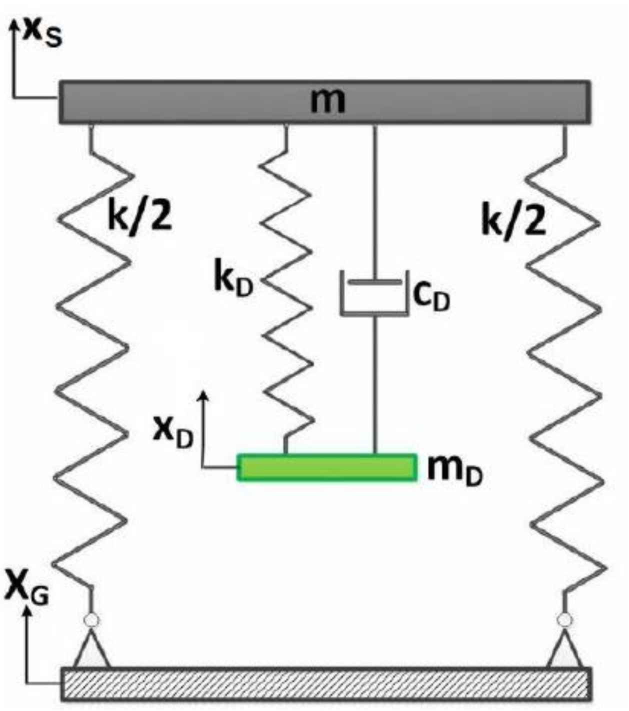

Figure 2.4: Schematic presentation of a Tuned Mass Damper (TMD)

The resulting equations of motion are listed below:

$$m\ddot{u}_S + c_D(\dot{u}_S - \dot{u}_D) + k_D(u_S - u_D) + ku_S = -m\ddot{x}_g \tag{2.2a}$$

$$m_D\ddot{u}_D - c_D(\dot{u}_S - \dot{u}_D) - k_D(u_S - u_D) = -m_D\ddot{x}_g \tag{2.2b}$$

Regarding the optimal design of TMD, various approaches can be found in the literature, depending on the specific problem. A common practice is to tune the TMD to the fundamental frequency of the original system, and then numerically calculate the damping ratio.

2.3 Inerters and Tuned Mass Damper Inerters (TMDI)

In an effort to reduce the requirements for large additional mass, the principle of the inerter was introduced by (Smith, 2002), in the early 2000s. The inerter is a two-terminal device that generates a force proportional to the relative acceleration across its terminals. This proportionality constant is called "inertance" and is measured in kilogram units. The main advantage of the inerter is that it does not need to have a large mass to achieve the same inertial effect as the additional mass in the TMD.

An illustrative application of the inerter is shown in Figure (2.5). In this arrangement, the inerter connects the mass of the structure directly to the base. This reduces the natural frequency of the system and consequently, the seismic loads without reducing the load-carrying capacity of the structure or introducing additional masses.

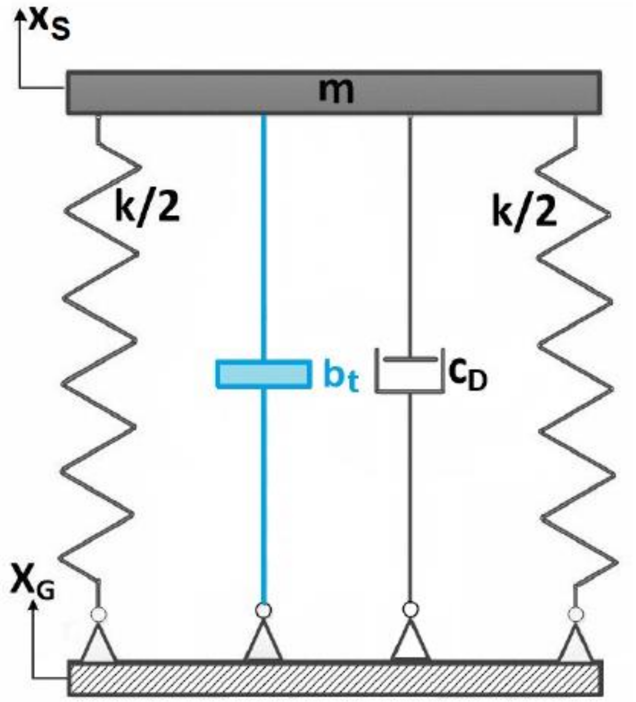

Figure 2.5: Schematic presentation of the inerter damper

The equation of motion for this system is as follows:

$$(m + b_t)\ddot{u}_S + c_D\dot{u}_S + ku_S = -m\ddot{x}_g \tag{2.3}$$

where b_t is the inertance.

Recently, the combination of TMD with an inerter (TMDI) has been proposed (De Domenico, Impollonia, & Ricciardi, 2018). In this arrangement, the additional mass of the TMD is connected to the base through an inerter. This way, the inertial force of the additional mass is increased without increasing the mass itself. The TMDI configuration is shown in Figure (2.6). However, proposed TMDs with inerters suffer from susceptibility to detuning.

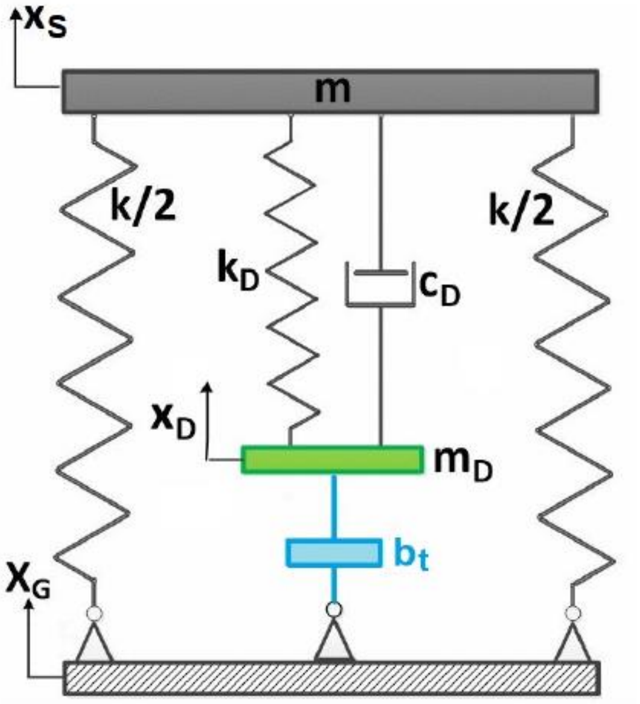

Figure 2.6: Schematic presentation of the Tuned Mass Damper with Inerter (TMDI)

The equations of motion, now, are the following:

$$m\ddot{u}_S + c_D(\dot{u}_S - \dot{u}_D) + k_D(u_S - u_D) + ku_S = -m\ddot{x}_g \tag{2.4a}$$

$$(m_D + b_t)\ddot{u}_D - c_D(\dot{u}_S - \dot{u}_D) - k_D(u_S - u_D) = -m_D\ddot{x}_g \tag{2.4b}$$

3 NEGATIVE STIFFNESS KDAMPER-BASED DYNAMIC VIBRATION ABSORBERS

3.1 The KDamper concept

A promising group of absorbers relies on enhancing damping through the strategic inclusion of negative stiffness components. Taking advantage of the benefits offered by the traditional Tuned Mass Dampers (TMD) and the Quasi Zero Stiffness (QZS) oscillators, a novel concept for passive vibration absorption and damping, known as the KDamper concept, was introduced by (Antoniadis, Kanarachos, Gryllias, & Sapountzakis, 2018). The KDamper incorporates a negative stiffness element known for its exceptional damping properties, while avoiding the drawbacks associated with traditional linear oscillators or zero-stiffness designs. The overall static stiffness of the KDamper is designed to be similar to that of a conventional reference oscillator. However, it differs from both the original single-degree-of-freedom (SDoF) oscillator and existing negative stiffness oscillators through the strategic redistribution of individual stiffness elements and damping reallocation. Despite the inclusion of a negative stiffness element, the proposed oscillator is designed to ensure static and dynamic stability. Additionally, the presence of an additional mass helps mitigate the effects of vibrating loads by acting as an energy dissipation mechanism, transferring energy from the structure to the added mass. The KDamper overcomes the sensitivity issues associated with Tuned Mass Dampers, as the tuning is primarily controlled by the parameters of the negative stiffness element.

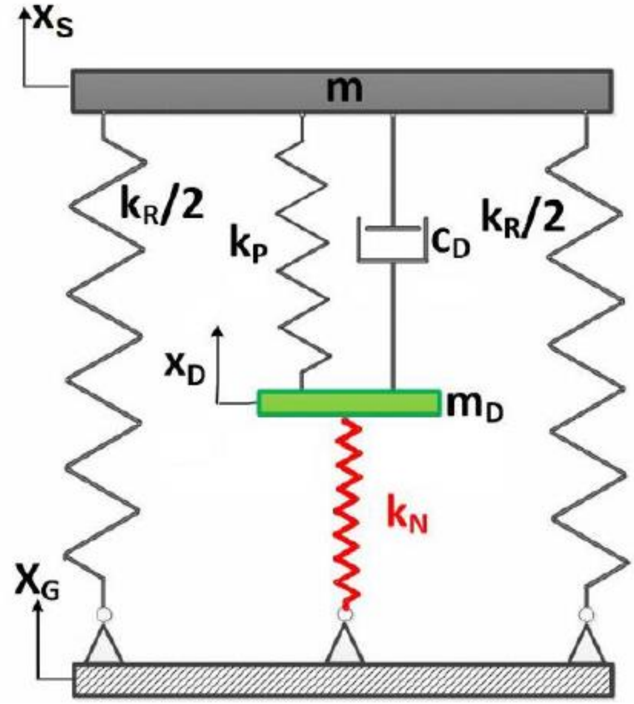

Figure 3.1: Schematic presentation of the KDamper vibration absorption system

The KDamper has been effectively implemented in multistory buildings as a base absorption system (Kapasakalis, Antoniadis, & Sapountzakis, Implementation of the KDamper as a Stiff Seismic Absorption Base: A Preliminary Assessment, 2019) and has been compared to conventional base isolation systems (Kapasakalis, Antoniadis, & Sapountzakis, Performance assessment of the KDamper as a seismic Absorption Base, 2019).

As it can be clearly observed in the schematic presentation of the KDamper concept in (Fig. 3.1), similarly to the QZS oscillator, there is a negative stiffness element. However, contrary to the QZS isolator, the first basic requirement of the KDamper is that the overall static stiffness of the system is maintained. Thus, The KDamper concept effectively addresses the inherent drawback of negative stiffness (NS) isolators. Moreover, compared to the TMD, the negative stiffness element connects the additional oscillating mass to the base. In this way, the KDamper achieves the vibrations control with relatively small values of the additional mass. The equations of motion of this system become:

$$m\ddot{u}_S + c_D(\dot{u}_S - \dot{u}_D) + k_P(u_S - u_D) + k_R u_S = -m\ddot{x}_g \tag{3.1a}$$

$$m_D\ddot{u}_D - c_D(\dot{u}_S - \dot{u}_D) - k_P(u_S - u_D) + k_N u_D = -m_D\ddot{x}_g \tag{3.1b}$$

3.2 Extended version of the KDamper concept

The next dynamic vibration absorption system is an extension of the KDamper concept and thus, it is called extended KDamper (EKD system). Similar to the KDamper, the EKD incorporates a combination of masses, negative stiffness, positive stiffness elements and artificial dampers. The main difference lies in the system configuration, where the positive stiffness spring (k_{PS}) connects the damper mass (m_D) to the system's base, while the negative stiffness element (k_{NS}) is connected between the damper mass (m_D) and the oscillating mass (m). Additionally, an extra artificial damper is introduced in parallel with the negative stiffness element, resulting in two dampers, namely c_{NS} and c_{PS}. Utilizing the original formulation of the KDamper expressions (Equations (3.1)), the following equations of motion for the EKD system are derived as follows, according to the figure (3.2):

$$m\ddot{u}_S + c_{NS}(\dot{u}_S - \dot{u}_D) + k_{NS}(u_S - u_D) + k_R u_S = -m\ddot{x}_g \tag{3.2a}$$

$$m_D\ddot{u}_D - c_{NS}(\dot{u}_S - \dot{u}_D) - k_{NS}(u_S - u_D) + c_{PS}\dot{u}_S + k_{PS}u_D = -m_D\ddot{x}_g \tag{3.2b}$$

Since the EKD system is an extension of the classical KDamper concept, it is anticipated that the vibration control strategy implemented with the EKD system will yield similar effects to those observed with the KDamper in terms of controlling the dynamic behavior of the system. The configuration of the EKD system aims to ensure that the displacements and velocities of the internal degrees of freedom (DoFs) remain within reasonable limits. This design approach aims to strike a balance between practicality and efficiency, allowing for a realistic and effective implementation.

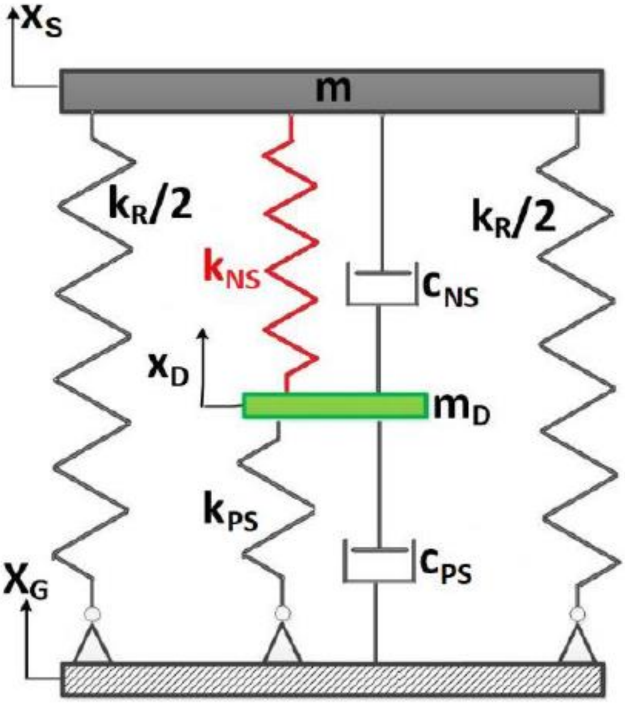

Figure 3.2: Schematic presentation of the extended KDamper concept (EKD system)

The EKD has been successfully implemented as a seismic base absorber of multi-story building structures (Kapasakalis, Antoniadis, & Sapountzakis, Constrained optimal design of seismic base absorbers based on an extended KDamper concept, 2021), without or by including the effect of the Soil-Structure Interaction (SSI) for various soil categories (Kapasakalis, Antoniadis, & Sapountzakis, A Soil-Dependent Approach for the Design of Novel Negative Stiffness Seismic Protection Devices, 2021), or by adopting an extreme geometrical nonlinear configuration for the realization of the negative stiffness element (Kapasakalis & Sapountzakis, Vibration Absorption using KDamper-based Devices with Extreme Geometric Nonlinearity,, 2022), or as a seismic retrofitting measure for typical RC residential buildings (Kapasakalis, Alvertos, Antoniadis, & Sapountzakis, 2022) and finally as a system for vibration mitigation of a monopile Offshore Wind Turbine (OWT) (Kampitsis, Kapasakalis, & Via-Estrem, 2022).

3.3 Extension of KDamper Equipped with Inerter

In figure (3.3), there is an extension of the KDamper, the EKD system, as analyzed in the previous section 3.2, by introducing an inerter, which directly connects the structure to the ground. This leads to a decrease in the natural frequency (f_0) of the system, thereby reducing the seismic load on the structure without lessening its stiffness or increasing its actual mass. Simultaneously, the EKD system is implemented to effectively control the significant relative displacements of the structure by enhancing the overall damping.

The EKD system, with the incorporation of an inerter, has been investigated as a vibration control base for multistory structures, called as Stiff Base Absorber (SBA), in the work of (Kapasakalis, Antoniadis, & Sapountzakis, 2022), as a method for the vertical component of earthquake excitations (Kapasakalis, Antoniadis, & Sapountzakis, STIFF vertical seismic absorbers, 2021) and (Kalogerakou, Kapasakalis, Antoniadis, & Sapountzakis, 2023) and as a vibration mitigation approach for Wind Turbine towers (WT) in the study of (Kapasakalis K. A., Antoniadis, Sapountzakis, & Kampitsis, Vibration Mitigation of Wind Turbine Towers Using Negative Stiffness Absorbers, 2021).

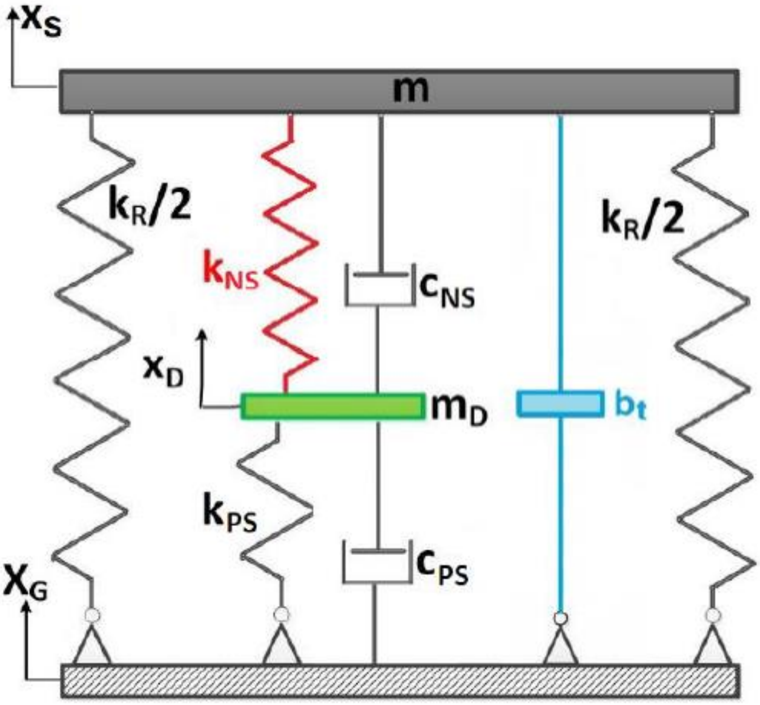

Figure 3.3: Schematic presentation of the Stiff Base Absorber (SBA system)

Thus, the equations of motion of this system are the following:

$$(m + b_t)\ddot{u}_S + c_{NS}(\dot{u}_S - \dot{u}_D) + k_{NS}(u_S - u_D) + k_R u_S = -m\ddot{x}_g \tag{3.3a}$$

$$m_D\ddot{u}_D - c_{NS}(\dot{u}_S - \dot{u}_D) - k_{NS}(u_S - u_D) + c_{PS}\dot{u}_S + k_{PS}u_D = -m_D\ddot{x}_g \tag{3.3b}$$

4 PROPOSED NEGATIVE STIFFNESS VIBRATION ABSORPTION DEVICES

4.1 Introduction to Extended Stiff Base Absorbers

4.1.1 Schematic presentation of the proposed Extended Stiff Base Absorbers

The present thesis aims to propose extended versions of the “Stiff Base Absorber” (SBA) system, as presented in the work of (Kapasakalis, Antoniadis, & Sapountzakis, 2022). More specifically, additional inerter elements are introduced and placed in different locations of the proposed dynamic vibration absorber, to enhance its performance and maintain its previously defined advantages.

The proposed extended versions of SBA, which will be referred as **ESBA** from now on, are presented in the following figures. The first alternative configuration, **ESBA-1**, depicted in (Fig. 4.1), introduces an additional inerter element $\boldsymbol{b_{NS}}$ parallel to the negative stiffness (NS) element $\boldsymbol{k_{NS}}$ and aims to reduce the Negative Stiffness (NS) stroke (relative displacement between the terminals of the NS element).

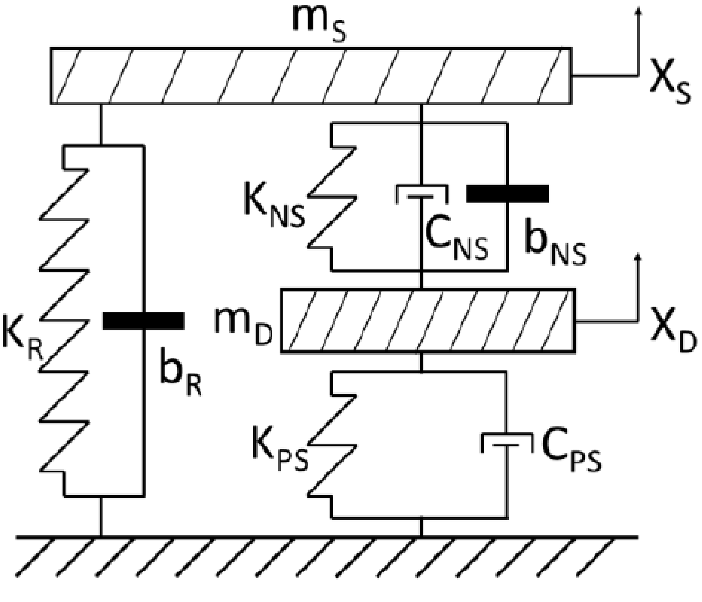

Figure 4.1: Configuration of the ESBA-1 proposed system

The second alternative, **ESBA-2** in (Fig. 4.2), introduces an inerter element $\boldsymbol{b_{PS}}$ parallel to the grounded positive stiffness element $\boldsymbol{k_{PS}}$, aiming to reduce the displacement of the additional oscillating mass.

Finally, a third alternative is proposed, **ESBA-3** in (Fig. 4.3). This is a combination of the two previously mentioned configurations, incorporating both the $\boldsymbol{b_{NS}}$ and $\boldsymbol{b_{PS}}$ inerters, between the additional oscillating mass and the rigid mass mounted on top, and the oscillating mass and the ground, respectively, with the expectation to exhibit the best possibly dynamic performance.

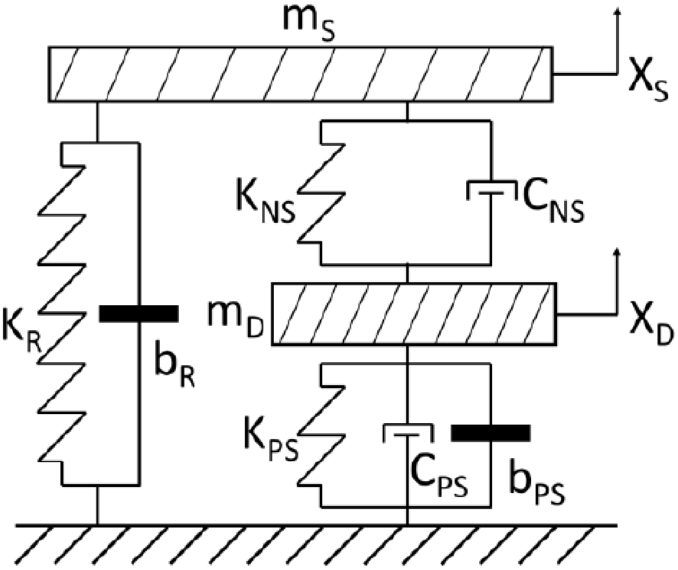

Figure 4.2: Configuration of the ESBA-2 proposed system

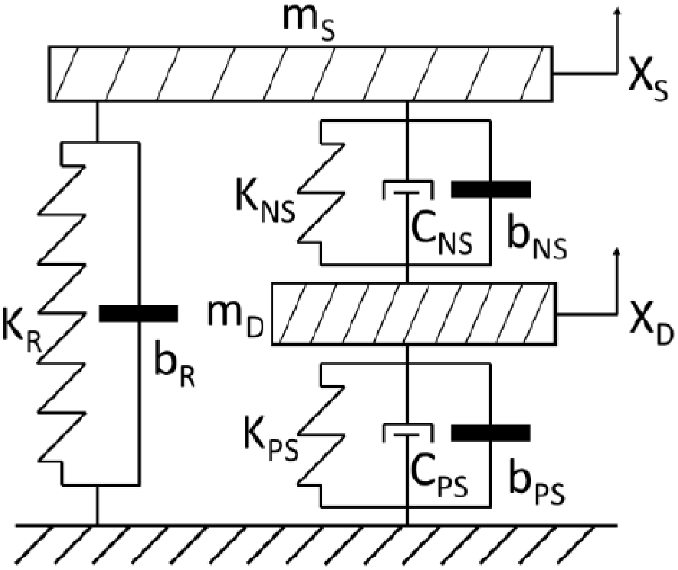

Figure 4.3: Configuration of the ESBA-3 proposed system

4.1.2 Mathematical expression of the proposed Extended Stiff Base Absorbers

Taking into account the various configurations of the ESBA system and its components, the equations of motion, that define its dynamic performance, may be formulated. Starting with the ESBA-1 configuration, compared to the original SBA system, as an extended version of the KDamper, in a similar way the following equations are expressed as for the rigid mass and the additional mass, respectively:

$$[m_S + (b_R + b_{NS})m_S]\ddot{u}_s - (b_{NS}m_S)\ddot{u}_D + c_{NS}\dot{u}_S - c_{NS}\dot{u}_D + (k_R + k_{NS})u_S \\ -k_{NS}u_D \ = -m_S\ddot{x}_g \tag{4.1}$$

$$-(b_{NS}m_S)\ddot{u}_s + [(b_{NS}m_S) + m_D]\ddot{u}_D - c_{NS}\dot{u}_S + (c_{NS} + c_{PS})\dot{u}_D - k_{NS}u_S \\ +(k_{PS} + k_{NS})u_D = -\,m_D\ddot{x}_g \tag{4.2}$$

In the above equations, m_S is the total mass of the rigid mass (including the mass of any additional superstructure elements if they exist), m_D is the mass of the additional oscillating mass, c_{NS} is the damping coefficient of the artificial damper between the rigid mass and the additional oscillating mass, c_{PS} is the damping coefficient of the damper lying between the additional oscillating mass and the ground, k_{NS} is the stiffness of the negative stiffness element, k_{PS} is the stiffness of the positive stiffness element and k_R is the stiffness of the structure. Finally, since b_R, b_{NS} (or b_{PS} as follows) express inertance, their units are in terms of mass. This is applied to various works, such as (De Domenico & Ricciardi, 2018) or (Qiao, Huang, De Domenico, & Wang, 2022). However, in the present thesis a slightly different expression of inertance is used. They are expressed as a portion/percentage of the total mass m_S. Thus, the above equations are defined in this form. Those relations are produced by considering an external base excitation of the form $x_g(t)$. The terms u_S and u_D describe the relative to the ground displacements of the structure and the oscillating mass, respectively. The superimposed dot (or two dots) denote the derivative with respect of time, with the one dot expressing the first derivative or equivalently the relative velocity and the two dots the second derivative, which corresponds to the relative acceleration.

It is convenient for the following calculations and analyses to transform the equations (4.1) and (4.2) in matrix form. They are defined as:

$$\boldsymbol{M}\ddot{\boldsymbol{u}}(t) + \boldsymbol{C}\dot{\boldsymbol{u}}(t) + \boldsymbol{K}\boldsymbol{u}(t) = -\boldsymbol{\tau}\ddot{x}_g(t) \tag{4.3}$$

Where:

$$\boldsymbol{M} = \begin{bmatrix} [m_S + (b_R + b_{NS})m_S] & -(b_{NS}m_S) \\ -(b_{NS}m_S) & [(b_{NS}m_S) + m_D] \end{bmatrix}$$

$$\boldsymbol{C} = \begin{bmatrix} c_{NS} & -c_{NS} \\ -c_{NS} & (c_{NS} + c_{PS}) \end{bmatrix}$$

$$\boldsymbol{K} = \begin{bmatrix} (k_R + k_{NS}) & -k_{NS} \\ -k_{NS} & (k_{PS} + k_{NS}) \end{bmatrix}$$

$$\boldsymbol{\tau} = \begin{bmatrix} m_S \\ m_D \end{bmatrix}$$

$$\boldsymbol{u}(t) = \begin{bmatrix} u_S(t) \\ u_D(t) \end{bmatrix} \tag{4.4}$$

In matrix and vector notation, boldface capital variables denote matrices and boldface lowercase vectors, respectively.

Continuing with the rest two ESBA configurations, the equations of motion are formed in the same exact way. In accordance with the above (Fig. 4.2), for the ESBA-2 it is:

$$(m_S + b_R m_S)\ddot{u}_s + c_{NS}\dot{u}_S - c_{NS}\dot{u}_D + (k_R + k_{NS})u_S - k_{NS}u_D = -m_S\ddot{x}_g \tag{4.5}$$

$$\begin{aligned}&[m_D + (b_{PS}m_S)]\ddot{u}_D - c_{NS}\dot{u}_S + (c_{NS} + c_{PS})\dot{u}_D - k_{NS}u_S \\ &+(k_{PS} + k_{NS})u_D = -\, m_D\ddot{x}_g\end{aligned} \tag{4.6}$$

As it can be clearly observed, only the arrangement of the terms containing the inerter quantities is altered. So, by expressing those relations in matrix form, only the mass matrix is differentiated as:

$$\boldsymbol{M} = \begin{bmatrix} (m_S + b_R m_S) & 0 \\ 0 & (m_D + b_{PS}m_S) \end{bmatrix} \tag{4.7}$$

while all the rest of the matrices remain intact.

Finally, according to the (Fig. 4.3) the relations of the motion concerning the ESBA-3 configuration sum up as:

$$\begin{aligned}&[m_S + (b_R + b_{NS})m_S]\ddot{u}_s - (b_{NS}m_S)\ddot{u}_D + c_{NS}\dot{u}_S - c_{NS}\dot{u}_D + (k_R + k_{NS})u_S \\ &-k_{NS}u_D \;\; = -m_S\ddot{x}_g\end{aligned} \tag{4.8}$$

$$\begin{aligned}&-(b_{NS}m_S)\ddot{u}_s + [m_D + (b_{NS} + b_{PS})m_S]\ddot{u}_D - c_{NS}\dot{u}_S + (c_{NS} + c_{PS})\dot{u}_D - k_{NS}u_S \\ &+(k_{PS} + k_{NS})u_D = -\, m_D\ddot{x}_g\end{aligned} \tag{4.9}$$

Since, ESBA-3 is a combination of the other two configurations, the fact that relation (4.8) coincides with the (4.1) emerges. Similarly, the only different matrix is the mass matrix again and is configured as:

$$\boldsymbol{M} = \begin{bmatrix} [m_S + (b_R + b_{NS})m_S] & -(b_{NS}m_S) \\ -(b_{NS}m_S) & [m_D + (b_{NS} + b_{PS})m_S] \end{bmatrix} \tag{4.10}$$

Once the equations of motion of the proposed vibration absorbers (ESBA) are stated, the goal now is to determine the optimal system parameters.

4.2 Statement of the optimization problem

As observed in the previously defined equations, there is a multitude of variables that render the dynamic performance of the ESBA system feasible. In order to define the best values of these parameters so as to enhance the performance of the ESBA system, an optimization procedure may be followed. A first approach can be made by adopting the classical minmax (H∞) procedure, as described by (Den Hartog, 1956). This procedure aims at the minimization of a suitably selected transfer function of the system. However, since there is the option to select a specific transfer function to be minimized, different results can be produced. As aptly mentioned in the work of (Kapasakalis, Alamir, Antoniadis, & Sapountzakis, 2021), the minimization of a transfer function referring to the relative displacement (H_{US}), for example, may give non optimal results, while the minimization of that of the absolute acceleration (H_{AS}) may yield the optimal values of the parameters and thus, confirming that the results can have significant discrepancies, depending on the option of various transfer functions.

Due to the aforementioned problem, considering non optimal, but mathematically acceptable results, the values of the variables that characterize the ESBA system may lead to non-realistic results. That means, large values of the stiffness elements, the dampers or the inerters can have an adverse impact on the technological design of the system, as it may not be feasible to design, construct and implement those components to meet those requirements. From the other hand, it might be financially difficult to apply these configurations and as a result be a disadvantageous system compared to the conventional base isolation.

In order to avoid those situations, an optimization procedure that can end up in realistic configurations adjacent to reasonably engineered criteria is sought. The dynamic vibration absorber should be designed to meet all the geometrical and constructional limitations imposed by the structural system and retain the values of all the components to reasonable ranges.

4.2.1 Optimization process – Harmony Search Algorithm

Structural design optimization is a vital and complex task that has gained significant attention in recent years. Various mathematical methods, including linear, nonlinear, and dynamic programming, have been developed to tackle engineering optimization problems. However, these methods have limitations and none of them are entirely effective and robust for all types of optimization problems, according to (Lee & Geem, 2004). Some mathematical methods exhibit drawbacks in optimization processes, as they require calculations with complex derivatives, have sensitivity depending on the initial values or demand large amount of enumeration memory. Those techniques, usually, search a solution in the nearby area of the initial point. If the solution encounters a local optimum of the many, the engineering problem may have, the result will not be a global optimum and solution direction will depend on the initial point. Moreover, due to many constraints the problem may have, gradient search may become difficult and unstable. Those reasons justify the fact that these methods may be inefficient for optimization problems, especially for large structural problems with a great number of variables, and perform a large amount of gradient calculations with many iterative processes without a possible achievement of the global optimum.

Scientists have moved in the direction of the approximate algorithms to overcome the aforementioned limitations (Alia & Mandava, 2011). Metaheuristic algorithms are well known approximate algorithms, which can deal with optimization problems with satisfying results. The special characteristic of metaheuristic algorithms is that they combine rules and random aspects to imitate natural phenomena. A novel metaheuristic algorithm, that of the Harmony Search (HS) (Geem, Kim, & Loganathan, 2001), is one the most efficient algorithms in the field of combinatorial optimization. It is a population-based algorithm that imitates the musical improvisation process where musicians search for the ideal state of harmony by improvising the pitch of their instruments.

In (Alia & Mandava, 2011) there is an analytical explanation of the steps that HS algorithm involves. They are described as follows:

At first the optimization process that has to be made is to minimize or maximize a function $f(\boldsymbol{x})$ which is subject to $x_i \in X_i$, for i=1,2,…,N. $f(\boldsymbol{x})$ is the objective function, $\boldsymbol{x}$ is a set (vector solution) of each decision variable x_i, X_i is the possible range of each variable and N is the number of variables. There are some parameters that operate the HS algorithm and are explained analytically in the steps that come after.

- STEP 1 – Initialize Harmony Memory (HM)

In the first step, the aim is to construct the Harmony Memory (HM) matrix. This matrix has dimensions of (HMS)x(N). HMS stands for Harmony Memory Size and is the first parameter of the procedure. It is the number of randomly generated solution vectors. The HM matrix has the following form:

$$\boldsymbol{HM} = \begin{bmatrix} x_1^1 & x_2^1 & \dots & x_N^1 \\ x_1^2 & x_2^2 & \dots & x_N^2 \\ \vdots & \vdots & \dots & \vdots \\ x_1^{HMS} & x_2^{HMS} & \dots & x_N^{HMS} \end{bmatrix} \tag{4.11}$$

Each row represents a possible solution vector which has been randomly generated for every variable (N in total -number of columns- for an N dimensional problem). Every variable x_l^k, where $k \in [1, HMS], l \in [1, N]$ has been randomly generated from its predefined range as follows:

$$x_l^k = rand() \cdot ({}_U x_l^k - {}_L x_l^k) + {}_L x_l^k \tag{4.12}$$

Where ${}_L x_l^k$ and ${}_U x_l^k$ are the lower and upper limit of the range of each variable, respectively and $rand()$ is a random scalar drawn from the uniform distribution in the interval (0,1).

Finally, in parallel with the initial HM matrix, a vector **fit** with dimensions (1)x(HMS) is constructed, that contains the objective function values generated by every set of variables.

- STEP 2 – Improvise a new harmony

In this step a new harmony vector $x' = (x'_1, x'_2, \dots, x'_N)$ is generated by checking the probability test of HMCR. HMCR is the second parameter of the HS algorithm, it stands for Harmony Memory Considering Rate and since it is probability it is by definition HMCR ∈ [0,1]. For every new variable of the new harmony vector, if a random scalar, again drawn from the uniform distribution in the interval (0,1), is smaller than HMCR, then the new value is retrieved from a random position of the column of the already configured HM matrix that refers to that specific variable. If not (if the random scalar is larger than HMCR), then the new variable x'_i will be newly generated again from the previous relation (4.12). This operation is correlated with the musician's ability to produce a tune from his memory or create a new one.

However, a further mutation of the new variable may be performed if it belongs to the first case of the randomly inherited historical values of the HM matrix. This will be achieved by checking the PAR probability. PAR stands for Pitch Adjusting Rate and again it is PAR ∈ [0,1]. If a randomly generated scalar lies within the PAR probability, then the decision variable will be adjusted according to the following relation:

$$x'_i = x'_i \pm rand() \cdot b_W \tag{4.13}$$

Where b_W is an arbitrarily chosen distance bandwidth that determines how much the new value will change compared to the older one. Its value depends on the nature of the examined engineering problem and can be different for any variable. However, for simplicity reasons a uniform value may be taken for all the variables and the algorithm should be altered to take into account that the new decision variables will not exceed the limits of their ranges. Moreover, the ± case can follow a 50%-50% probability scheme. At the other hand if the rand lies outside the PAR probability, then the decision variable remains intact. This operation resembles to the musician's ability to play something similar to a known piece and thus he/she adjusts the pitch slightly. All the above can be summarized into the following relations:

$$x'_i = \begin{cases} x'_i \in \{x_i^1, x_i^2, \dots, x_i^{HMS}\}, with\ probability\ HMCR \\ x'_i \in rangeX_i, with\ probability\ (1 - HMCR) \end{cases} \tag{4.14}$$

$$x'_{i,within\ HMCR} = \begin{cases} Eq\ (4.13), with\ probability\ PAR \\ Do\ nothing, with\ probability\ (1 - PAR) \end{cases} \tag{4.15}$$

- STEP 3 – Update the Harmony Memory

Since the new harmony vector has been configured, the new value of the objective function is calculated and is compared to the worst value of the objective function from the set of decision variables stored in the HM matrix. If the new vector yields a better result than the worst, then the worst vector is replaced by the new one. If this does not happen, then the new vector will be rejected and the HM matrix will remain intact.

- STEP 4 – Stopping criterion

The steps 3 and 4 are repeated until a stopping criterion is satisfied. A common terminating criterion is the maximum number of total iterations. Then the best harmony vector is selected and considered the best solution that gives optimal results.

The (Table 4.1), below, contains the values of the parameters of the HS algorithm that were adopted for the following analyses.

Table 4.1: Parameters of the HS algorithm

HMS	**HMCR**	**PAR**	**b_w**
75	0.5	0.1	0.5

4.2.2 Evaluation of optimization constraints and limitations

Once the optimization algorithm and strategy have been figured out, the next step is to determine the imposed constraints and limitations that have to be set to the variables of the problem. Those constraints are necessary as they will result to a technologically feasible design of the ESBA configurations and its components will lie within realizable limits that will meet engineering and constructional criteria.

The first limitation is to define the variables that have to be optimized. Since the ESBA configurations are an advanced extended version of the KDamper concept, they satisfy the first basic requirement of it (Antoniadis, Kanarachos, Gryllias, & Sapountzakis, 2018), which is that the overall static stiffness of the system is maintained, overcoming the main disadvantage of the NS isolator and is expressed by the relation that follows:

$$k_R + \frac{k_{NS} k_{PS}}{k_{NS} + k_{PS}} = k_0 = (2\pi f_0)^2 m_{total} \tag{4.16}$$

Where k_0 and f_0 are the overall static stiffness and frequency of the system, respectively and m_{total} is the total mass of the system, including both the total mass of the superstructure and the mass of the oscillating mass of the KDamper.

Moreover, since ESBA configurations are enriched versions of the Extended KDamper concept, with inerters in various locations, they subsequently adopt the characteristics concerning the variations in the values of the stiffness elements of the system (Kapasakalis, Antoniadis, & Sapountzakis, Constrained optimal design of seismic base absorbers based on an extended KDamper concept, 2021). In other words, due to various reasons, like temperature variations, manufacture tolerances or nonlinear behaviors, all the stiffness elements may exhibit a significant behavior in practice, as all the negative stiffness configurations emerge from unstable nonlinear systems. So, the ESBA design, just like the Extended KDamper, foresees a simultaneous variation in the values of all the stiffness elements, in order to secure the static stability of the system. This is achieved by introducing stiffness variation coefficients in the limit case where the system becomes statically unstable. This is realized when the stiffness matrix determinant becomes zero. Thus, by considering synchronous variations and more specifically, an increase in the absolute value of the negative stiffness by a factor ε_{NS} and a decrease in the values of the positive stiffnesses k_R and k_{PS} by factors ε_R and ε_{PS}, respectively, the following equation is yielded:

$$\det(\boldsymbol{K}) = 0 \quad => \quad (1-\varepsilon_R)k_R + \frac{(1+\varepsilon_{NS})k_{NS}(1-\varepsilon_{PS})k_{PS}}{(1+\varepsilon_{NS})k_{NS}+(1-\varepsilon_{PS})k_{PS}} = 0 \tag{4.17}$$

By introducing an auxiliary coefficient of the negative stiffness ratio, which is defined as:

$$k_{ns} = \frac{k_{NS}}{k_0} \tag{4.18a}$$

The values of all the rest stiffness elements can be determined with the use of stiffness ratios by combining the (Eq. 4.16) and (Eq. 4.17) as follows:

$$k_r = \frac{-b-\sqrt{b^2-4a\cdot c}}{2a} \quad => \quad k_R = k_r \cdot k_0 \tag{4.18b}$$

$$k_{ps} = \frac{k_{ns}-k_r\cdot k_{ns}}{k_r+k_{ns}-1} \quad => \quad k_{PS} = k_{ps} \cdot k_0 \tag{4.18c}$$

Where parameters a, b and c are defined as:

$$a = R(PS-NS) \tag{4.19a}$$

$$b = k_{ns} \cdot NS(PS-R) + R(NS-PS) \tag{4.19b}$$

$$c = -PS \cdot NS \cdot k_{ns} \tag{4.19c}$$

Where the auxiliary parameters R, NS and PS are the following:

$$R = (1-\varepsilon_R) \tag{4.20a}$$

$$NS = (1+\varepsilon_{NS}) \tag{4.20b}$$

$$PS = (1-\varepsilon_{PS}) \tag{4.20c}$$

From the above, it is now obvious that the optimization process can be implemented by adopting the following conditions:

- The optimization problem is formed to comply with seismic design codes. The constraints and objective function are selected from time-domain responses. The procedure, from which the system is set dynamically motioned, involves earthquake ground excitations, which their selection is described in the next section (4.2.3).
- The objective function is set to be the relative to the ground structure displacement.
- Based on previous work (Kapasakalis, Antoniadis, & Sapountzakis, 2019), the negative stiffness stroke may be set as a constraint with an upper limit of 15cm.

However, in this work it is let as a free parameter, in order to check its tendency of variation and observe at what magnitudes it can reach. A slightly higher hypothetical limit of 20cm could be chosen so as to not exceed the constructional criteria of manufacturing tolerances.

- The ESBA configurations are designed to be an efficient and a realistic vibration absorption system. So, to better observe the efficiency of the proposed configurations, an acceleration filter is placed. Therefore, each set of the optimized parameters of the ESBA refers to the maximum structure acceleration, expressed as a percentage of the PGA (Peak Ground Acceleration) of the accelerogram of the ground excitation.
- Based, again on previous work (Kapasakalis, Antoniadis, & Sapountzakis, 2019) the negative stiffness coefficient factor ε_{NS} was taken equal to 5%. In this work, all the stability stiffness factors ε_{NS}, ε_{R} and ε_{PS} are considered equal to 10%. This increase takes into consideration larger variations in the magnitude of all the stiffnesses and can be judged as a conservative safety feature.
- Considering the magnitude of the oscillating mass, since the ESBA system can be placed at the base of the structure, there is no a particular limitation to its mass. In fact, in the work of (Kapasakalis, Antoniadis, & Sapountzakis, Performance assessment of the KDamper as a seismic Absorption Base, 2019) was taken as the 5% of the total mass of the superstructure and it proved to be efficient. In the other work of (Kapasakalis, Antoniadis, & Sapountzakis, 2022) it was considered as the 0.1% reducing significantly its magnitude. In the present work it is taken as an intermediate value between the two aforementioned, that of 1%, which is again a quite small portion compared to that of the total mass.
- Considering the negative stiffness, according to (Antoniadis, Kanarachos, Gryllias, & Sapountzakis, 2018), where the negative stiffness element is realized with pre-compressed springs (a more analytical description exists in Chapter 5), an approximate value of -100 kN/m per 1000kg mass of the superstructure is realistic. In this work, a 50% reduced value, that of -50 kN/m per 1000kg of the superstructure mass is considered, for a more efficient design of the system. In other words, for a 300 tonnage total mass of the base and the superstructure, an upper limit of -15000 kN/m is considered. The value of 300 Mgr is an indicative value of a 3storey concrete building with a base.
- The damping coefficients' maximum value is set at 3 kNs/m per 1 Mgr of structure mass. That means, again for a 300 Mgr total mass of the structure a value of 900 kNs/m is set as the upper limit. So, common linear damping devices can be used.
- In the work of (Kapasakalis, Antoniadis, & Sapountzakis, 2022), two cases of the maximum values of the inerter are examined, that of 100% and 200% of the total mass of the structure. In this work, since there are more inerter configurations in various locations and combinations, two cases of 20% and 50% of the total mass of the structure are investigated.
- Finally, for the nominal frequency of the ESBA system an upper limit of 1.5 Hz is considered.

The following (Table 4.2) concentrates the limits of the free design variables that are considered for the optimization processes of the ESBA system.

Table 4.2: Limits of the free design variables

f_0 (Hz)	k_{NS} (kN/m)	c_{NS} (kNs/m)	c_{PS} (kNs/m)	b_R (% ms)	b_{NS} (% ms)	b_{PS} (% ms)
[0.2 1.5]	[-15000 -3000]	[100 900]	[0 900]	[0 20] or [0 50]	[0 20] or [0 50]	[0 20] or [0 50]

By considering all the above data and by setting values to the nominal frequency of the system and the negative stiffness element, the rest of the stiffnesses of the system are automatically emerge by combining all the relations (4.16)-(4.20c).

4.2.3 Generation of spectrum compatible artificial accelerograms

As it was mentioned in the previous section (4.2.2), the optimization problem is set to comply with the seismic codes. The structure's responses of absolute acceleration and relative displacement are controlled by the following characteristics: the structure's fundamental period, damping ratio, the ground conditions and the seismic intensity. Since the ESBA configurations are an extended version of the KDamper, their application as an absorption base creates Multi-Degree of Freedom systems (MDoF) and therefore this renders the direct application of the design response spectra impossible. A solution to this, is the analysis at the time-domain level. Thus, artificial accelerograms that are compatible with a design response spectrum are suitable for the optimal design of the proposed dynamic vibration absorbers.

In this study, 30 artificial accelerograms, that are compatible with the Eurocode 8 (EC 8) Type 1 elastic horizontal acceleration design response spectrum, are used. They correspond to the quite unfavorable case of the seismic danger zone III, which gives a ground acceleration of 0.36g. Moreover, the importance class II is used, that refers to a typical residential building. The case of ground type C is used. The mean PGA of the artificial accelerograms is 5.19 m/sec^2. More information of the spectral properties can be found in EC8 (EN 1998-1, 2004). The database of the artificial accelerograms is taken from the work of (Kapasakalis A. K., 2020). In the same work, there is an analytical description on how the artificial accelerograms were generated.

In the figure below (Fig. 4.4(a)), there is the time history of an indicative artificial accelerogram. Its peak acceleration is quite near the mean PGA. The duration of the earthquake is 30 seconds. In the same figure (Fig. 4.4(b)), there is the plot of the acceleration response spectrum generated by the random accelerogram and the mean acceleration response spectrum generated by the 30 artificial accelerograms. They are both compared to the EC8 horizontal acceleration response spectrum. All of them are plotted by considering a typical viscous damping of 5%. As it can be clearly observed, all the artificial accelerograms yield a well fitted response spectrum compared to the EC8 equivalent design. In fact there is an adequate-near perfect- match of the mean artificial response spectrum in the range of periods 0.2 sec to 2 sec, which are representative values for the structure performance. The response spectrum, generated by the individual random accelerogram, exhibits a similar behavior with some minor fluctuations in the same periods.

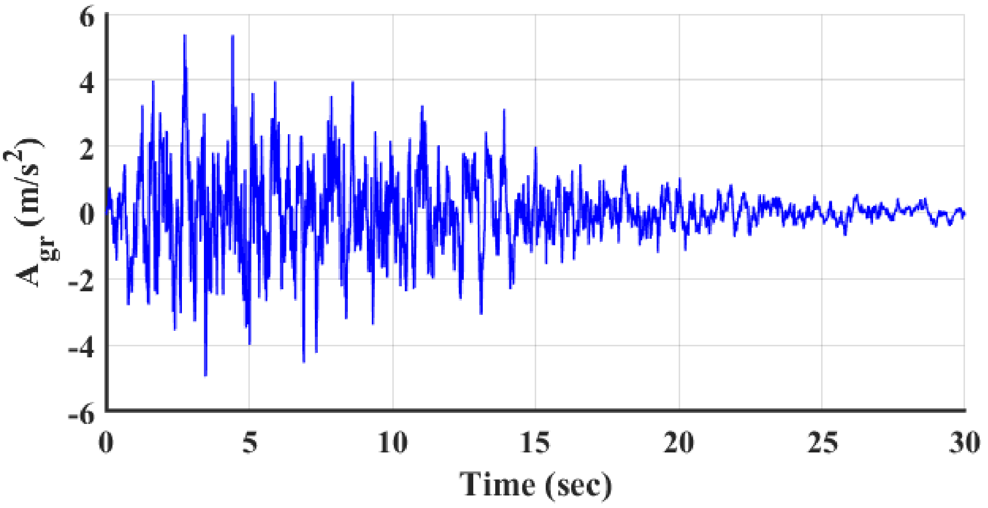

(a)

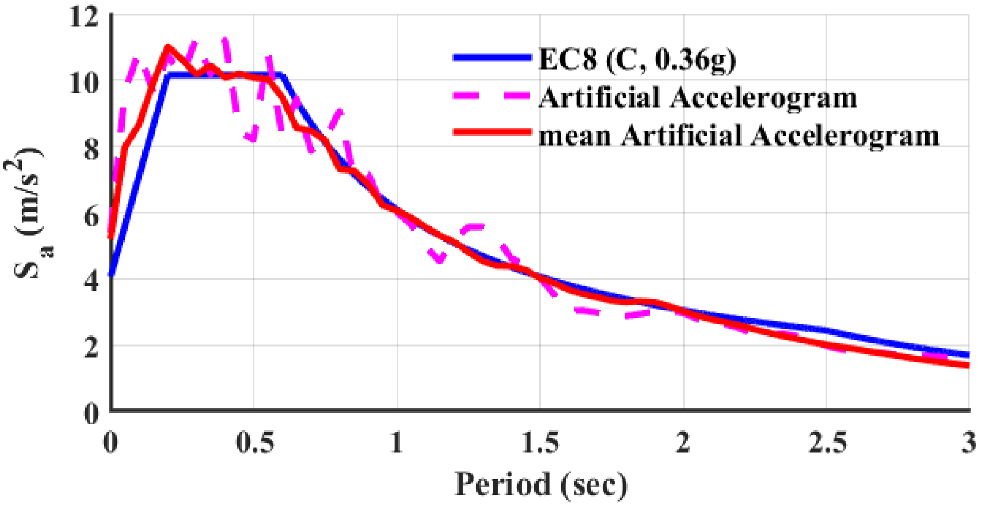

(b)

Figure 4.4: (a) Random artificial accelerogram and (b) individual and mean artificial acceleration response spectrum, of the 30 generated artificial accelerograms in the database compared to the EC8 horizontal acceleration response spectrum.

4.2.4 Newmark's Method for solving the equations of motion

In section (4.2.2), it was mentioned that the constraints and objective function are selected from time-domain responses. Thus, this becomes feasible by using numerical time-stepping methods for integration of the differential equation of motion. In this way the dynamic responses of the structure, such as the relative to the ground displacement and velocity or the absolute acceleration can be defined for an external force that varies arbitrarily with the time, like the ground excitation. One of the most commonly used methods, is that of Newmark's method (Newmark, 1959). Newmark developed a family of time-stepping iterative methods based on the following equations:

$$\dot{u}_{i+1} = \dot{u}_i + [(1-\gamma)\Delta t]\ddot{u}_i + (\gamma\Delta t)\ddot{u}_{i+1} \tag{4.21a}$$

$$u_{i+1} = u_i + (\Delta t)\dot{u}_i + [(0.5-\beta)(\Delta t)^2]\ddot{u}_i + [\beta(\Delta t)^2]\ddot{u}_{i+1} \tag{4.21b}$$

From the above, u is the relative to the ground displacement of the structure, while the one or two superimposed dots express the first and second derivative with respect to time, that correspond to the relative to the ground velocity and acceleration, respectively. The indices i and $i+1$ denote an arbitrary previous time step and the exact next one, respectively. The parameters β and γ are introduced to control the variation of the acceleration over a time step and to determine the stability and accuracy of the method. As depicted in the figure below (Fig. 4.5), two cases of the variation of the acceleration over the time step have been developed. The first one is the constant average, while the other is the linear variation.

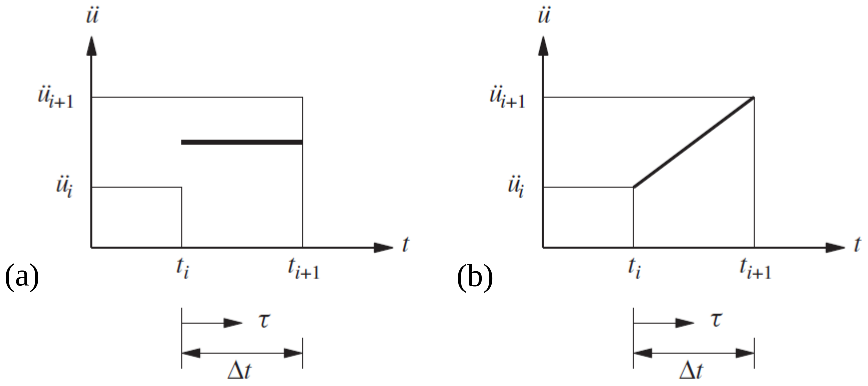

Figure 4.5: (a) Constant average acceleration and (b) Linear variation of acceleration over a time step

The relations that correspond to the variation of the acceleration over a time step (Fig. 4.5) are the following:

$$\ddot{u}(\tau) = \frac{1}{2}(\ddot{u}_{i+1} + \ddot{u}_i) \tag{4.22a}$$

$$\ddot{u}(\tau) = \ddot{u}_i + \frac{\tau}{\Delta t}(\ddot{u}_{i+1} - \ddot{u}_i) \tag{4.22b}$$

From the above, τ is an arbitrary instant over the time step Δt. Eq. (4.22a) corresponds to the constant average acceleration method, while (4.22b) is for the linear method.

The constant average acceleration method is adopted in this work, so a further elaboration of only the Eq. (4.22a) is performed. Two consecutive integrations over the time step where $\tau = \Delta t$ gives the velocity and displacement:

$$\dot{u}(\tau) = \dot{u}_i + \frac{\tau}{2}(\ddot{u}_{i+1} + \ddot{u}_i) \quad => \quad \dot{u}_{i+1} = \dot{u}_i + \frac{\Delta t}{2}(\ddot{u}_{i+1} + \ddot{u}_i) \tag{4.23a}$$

$$u(\tau) = u_i + \dot{u}_i\tau + \frac{\tau^2}{4}(\ddot{u}_{i+1} + \ddot{u}_i) \quad =>$$

$$u_{i+1} = u_i + \dot{u}_i\Delta t + \frac{(\Delta t)^2}{4}(\ddot{u}_{i+1} + \ddot{u}_i) \tag{4.23b}$$

If, at first, a Single Degree of Freedom (SDoF) is considered, the equation of equilibrium at any arbitrary time step is the following by analogy with Eq. (4.3):

$$m\ddot{u}_{i+1} + c\dot{u}_{i+1} + ku_{i+1} = p_{i+1} \tag{4.24}$$

Where, p_{i+1} is the external force. Moreover, in the Eq. (4.21b) the quantity $\ddot{u}_{i+1}$ can be expressed in terms of the quantity u_{i+1} as:

$$\ddot{u}_{i+1} = \frac{1}{\beta(\Delta t)^2}(u_{i+1} - u_i) - \frac{1}{\beta\Delta t}\dot{u}_i - \left(\frac{1}{2\beta} - 1\right)\ddot{u}_i \tag{4.25a}$$

Substituting the Eq. (4.25a) into Eq. (4.21a) it is:

$$\dot{u}_{i+1} = \frac{\gamma}{\beta\Delta t}(u_{i+1} - u_i) + \left(1 - \frac{\gamma}{\beta}\right)\dot{u}_i + \Delta t\left(1 - \frac{\gamma}{2\beta}\right)\ddot{u}_i \tag{4.25b}$$

By substituting the Eq. (4.25a) and (4.25b) into the governing Eq. (4.24) the following relation emerges:

$$\hat{k}u_{i+1} = \hat{p}_{i+1} \tag{4.26}$$

Where:

$$\hat{k} = k + \frac{\gamma}{\beta\Delta t}c + \frac{1}{\beta(\Delta t)^2}m \tag{4.27}$$

And:

$$\hat{p}_{i+1} = p_{i+1} + \left[\frac{1}{\beta(\Delta t)^2}m + \frac{\gamma}{\beta\Delta t}c\right]u_i + \left[\frac{1}{\beta\Delta t}m + \left(\frac{\gamma}{\beta} - 1\right)c\right]\dot{u}_i +$$

$$\left[\left(\frac{1}{2\beta} - 1\right)m + \Delta t(\frac{\gamma}{2\beta} - 1)c\right]\ddot{u}_i \tag{4.28}$$

The quantity $\hat{k}$ is fully known a priori, as it is defined by the structure's properties, the Newmark's method parameters and the time step. The same applies to the term $\hat{p}_{i+1}$ as it is incorporates the external force and the structures dynamic responses of relative displacement, velocity and acceleration, which are known from the last step. In the next step, the updated displacement is defined by the relation (4.26) and the method continues with the velocity and acceleration from relations (4.25b) and (4.25a), respectively and again the same procedure is performed in an iterative scheme.

Finally, the Newmark's method is stable if the following condition is satisfied:

$$\frac{\Delta t}{T_N} \leq \frac{1}{\pi\sqrt{2}}\frac{1}{\sqrt{\gamma - 2\beta}} \tag{4.29}$$

Where, T_N is the natural period of the structure.

The typical values for the parameters γ and β are 0.5 and $[\frac{1}{6}\ \frac{1}{4}]$. For this work, the constant average acceleration is used and in the table below (4.3) there are the values of the parameters that are adopted to perform the optimization procedures.

Table 4.3: Parameters of the constant average acceleration method

$\boldsymbol{\gamma}$	$\boldsymbol{\beta}$	$\boldsymbol{\Delta t}\ (\boldsymbol{sec})$
0.5	0.25	0.01

The time step coincides with values generated of the artificial accelerograms. For the values of the constant average acceleration method, relation (4.29) gives $\frac{\Delta t}{T_N} \leq \infty$. That means, the constant average acceleration method is unconditionally stable. So in this case the time step affects the accuracy of the method. The value of 0.01 sec can be considered small and thus, does not affect the accuracy.

Based on all the aforementioned, the constant average acceleration method can be extended in MDoF systems. The scalar quantities are substituted by matrices and vectorial ones. In the book of (Chopra, 2011), a pseudo-code algorithm is incorporated:

Algorithm: Constant average acceleration method

```
Determine parameters $\gamma$ and $\beta$ (=0.5 and 0.25, respectively for constant average acceleration method)
Step 1: Initial calculations
    1.1 Initial conditions $\boldsymbol{u}(0), \dot{\boldsymbol{u}}(0)$
    1.2 Initial load $\boldsymbol{p}(0) = -\boldsymbol{\tau}\ddot{\boldsymbol{x}}_g(0)$
    1.3 Initial acceleration: $\ddot{\boldsymbol{u}}(0) = [\boldsymbol{M}]^{-1}(\boldsymbol{p}(0) - \boldsymbol{C}\dot{\boldsymbol{u}}(0) - \boldsymbol{K}\boldsymbol{u}(0))$
    1.4 Select $\Delta t$
    1.5 Compute: $\mathbf{a}_1 = \frac{1}{\beta(\Delta t)^2}\boldsymbol{M} + \frac{\gamma}{\beta\Delta t}\boldsymbol{C};\ \mathbf{a}_2 = \frac{1}{\beta\Delta t}\boldsymbol{M} + \left(\frac{\gamma}{\beta} - 1\right)\boldsymbol{C};$
            $\mathbf{a}_3 = \left(\frac{1}{2\beta} - 1\right)\boldsymbol{M} + \Delta t(\frac{\gamma}{2\beta} - 1)\boldsymbol{C}$
    1.6 Compute: $\widehat{\boldsymbol{K}} = \boldsymbol{K} + \mathbf{a}_1$
Step 2: Calculations for each time step, $i = 0, 1, 2, \dots$
    2.1 $\widehat{\boldsymbol{P}}_{i+1} = -\boldsymbol{\tau}\ddot{\boldsymbol{x}}_{g,i+1} + \mathbf{a}_1\boldsymbol{u}_i + \mathbf{a}_2\dot{\boldsymbol{u}}_i + \mathbf{a}_3\ddot{\boldsymbol{u}}_i$
    2.2 Solve: $\widehat{\boldsymbol{K}}\boldsymbol{u}_{i+1} = \widehat{\boldsymbol{P}}_{i+1}$  =>  $\boldsymbol{u}_{i+1} = [\widehat{\boldsymbol{K}}]^{-1}\widehat{\boldsymbol{P}}_{i+1}$
    2.3 $\dot{\boldsymbol{u}}_{i+1} = \frac{\gamma}{\beta\Delta t}(\boldsymbol{u}_{i+1} - \boldsymbol{u}_i) + \left(1 - \frac{\gamma}{\beta}\right)\dot{\boldsymbol{u}}_i + \Delta t\left(1 - \frac{\gamma}{2\beta}\right)\ddot{\boldsymbol{u}}_i$
```

2.4 $\ddot{\boldsymbol{u}}_{i+1} = \frac{1}{\beta(\Delta t)^2}(\boldsymbol{u}_{i+1} - \boldsymbol{u}_i) - \frac{1}{\beta\Delta t}\dot{\boldsymbol{u}}_i - \left(\frac{1}{2\beta} - 1\right)\ddot{\boldsymbol{u}}_i$

Step 3: Repetition for the next time step. Replace i by $i + 1$ and implement steps 2.1 to 2.4 for the next time step

---

The external loading is modified to comply with the Eq. (4.4).

4.3 Optimization curves

By implementing all the aforementioned, the optimization curves are yielded. The analyses are performed by considering two cases of the maximum value of the inerters for all the ESBA configurations, that of $b_{max} = 0.2$ and $b_{max} = 0.5$, as they are expressed as a percentage of the total mass of the structure m_S. According to section (4.2.2) an acceleration filter is placed to observe the efficiency of the proposed vibration absorption system. The optimization procedure is performed in a way, so that every set of the optimized parameters can refer to a specific value of the structure's absolute acceleration. The range of the acceleration filter is from 25% to 75% with a step of 2.5% for every analysis. The absolute acceleration may be expressed as a percentage of the mean PGA of all the artificial accelerograms.

According to the STEP 4 of the harmony search algorithm, a stopping criterion, like the total number of iterations, should be imposed. A total number of 100000 iterations per acceleration filter step is considered to yield quite accurate results. However, since there are many iterations and many parameters to be optimized, the whole procedure can be quite time-consuming. Thus, in an attempt to reduce the time consumption of the procedures, the following conditions were adopted, in order to get the first results:

- Instead of optimizing the parameters of all the ESBA configurations with respect to the mean PGA of all the artificial accelerograms, the parameters are optimized by considering one random accelerogram out of the total thirty. After all, the PGA of this random accelerogram is 5.21m/sec^2 (almost equal to the 5.19m/sec^2 of the mean PGA) and each one of the accelerograms exhibit similar behavior compared to one another. In this way the total time of the whole optimization can be reduced to 1/30.
- Based on (Kapasakalis, Antoniadis, & Sapountzakis, Constrained optimal design of seismic base absorbers based on an extended KDamper concept, 2021) the variation of c_{PS} parameter by ±50% had an insignificant effect on the results. So, as a first approach, since all ESBA configurations are extended versions of the extended KDamper, the c_{PS} parameter is considered to have a fixed value, that of 100 kNs/m.

Based on these, the first optimization curves are presented in the following figure (Fig. 4.6(a) and 4.6(b)). The first figure (Fig. 4.6(a)) depicts the structure's maximum relative to the ground displacement over the structure's maximum absolute acceleration, expressed as a percentage of the PGA of the random accelerogram. As it can be observed, all the configurations exhibit a similar graphic behavior. As the acceleration

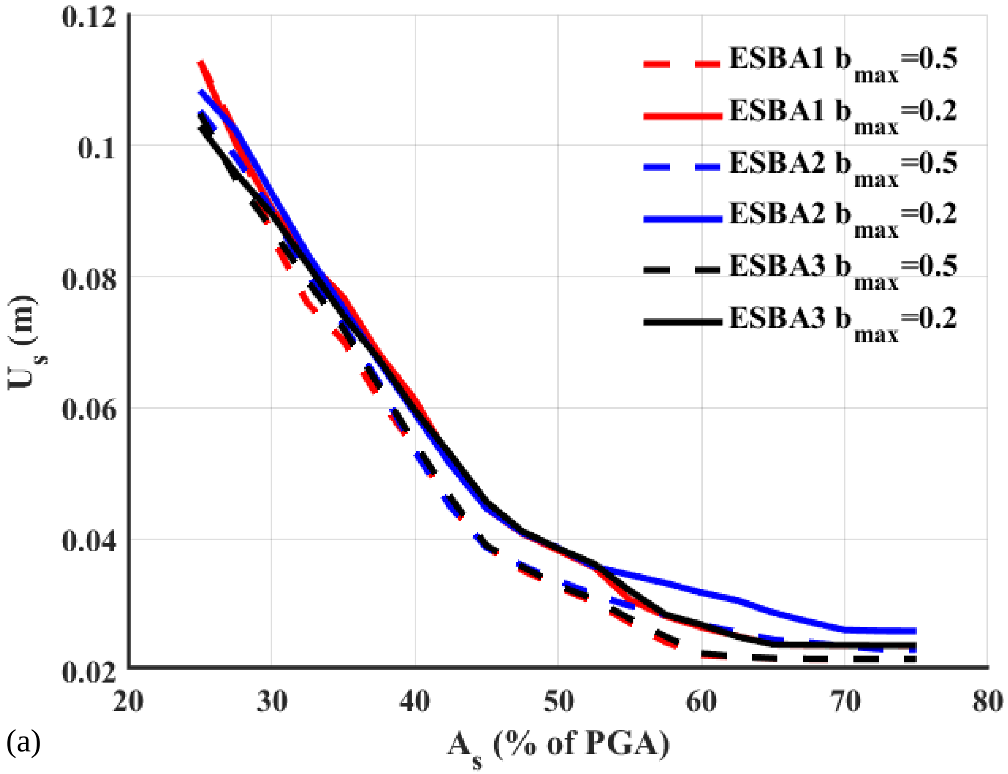

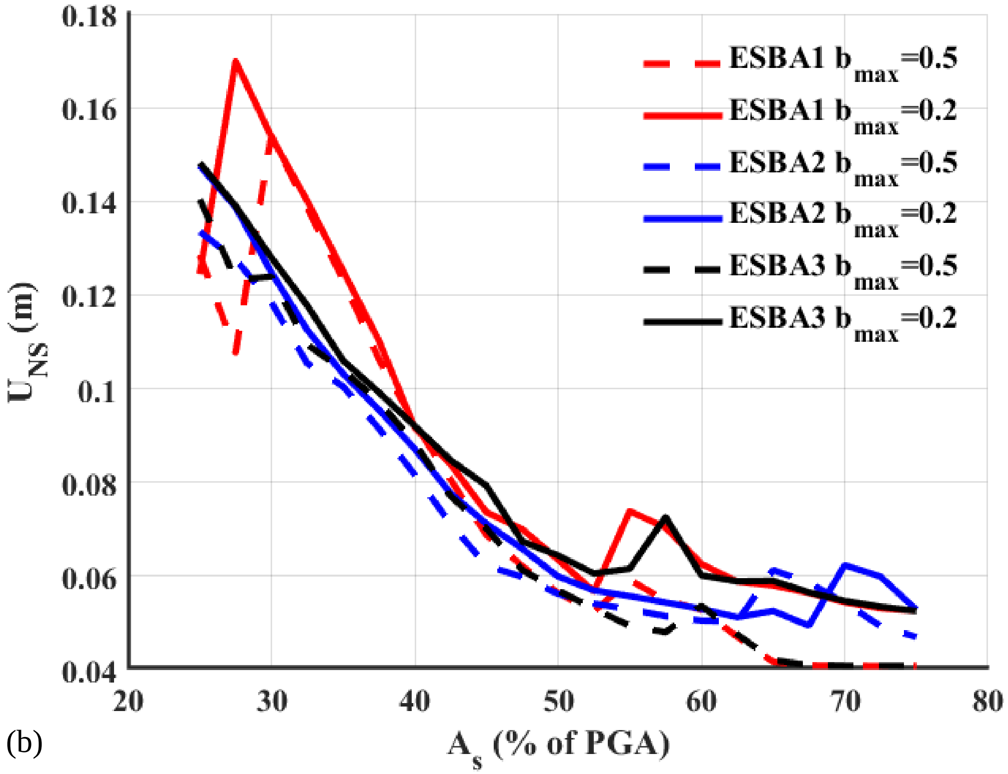

Figure 4.6: (a) Structure relative displacement and (b) NS element stroke maximum values over the structure absolute acceleration (% of PGA), of the ESBA configurations optimized with respect to a random artificial accelerogram, for *bmax*=0.2 and *bmax*=0.5 and c_{PS}=100 kNs/m

filter increases, the structural drifts decrease. Moreover, as expected, by increasing the upper limit of the inerter elements, the structural drifts are further reduced in all ESBA configurations. At the lowest filters, the relative displacement fluctuates between 0.113m and 0.103m, with the highest value corresponding to the ESBA-1 (both inerter cases) and the lowest value to the ESBA-3 (again for both inerter cases). At intermediate filters, it is clear that all configurations coincide together in each case, with the higher inerter maximum value having smaller displacements. For example, for the 45% acceleration filter, the relative displacement is approximately 0.045m for all ESBA configurations at $b_{max} = 0.2$ and 0.039m for all ESBA configurations at $b_{max} = 0.5$. Finally, at the highest filters ESBA-2 for $b_{max} = 0.2$ is the worst case, ESBA-2 for $b_{max} = 0.5$ coincides with ESBA-1 and ESBA-3 for $b_{max} = 0.2$ and ESBA-1 and ESBA-3 for $b_{max} = 0.5$ coincide and having simultaneously the best behavior, as the relative displacement appears to be 0.022m. The second figure (Fig. 4.6(b)) depicts the NS stroke over the structure's maximum absolute acceleration, expressed again as a percentage of the PGA of the random accelerogram. In general, the same apply to these curves. As the filter increases, the NS stroke decreases and the maximum upper limit inerters have reduced values in relation with the minimum upper limit. However, those curves, compared to the ones of the relative displacement, do not have the smoothly decreasing graphical scheme, especially in the ESBA-1 configuration. At lowest filters, they exhibit a sudden increase, reaching the values of 0.17m (for $b_{max} = 0.2$) and 0.154m (for $b_{max} = 0.5$). The other two configurations produce an NS stroke slightly above from 0.14m (for $b_{max} = 0.2$) and below from that value (for $b_{max} = 0.5$). At the next lower and at all the intermediate filters, ESBA-2 configurations mitigate the NS stroke, compared to all the rest configurations. At the same filter of 45%, as previously, the NS stroke for ESBA-2 at $b_{max} = 0.5$ is 0.062m. Finally, at the highest filters, again ESBA-1 and ESBA-3 coincide and present the lowest value of the NS stroke, at approximately 0.041m. Overall, the addition of the inerter parallel to the positive stiffness element (ESBA-2), has little to no contribution in the structural drifts, but significantly reduces the NS element stroke, especially in the intermediate and low acceleration filter ranges. The ESBA-3 configuration is superior, both in terms of structural drifts and NS stroke, by observing all the filter ranges.

The next figure (Fig. 4.7(a) and (b)) presents the same graphs with optimization curves as in the previous figure (Fig. 4.6). The difference is now that those curves are formulated by considering all the sets of parameters, having been optimized by the one random artificial accelerogram, as fixed data. The scope is now to examine how those particular sets of parameters affect the mean maximum values of the structure's relative to the ground displacement and mean NS stroke over the same absolute acceleration filters with respect to all the artificial accelerograms. As it can be clearly observed, they have the same graphic form of their descending response (in both the relative displacement and NS stroke) with respect to the increase of the acceleration filter. In fact, the only difference is that they exhibit slightly smaller values of their responses at the lowest filters and slightly larger values at the intermediate and highest filters.

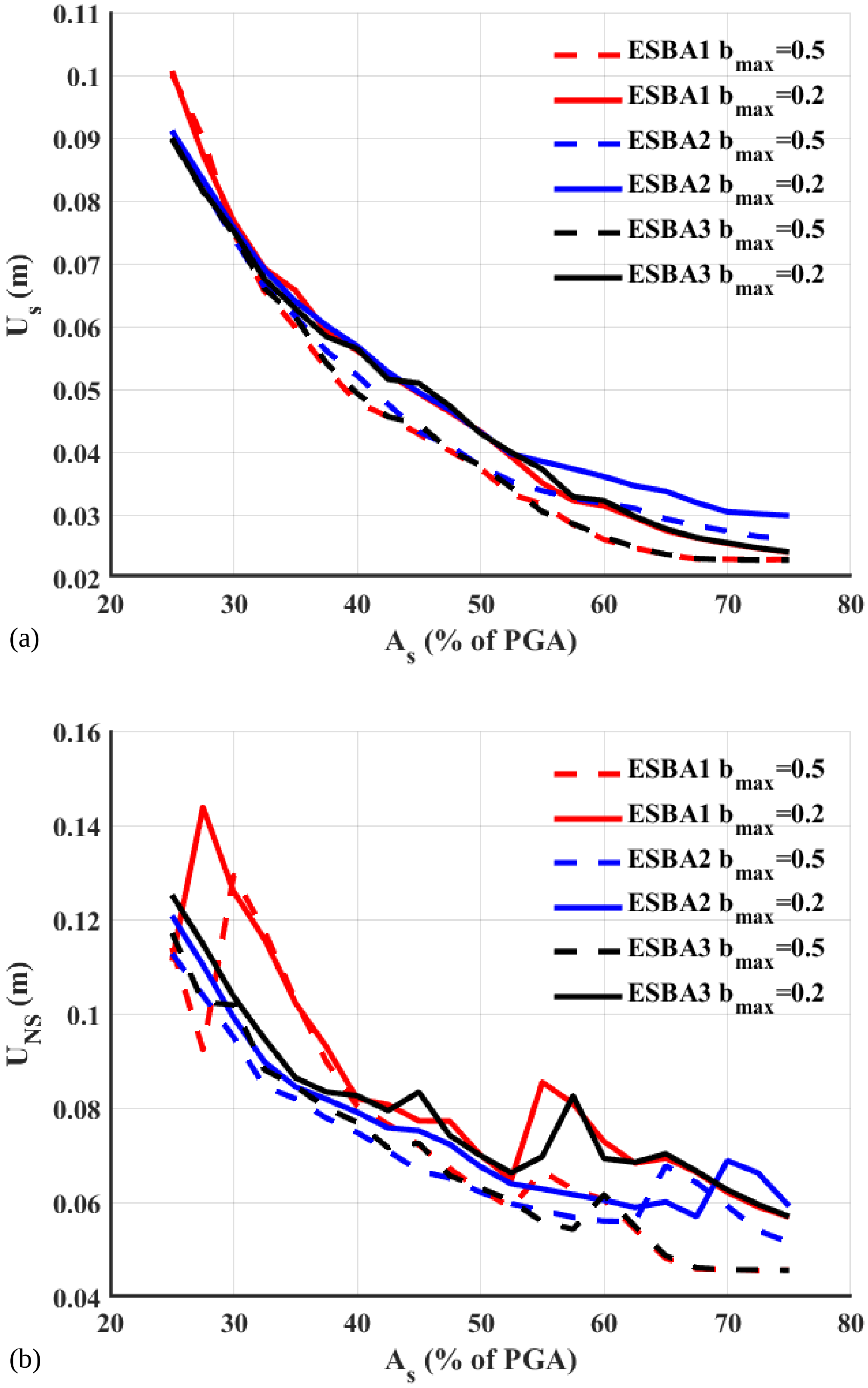

Figure 4.7: (a) Structure relative displacement and (b) NS element stroke maximum values over the structure absolute acceleration (% of PGA), of the ESBA configurations with respect to all artificial accelerograms, for *bmax*=0.2 and *bmax*=0.5 and c_{PS}=100 kNs/m

From the above, it can be detected that all configurations of $b_{max} = 0.5$ display a better dynamic response compared to the case of $b_{max} = 0.2$. Secondly, ESBA-3 can be considered as the most superior of the examined systems, in contrast with the ESBA-1, to some minor degree. Hence, a second optimization procedure is performed with the following different characteristics from the previous optimization process:

- Only the case of $b_{max} = 0.5$ is examined now
- All the parameters are set to be optimized (including the C_{PS}) to investigate the global behavior of the systems
- The total number of iterations remain 100000 for ESBA-1 and ESBA-2 and is raised to 300000 for ESBA-3 as it is pursued to find the best possible optimal sets of the parameters constrained to the same limit ranges

The following figure (Fig. 4.8(a) and (b)) presents the optimized curves. Again, the dynamic responses of the relative to the ground displacement of the structure and the NS stroke are plotted over the structure's absolute acceleration, expressed as a percentage of the PGA of the artificial accelerogram. The global behavior of the curves of both cases are exactly the same as in (Fig. 4.6). That means, with an increase of the filter, there is a decrease in the dynamic response. Moreover, the ESBA-3 configuration displays the best performance in overall. Indicatively, ESBA-1 and ESBA-3 curves coincide in (Fig. 4.8(a)) within the majority of the filters. Only at the lowest filters, ESBA-3 is better. Indicatively, at the lowest filter, all the configurations demonstrate a relative displacement that fluctuates between 0.101m (ESBA-3) and 0.106m (ESBA-1). At intermediate filters (45%-50%) a value just over 0.03m is reached, slightly smaller than of the case with fixed c_{PS} parameter. Finally, at the highest filter the relative displacement is 0.021m, slightly smaller than in the previous case. The same exactly apply to the (Fig. 4.8(b)) compared to that of (Fig. 4.6(b)). ESBA-1 configuration exhibits again the sudden increase and decrease of the NS stroke at the lowest filters with a maximum value of 0.137m. At the same filters, ESBA-2 manages to mitigate the NS stroke to the lowest. At the intermediate and highest filters, ESBA-1 and ESBA-3 coincide attaining the value of 0.033m. However, all the configurations have smoother finishing at the highest filters. So, it is indicated that the optimization of all the parameters (including the c_{PS} parameter) had a minor beneficial impact on the global behavior of the curved. The raising of the maximum number of iterations to 300000 for ESBA-3 appears to not affect the final results, as it coincides with ESBA-1 with 100000 maximum iterations. Thus, it is a rational assumption that 100000 iterations produce accurate results.

In (Fig. 4.9), where all the sets of the optimized parameters are considered as given data, the same dynamic responses are plotted with respect to all the artificial accelerograms. As in the case of (Fig. 4.7) with respect to the (Fig. 4.6), the same can be observed compared to the results of (Fig. 4.8). The same global behavior of all the curves, with slightly decreased values, can be seen.

In general, the optimization procedure gave quite realistic results that can lead to a technological feasible vibration absorption system, which incorporates realizable engineering criteria. The fact that the optimization process, performed with respect to

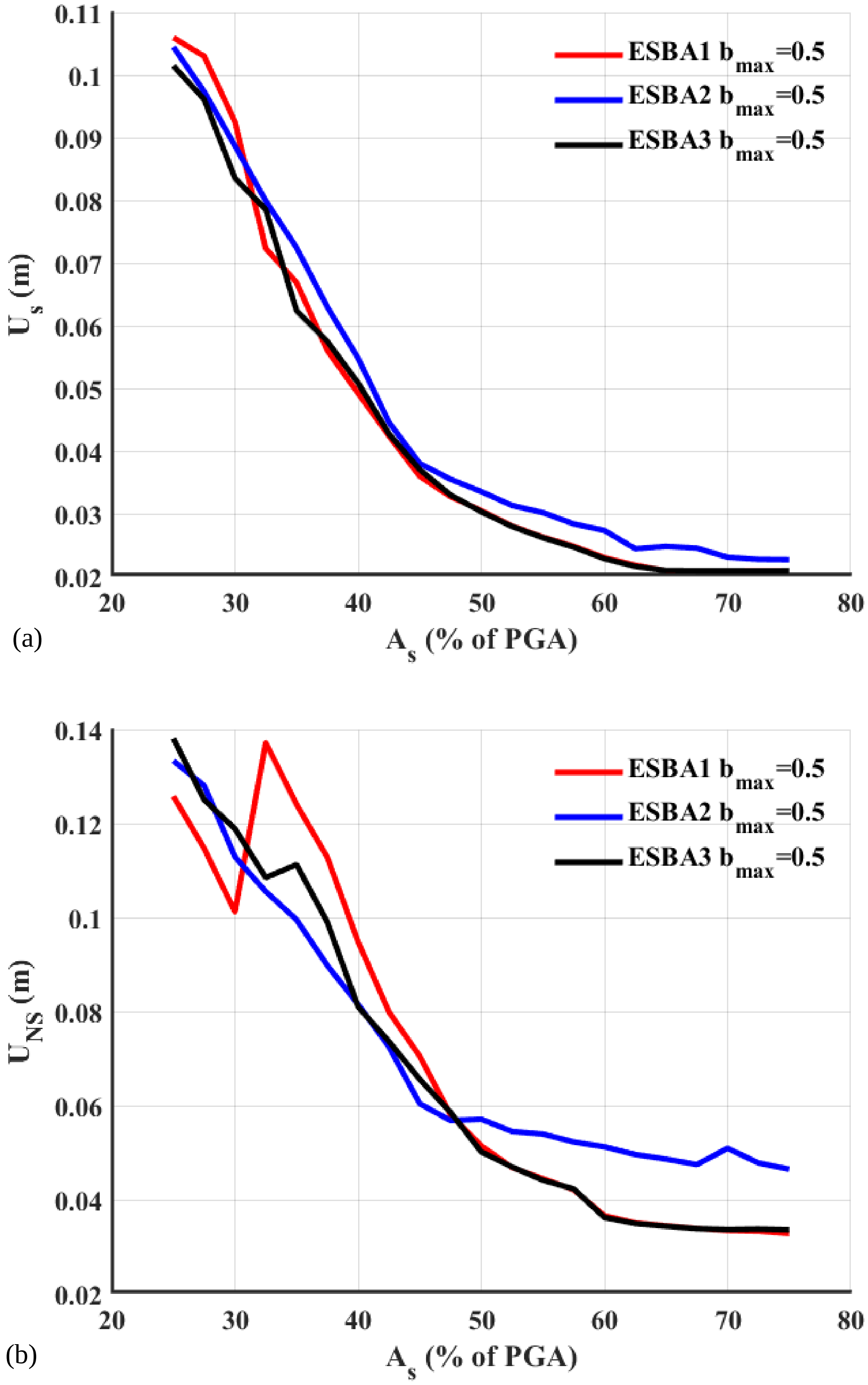

Figure 4.8: (a) Structure relative displacement and (b) NS element stroke maximum values over the structure absolute acceleration (% of PGA), of the ESBA configurations optimized with respect to a random artificial accelerogram, for *bmax*=0.5

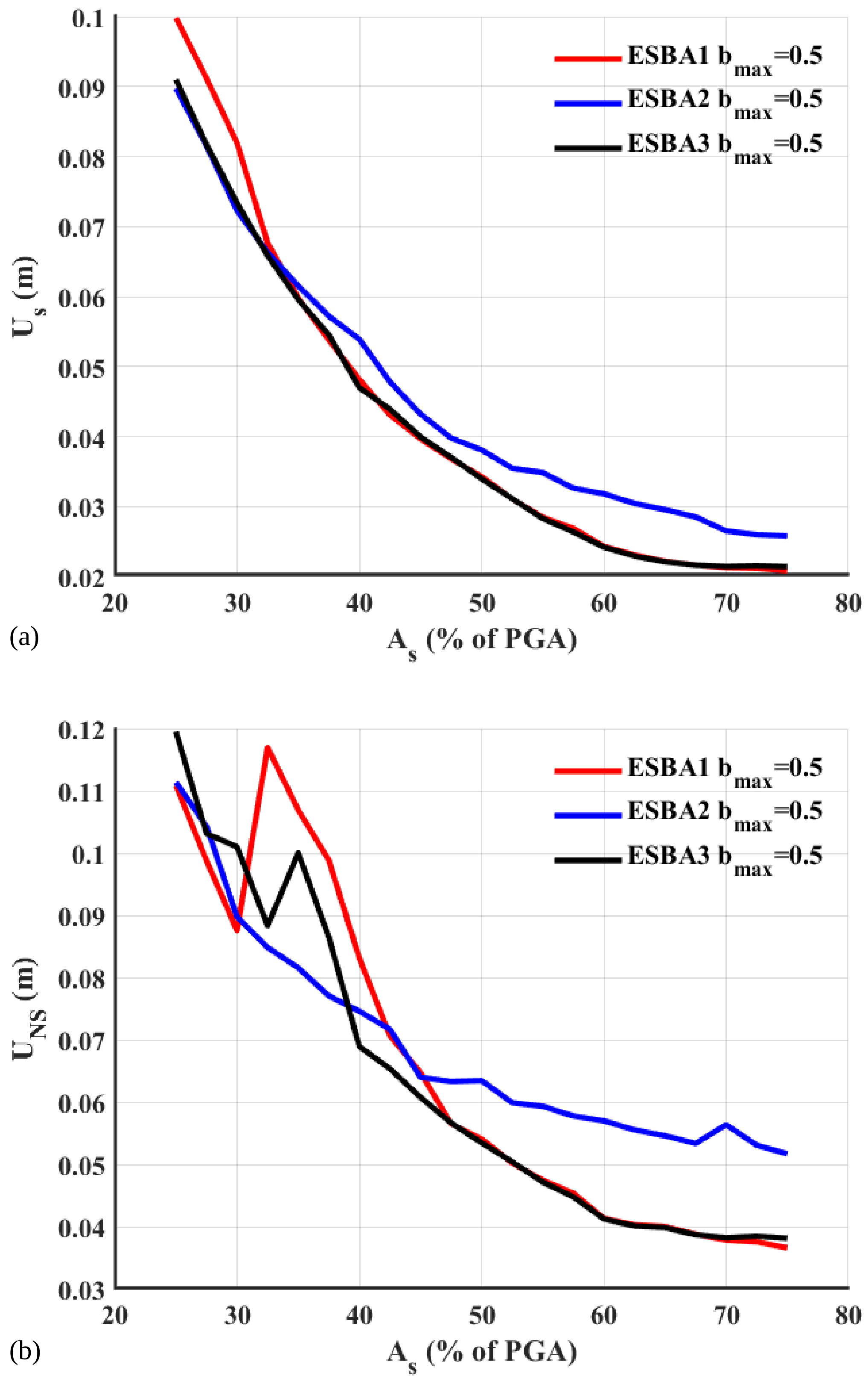

Figure 4.9: (a) Structure relative displacement and (b) NS element stroke maximum values over the structure absolute acceleration (% of PGA), of the ESBA configurations with respect to all artificial accelerograms, for *bmax*=0.5

one artificial accelerogram, gave similar results, with respect to all the artificial accelerograms, states that this procedure noted a stable response.

In the table and figure below (Table 4.4) and (Fig. 4.10), respectively, there are the optimal values and their graphical presentation over the structure's absolute acceleration (% of PGA) of all the parameters of the ESBA-3 configuration. As it can be clearly noted, many of the parameters have reached their lower or upper limit at the intermediate and upper acceleration filters. More particularly, the system's natural frequency (Fig. 4.10(a)) that controls the overall stiffness starts at approximately 0.42Hz, at the lowest filter and ends up to the upper limit of 1.5Hz with an approximate linear behavior. The negative stiffness (Fig. 4.10(b)) starts at -5000kN/m and remains there, until the 40% filter (approximately), then, by following a steep descent it achieves the lower limit (upper absolute limit) of -15000kN/m at the 60% filter and above. The

Table 4.4: Optimal values of parameters over the structure absolute acceleration (% of PGA), of the ESBA-3 configuration (optimized with respect to a random accelerogram for all parameters), for *bmax*=0.5 of (a) f_0, (b) k_{NS}, (c) c_{NS}, (d) c_{PS}, (e) b_R, (f) b_{NS} and (g) b_{PS}

A_S (% of PGA)	f_0 (Hz)	k_{NS} (kN/m)	c_{NS} (kNs/m)	c_{PS} (kNs/m)	b_R (% m_S)	b_{NS} (% m_S)	b_{PS} (% m_S)
25.00	0.4158	-4960.01	468.05	465.00	0.1729	0.1056	0.3150
27.50	0.4169	-5408.41	633.06	382.63	0.2026	0.0780	0.4040
30.00	0.4585	-5335.04	515.30	665.66	0.1903	0.2277	0.2820
32.50	0.4595	-5589.84	706.53	530.17	0.2296	0.1815	0.3126
35.00	0.5625	-4689.89	231.02	780.73	0.2139	0.3930	0.1110
37.50	0.5733	-5024.40	332.26	846.20	0.2435	0.4100	0.1582
40.00	0.6032	-6010.78	660.33	756.35	0.3145	0.3754	0.1464
42.50	0.6902	-5778.11	505.04	865.06	0.3269	0.4223	0.0819
45.00	0.7597	-6409.01	551.66	815.78	0.4557	0.3949	0.0759
47.50	0.8443	-6756.17	507.71	891.35	0.4999	0.4101	0.0403
50.00	0.9220	-10702.50	840.51	895.72	0.4993	0.2113	0.0001
52.50	0.9862	-12316.63	891.92	898.64	0.4978	0.2304	0.0000
55.00	1.0534	-13069.95	899.70	898.88	0.4994	0.2858	0.0003
57.50	1.1089	-13411.28	882.49	898.29	0.4986	0.3375	0.0003
60.00	1.2566	-14978.49	897.18	899.93	0.4995	0.2781	0.0010
62.50	1.3795	-14980.67	777.78	898.62	0.4992	0.2690	0.0011
65.00	1.4981	-14980.41	649.89	894.28	0.4991	0.2526	0.0002
67.50	1.4996	-14968.41	669.29	899.60	0.4999	0.2780	0.0002
70.00	1.5000	-14996.71	678.93	897.88	0.4990	0.2887	0.0006
72.50	1.4999	-14994.91	675.28	898.58	0.5000	0.2821	0.0001
75.00	1.5000	-14988.59	679.43	899.82	0.4998	0.2911	0.0004

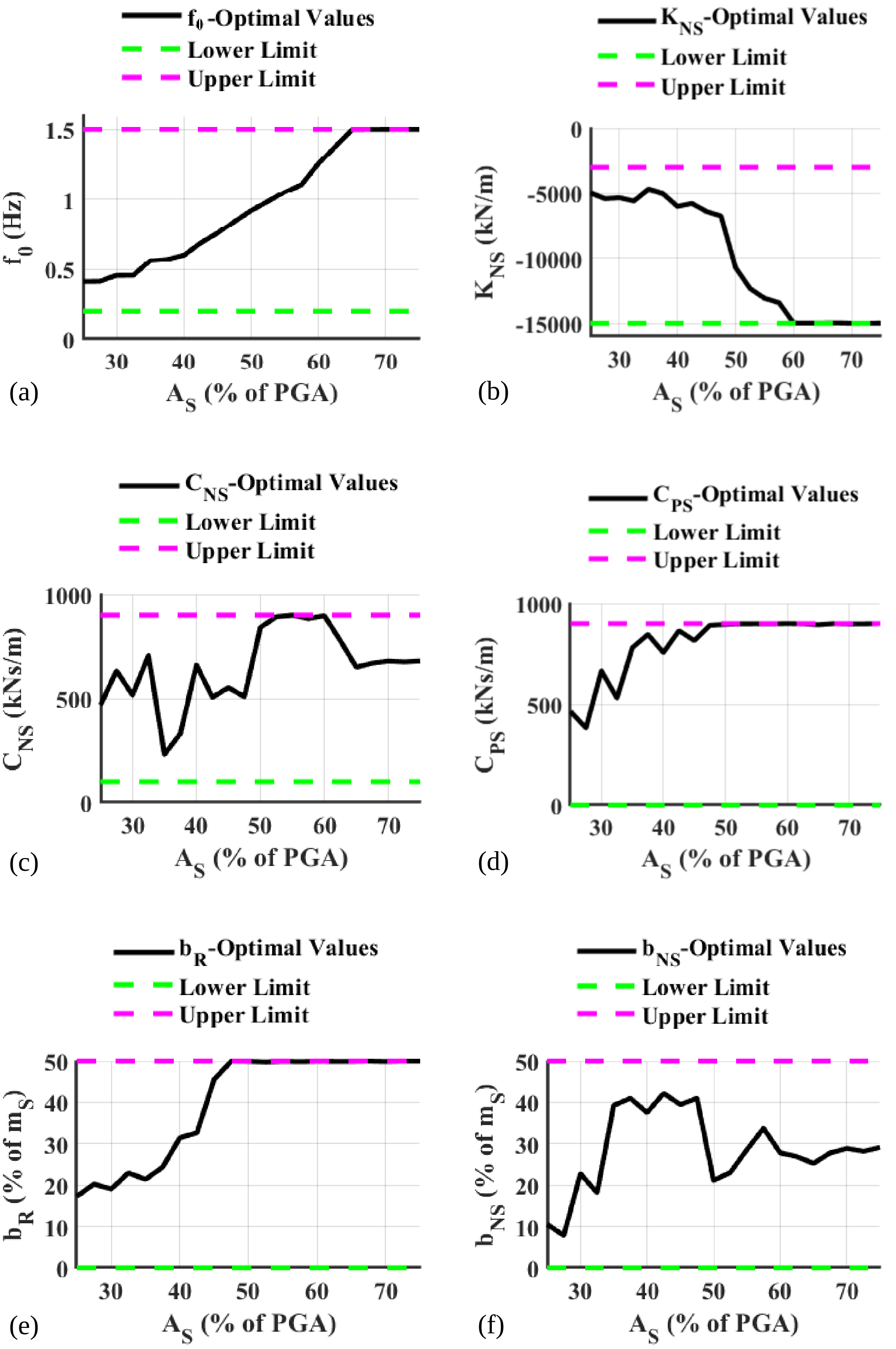
f0-Optimal Values
Lower Limit
Upper Limit
f0 (Hz)
1.5
1
0.5
0
30
40
50
60
70
(a)
AS (% of PGA)
KNS-Optimal Values
Lower Limit
Upper Limit
KNS (kN/m)
0
-5000
-10000
-15000
30
40
50
60
70
(b)
AS (% of PGA)
CNS-Optimal Values
Lower Limit
Upper Limit
CNS (kNs/m)
1000
500
0
30
40
50
60
70
(c)
AS (% of PGA)
CPS-Optimal Values
Lower Limit
Upper Limit
CPS (kNs/m)
1000
500
0
30
40
50
60
70
(d)
AS (% of PGA)
bR-Optimal Values
Lower Limit
Upper Limit
bR (% of mS)
50
40
30
20
10
0
30
40
50
60
70
(e)
AS (% of PGA)
bNS-Optimal Values
Lower Limit
Upper Limit
bNS (% of mS)
50
40
30
20
10
0
30
40
50
60
70
(f)
AS (% of PGA)

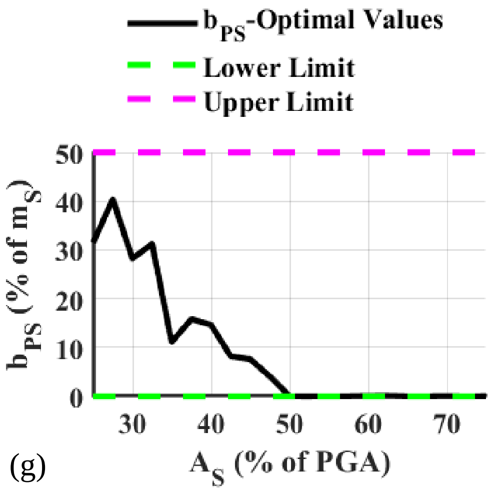

Figure 4.10: Optimal values of parameters over the structure absolute acceleration (% of PGA), of the ESBA-3 configuration (optimized with respect to a random accelerogram for all parameters), for *bmax*=0.5 of (a) f_0, (b) k_{NS}, (c) c_{NS}, (d) c_{PS}, (e) b_R, (f) b_{NS} and (g) b_{PS}

next parameter, that of the damping parallel to the negative stiffness element (Fig. 4.10(c)), notes a more random distribution across all filters. It fluctuates from 230kNs/m (at 35% filter) to the upper limit (from 50% to 60%). The other damping parameter (Fig. 4.10(d)), starts at approximately 500kNs/m and gradually ends up to the upper limit of 900kNs/m at the 47.5% filter and so on. A similar form, with a more exponential transition, from the start of 20% approximately, to the upper limit of 50% at the same filter of 47.5% is developed by the external inerter b_R, in (Fig. 4.10(e)). The inerter between the structure and the oscillating mass (Fig. 4.10(f)), follows a random distribution in the various filters, without achieving its range limits. It closely fluctuates from 10% to 40%. Finally, the inerter of the oscillating mass b_{PS} in (Fig. 4.10(g)), reversely escalates from 32% to 0% at the 50% filter. It maintains this value until the last filter. This clearly indicates that from a point and beyond, this inerter has no contribution to the system. That is why ESBA-1 and ESBA-3 curves coincide at this point. By examining the overall behavior, many parameters, reaching their limits, have the tendency to exceed those values and possibly attaining an even better behavior. However, since the desired performance is to be achieved within engineering and constructional limitations, those values become optimal considering the imposed constraints.

4.4 Time history analysis of SDoF system controlled with ESBA-3

4.4.1 Comparison with conventional base isolation

In order to check the effectiveness of the ESBA-3 configuration, time history responses of the structure's relative to the ground displacement, the structure's absolute acceleration and the shear base are compared to the equivalent responses of conventional base isolation systems. Those dynamic responses are due to the same random accelerogram with which the optimization processes are performed. From all the sets of the optimal values of the ESBA-3 system, those that correspond to the intermediate value of acceleration filter of 50% are chosen. The ESBA-3 configuration is compared to an SDoF system with a conventional base isolation, which satisfies the equation (4.24) (in analogy with Eq. (4.3)) of a one degree of freedom. In order to achieve same-size comparisons, the base isolation systems are considered to have the same natural frequency, that of $f_0 = 0.922Hz$, (according to Table 4.4) for 50% acceleration filter. In analogy to (Eq. 4.16), the stiffness of the base isolation system emerges from the following relation:

$$k_{BI} = m_s(2\pi f_0)^2 \tag{4.30}$$

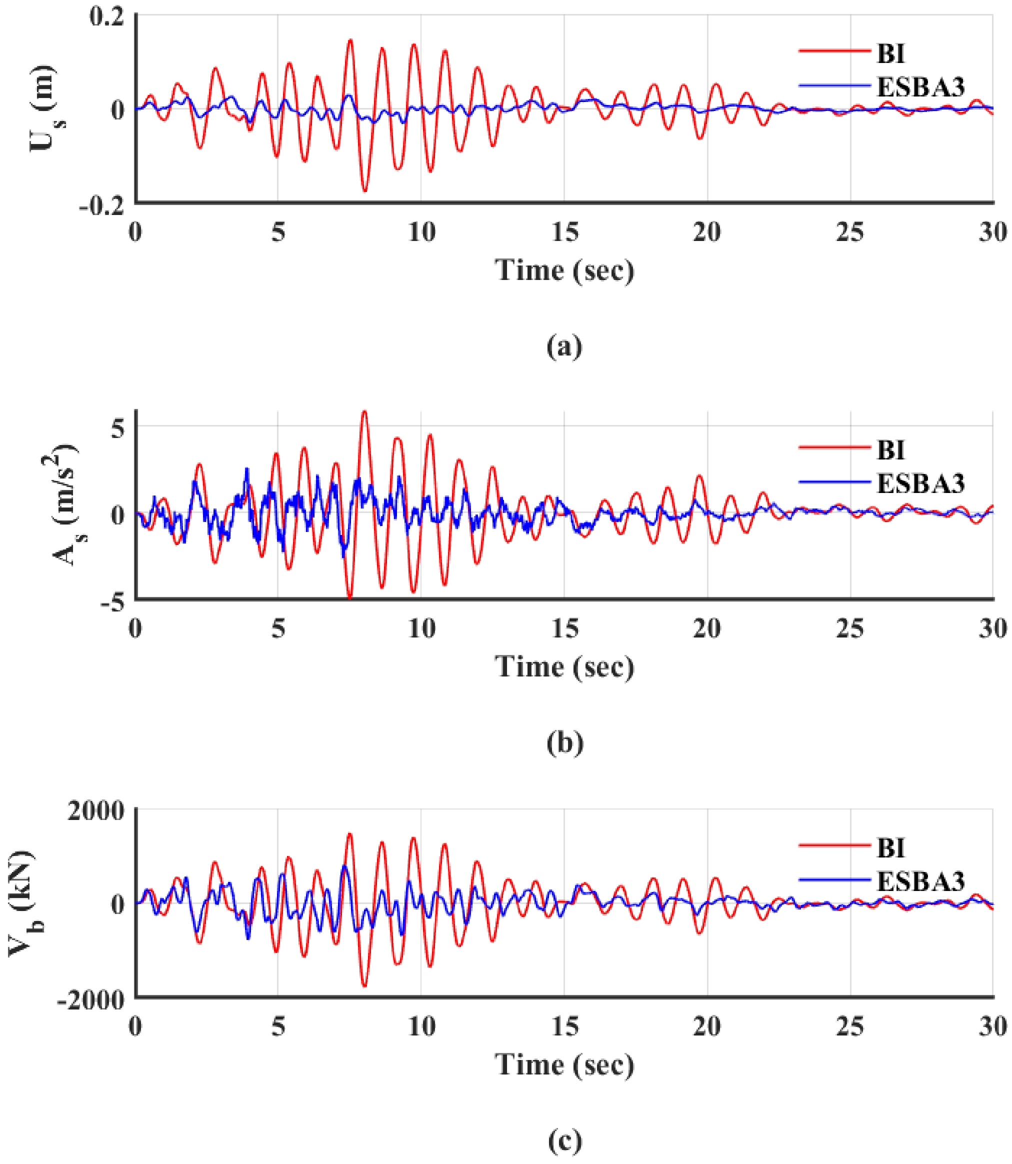

(a)

(b)

(c)

Figure 4.11: Dynamic responses, in terms of structure's (a) relative to the ground displacement, (b) absolute acceleration and (c) base shear of the ESBA-3 vibration absorber and a conventional base isolated structure (BI)

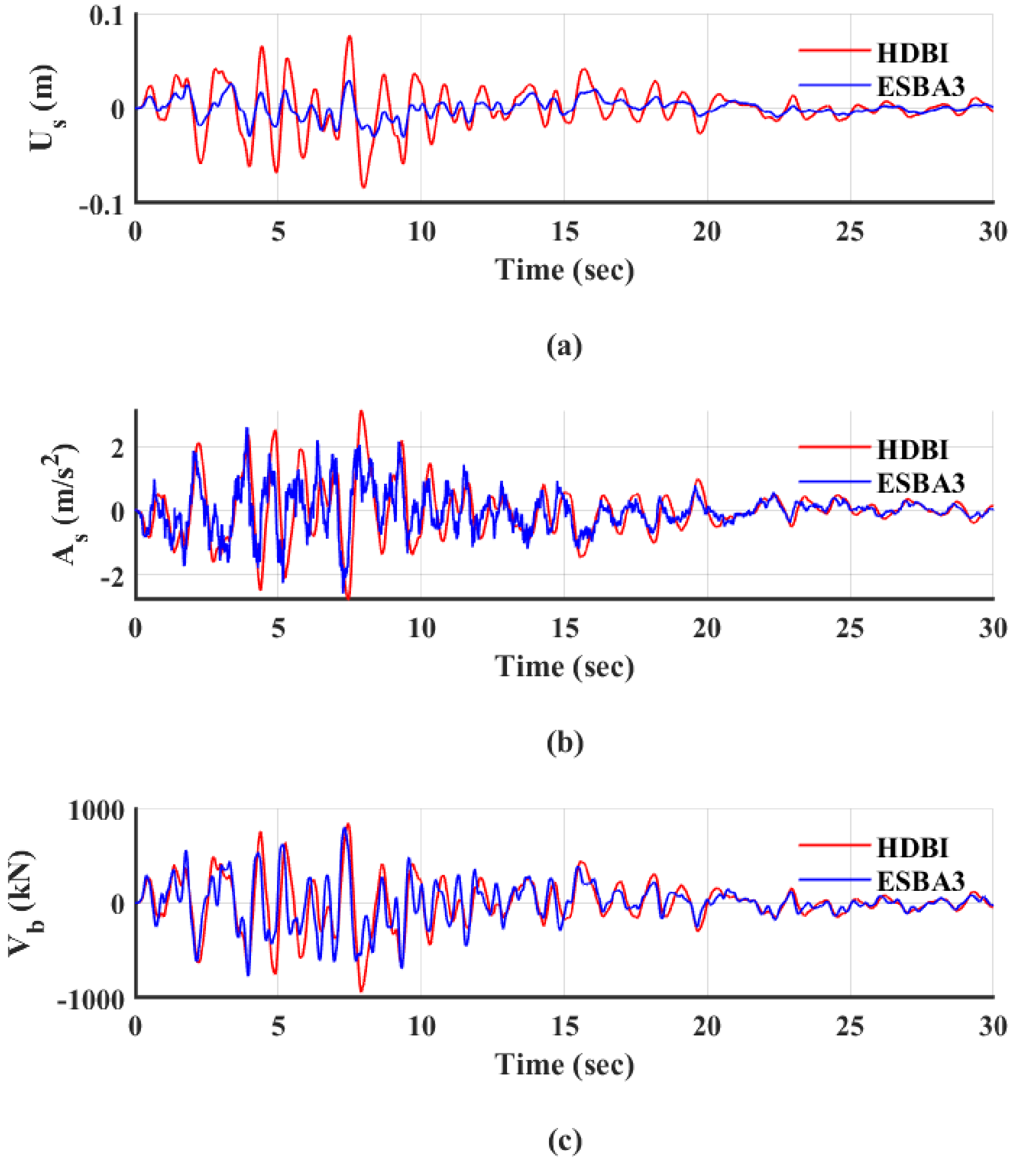

(a)

(b)

(c)

Figure 4.12: Dynamic responses, in terms of structure's (a) relative to the ground displacement, (b) absolute acceleration and (c) base shear of the ESBA-3 vibration absorber and a conventional highly damped base isolated structure (HDBI)

Where, m_S is the same total reference mass of the structure of 300 Mgr. Finally, the damping can be computed from the equation below:

$$c_{BI} = 2m_S(2\pi f_0)\zeta_{BI} \tag{4.31}$$

where ζ_{BI} is the damping ratio of the base isolation system. The value 5% can be considered for the case of the conventional base isolation system (BI), while that of 20% can be adopted for the highly damped base isolation system (HDBI).

From the first figure (Fig. 4.11(a)), can be clearly observed that the relative to the ground displacement of the structure develops into 0.175m for the case of the BI system, while that of the ESBA-3 configuration is 0.03m. That means, ESBA-3 system notes 82.86% reduction at this response. Meanwhile, HDBI, in (Fig. 4.12(a)), system notes a maximum relative displacement of 0.084m. Again, ESBA-3 configuration's response is 64.29% less than that. In (Fig. 4.11(b)) and (Fig. 4.12(b)) the absolute acceleration of both the base isolation systems is 5.90 m/s^2 (BI) and 3.14 m/s^2 (HDBI). ESBA-3 yielded an absolute acceleration of 2.61 m/s^2, which is less than that of the BI by 55.76% and than HDBI by 16.88%. Finally, the base shear can by defined from the following relations:

$$V_{b,ESBA-3} = k_R u_S + k_{PS} u_D + c_{PS} \dot{u}_D + b_R \ddot{u}_S + b_{PS} \ddot{u}_D \tag{4.32a}$$

$$V_{b,BI} = k_{BI} u_S + c_{BI} \dot{u}_S \tag{4.32b}$$

Equation (4.32a) refers to the shear base of the ESBA-3 configuration, while (Eq. 4.32b) corresponds to same quantity of the conventional base isolation. From (Fig. 4.11(c)) and (Fig. 4.12(c)), the maximum values of the base shear is 1769.1kN and 942.4kN for the BI and HDBI, respectively. ESBA-3 base shear configures at 796kN, which means that this quantity is reduced by 55% and 15.53%, respectively for both cases, with the presence of ESBA-3 system. It is observed that the ESBA-3 manages to significantly reduce all the dynamic responses of the structure, as compared to the BI and HDBI system approach.

4.4.2 Dynamic responses from real seismic excitations

Real earthquake ground excitations are not stationary and do not have a fixed duration, as in the case of spectrum compatible artificial accelerograms, that are used for the design of the proposed ESBA. For this reason, it is very important to examine the effectiveness of the proposed vibration absorbers (ESBA), also with real earthquake records. In this thesis, 24 real earthquake records are selected, based on the work of (Kapasakalis, Antoniadis, & Sapountzakis, Constrained optimal design of seismic base absorbers based on an extended KDamper concept, 2021). They are widely used in the literature and are known to have had a devastating impact on structural systems. The table that follows (Table 4.5) presents the details of each ground motion. This table incorporates data that refer to the name of each seismic event, the year it occurred, the station that recorded the acceleration data, its moment magnitude scale, its PGA in g and its epicentral distance in km. The last characteristic can classify the earthquakes into two categories. Earthquakes with an epicentral distance R_{jb} of fewer than 25 km, are classified as near-fault earthquakes (NF). From the other extreme, earthquakes whose epicentral distance is larger than that of 25 km, are classified as far-fault earthquakes (FF).

In order to check the effectiveness of the proposed vibration absorption system, the same ESBA-3 configuration system with the optimal values that correspond to the 50% acceleration filter (as in the case of section 4.4.1), is compared with a conventional base isolation system (BI) and a highly damped base isolation system (HDBI), with the exact same characteristics (same natural frequency, mass (and stiffness) and damping) as in

Table 4.5: List and information on the considered real earthquake records

No	Earthquake	Year	Station	Mw	PGA (g)	R_{jb} (km)
1	Northridge-N	1994	N Hollywood	6.69	0.3087	7.89
2	Northridge-F	1994	Montebello	6.69	0.1756	43.22
3	Loma Prieta-N	1989	Corralitos	6.93	0.6447	0.16
4	Loma Prieta-F	1989	APEEL 10-Skyline	6.93	0.1029	41.88
5	L’Aquila-N	2009	V. Aterno	6.3	0.4018	0.0
6	L’Aquila-F	2009	Ortucchio	6.3	0.0655	35.07
7	Chi-Chi-N	1999	CHY006	7.62	0.3587	9.76
8	Chi-Chi-F	1999	CHY012	7.62	0.0626	59.04
9	Kocaeli-N	1999	Izmit	7.51	0.1651	3.62
10	Kocaeli-F	1999	Fatih	7.51	0.1618	53.34
11	Tabas-N	1978	Tabas	7.35	0.854	1.79
12	Tabas-F	1978	Ferdows	7.35	0.0931	89.76
13	Kobe-N	1995	Amagasaki	6.9	0.2758	11.34
14	Kobe-F	1995	HIK	6.9	0.1394	95.72
15	Kozani-N	1995	Kozani	6.4	0.2069	14.13
16	Kozani-F	1995	Larisa	6.4	0.031	74.06
17	Niigata-N	2004	NIG017	6.63	0.3781	4.22
18	Niigata-F	2004	FKS020	6.63	0.043	101.78
19	Landers-N	1992	Joshua tree	7.28	0.2736	11.03
20	Landers-F	1992	Boron fire station	7.28	0.1189	89.69
21	Duzce-N	1999	Lamont 1059	7.14	0.1524	4.17
22	Duzce-F	1999	Mudurnu	7.14	0.1203	34.3
23	Friuli-N	1976	Tolmezzo	6.5	0.3571	14.97
24	Friuli-F	1976	Barcis	6.5	0.0292	49.13

the case of the section 4.4.1. The same natural frequency is chosen so that all the systems can have equal comparison basis.

The system main dynamic responses, in terms of structural relative to the ground displacements (drifts), structural absolute acceleration, total base shear and generated NS element stroke are presented in Figures 4.13 and 4.14, for all the selected real near and far fault earthquake records, respectively, presented in Table 4.5.

As it can be clearly observed, the ESBA-3 manages to reduce the structural drifts in all the earthquakes in both the NF and FF cases, compared with the equivalent response of the BI and HDBI. Indicatively, Kobe-N, with a PGA of 0.276g, seems to induce the

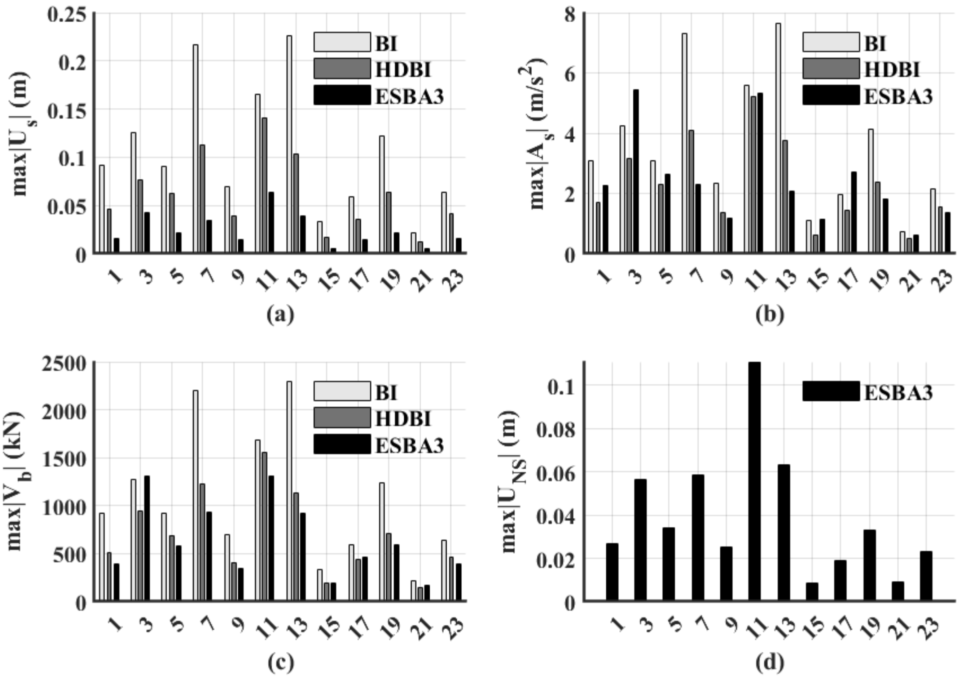

Figure 4.13: Main dynamic responses, (a) structural drift, (b) absolute acceleration, (c) base shear and (d) NS stroke of the controlled structure with conventional BI, a highly damper BI (HDBI) and with the ESBA-3 configuration, for all the near fault real earthquake records

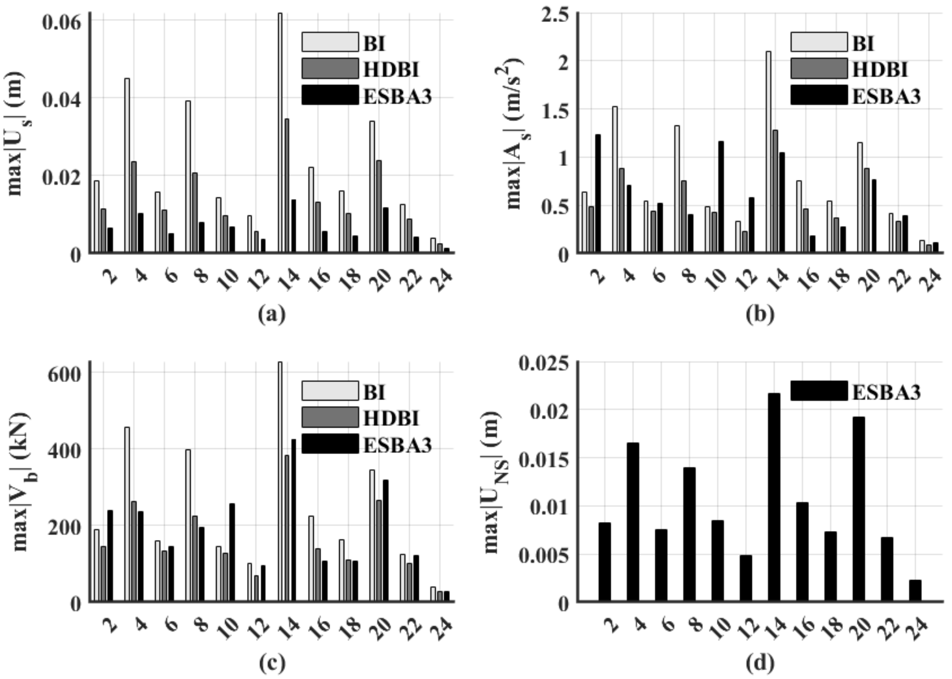

Figure 4.14: Main dynamic responses, (a) structural drift, (b) absolute acceleration, (c) base shear and (d) NS stroke of the controlled structure with conventional BI, a highly damper BI (HDBI) and with the ESBA-3 configuration, for all the far fault real earthquake records

largest structural drift of 0.226 m to the BI system. Increasing the damping ratio from 5% to 20%, which corresponds to the HDBI case, the structural drift drops to 0.104 m. However, ESBA-3 manages to keep the drift at the value of 0.039 m, which is lower by the drifts of BI and HDBI by 82.74% and 62.5%, respectively (Fig. 4.13(a)). In (Fig. 4.14(a)) there are the drifts of the FF earthquakes. Again, Kobe-F with a PGA of 0.139g causes the largest drift in BI, by 0.062 m. HDBI notes a drift of 0.035 m, while ESBA-3 a small value of 0.014 m. That means, ESBA-3 achieves a reduction of 77.42% and 60% of the BI and HDBI drifts, respectively.

In terms of the absolute acceleration, according to (Fig. 4.13(b)), approximately in half of the NF earthquakes, the ESBA-3 configuration manages to present the lowest values. In the rest of the NF earthquakes, it maintains the absolute acceleration at acceptable levels, by slightly exceeding the values of the same response of the BI and HDBI systems. In the same earthquake, BI system notes an absolute acceleration of 7.64 m/s^2, HDBI 3.76 m/s^2 and ESBA-3 a value of 2.09 m/s^2. ESBA-3 achieves a decrease by 72.64% and 44.41% with respect to the BI and HDBI systems. In (Fig. 4.14(b)), the values of the absolute acceleration for the same vibrations systems of BI, HDBI and ESBA-3 are 2.10 m/s^2, 1.27 m/s^2 and 1.04 m/s^2, respectively. The proposed system’s response is lower by 50.48% and 18.11% than that of the BI and HDBI.

According to (Fig. 4.13(c)) and (Fig. 4.14(c)), the base shear of the ESBA configuration is lower than that of the BI system at the majority of the earthquakes. At very few cases there is a minor exceedance of the value of the BI or HDBI system, which means that ESBA-3 maintains once more this response at acceptable levels. More specifically, the base shear of the BI, due to the same earthquake (No 13), is approximately 2292 kN, for the HDBI lies on the value of 1129 kN and for ESBA-3 is configured at 920 kN. Again, the ESBA system notes a reduction by 59.86% and 18.51% compared to the values of BI and HDBI, respectively. For the earthquake No14 the same responses are 629 kN, 382 kN and 426 kN for the BI, HDBI and ESBA-3 systems. The response of ESBA-3 configuration is 32.27% lower than that of BI, but 10.33% higher than that of HDBI.

Finally, by observing the figures (Fig. 4.13(d)) and (Fig. 4.14(d)), the NS element stroke reached the maximum values of 0.111 m for the NF earthquakes (corresponding to the Tabas-N earthquake with the highest PGA of 0.854g) and 0.022 m for all the FF cases, with that value corresponding to the same No 14 earthquake. As reflected from the (d) plot of the figures 4.13 and 4.14, the NS stroke fluctuated within reasonable ranges.

Overall, it is observed that the ESBA manages to significantly reduce the structural drifts and at the same time is able to maintain acceptable levels of structure absolute accelerations and base shears. The NS stroke did not surpass the stricter limit of 15 cm and obviously the more tolerant limit of 20 cm that was imposed during the optimization procedures.

5 PERFORMANCE ASSESSMENT OF THE ESBA-3 CONFIGURATION AS A SEISMIC PROTECTION SYSTEM FOR MULTISTORY BUILDING STRUCTURES

5.1 ESBA-3 configuration as a seismic protection device for SDoF systems

To examine MDoF systems (multi-story buildings) controlled by ESBA configurations, an expansion of the suggested vibration control approach is necessary. In order to achieve this, it is first demonstrated how the optimal configuration of ESBA-3, as outlined in Section 4.4, which was initially developed for a simplified 2-DoF system, can be implemented for MDoF systems. As in the work of (De Domenico & Ricciardi, 2018), at first, an SDoF flexible structure on a fixed base is considered (Fig. 5.1(a)). Its characteristics are its total mass m_S, damping coefficient c_S and stiffness k_S. If the structure is subjected to a ground excitation x_g, then the equation of motion is the following (in analogy to equations 4.3 and 4.24):

$$m_S\ddot{u}_S + c_S\dot{u}_S + k_S u_S = -m_S\ddot{x}_g \tag{5.1}$$

Where, $u_S = x_S - x_g$ is the relative to the ground displacement of the structure and x_S is the total displacement of the structure.

Then, the same flexible structure is mounted on a conventional or highly damped isolation base (Fig. 5.1(b)), which is another SDoF system. If again, the coupled, now, system is subjected to the same ground excitation, the equations of motions are:

$$m_S(\ddot{u}_S + \ddot{u}_B) + c_S\dot{u}_S + k_S u_S = -m_S\ddot{x}_g \tag{5.2a}$$

$$m_B\ddot{u}_B + m_S(\ddot{u}_S + \ddot{u}_B) + c_B\dot{u}_B + k_B u_B = -(m_S + m_B)\ddot{x}_g \tag{5.2b}$$

The quantities of m_B, c_B and k_B are the mass, the damping coefficient and the stiffness of the base isolation. The displacement of u_S is expressed, now, as the structure's relative to the base displacement and equals to $x_S - x_B$. The term $u_B = x_B - x_g$ and is the relative to the ground displacement of the base.

Finally, the same flexible structure is mounted on the extended seismic stiff base absorber configuration 3 (ESBA-3), which is now as an alternative base to the conventional or the highly damped isolation base (Fig. 5.1(c)). If the system is now subjected to the same ground excitation, its equations of motion will be the ones below, following the same logic as in the equations (5.2):

$$m_S(\ddot{u}_S + \ddot{u}_B) + c_S\dot{u}_S + k_S u_S = -m_S\ddot{x}_g \tag{5.3a}$$

$$\begin{gathered} m_B\ddot{u}_B + m_S(\ddot{u}_S + \ddot{u}_B) + (b_R m_{tot})\ddot{u}_B + (b_{NS} m_{tot})(\ddot{u}_B - \ddot{u}_D) + c_{NS}(\dot{u}_B - \dot{u}_D) \\ +k_R u_B + k_{NS}(u_B - u_D) = -m_{tot}\ddot{x}_g \end{gathered} \tag{5.3b}$$

$$\begin{gathered} m_D\ddot{u}_D - (b_{NS} m_{tot})(\ddot{u}_B - \ddot{u}_D) - c_{NS}(\dot{u}_B - \dot{u}_D) - k_{NS}(u_B - u_D) + (b_{PS} m_{tot})\ddot{u}_D \\ +c_{PS}\dot{u}_D + k_{PS} u_D = -m_D\ddot{x}_g \end{gathered} \tag{5.3c}$$

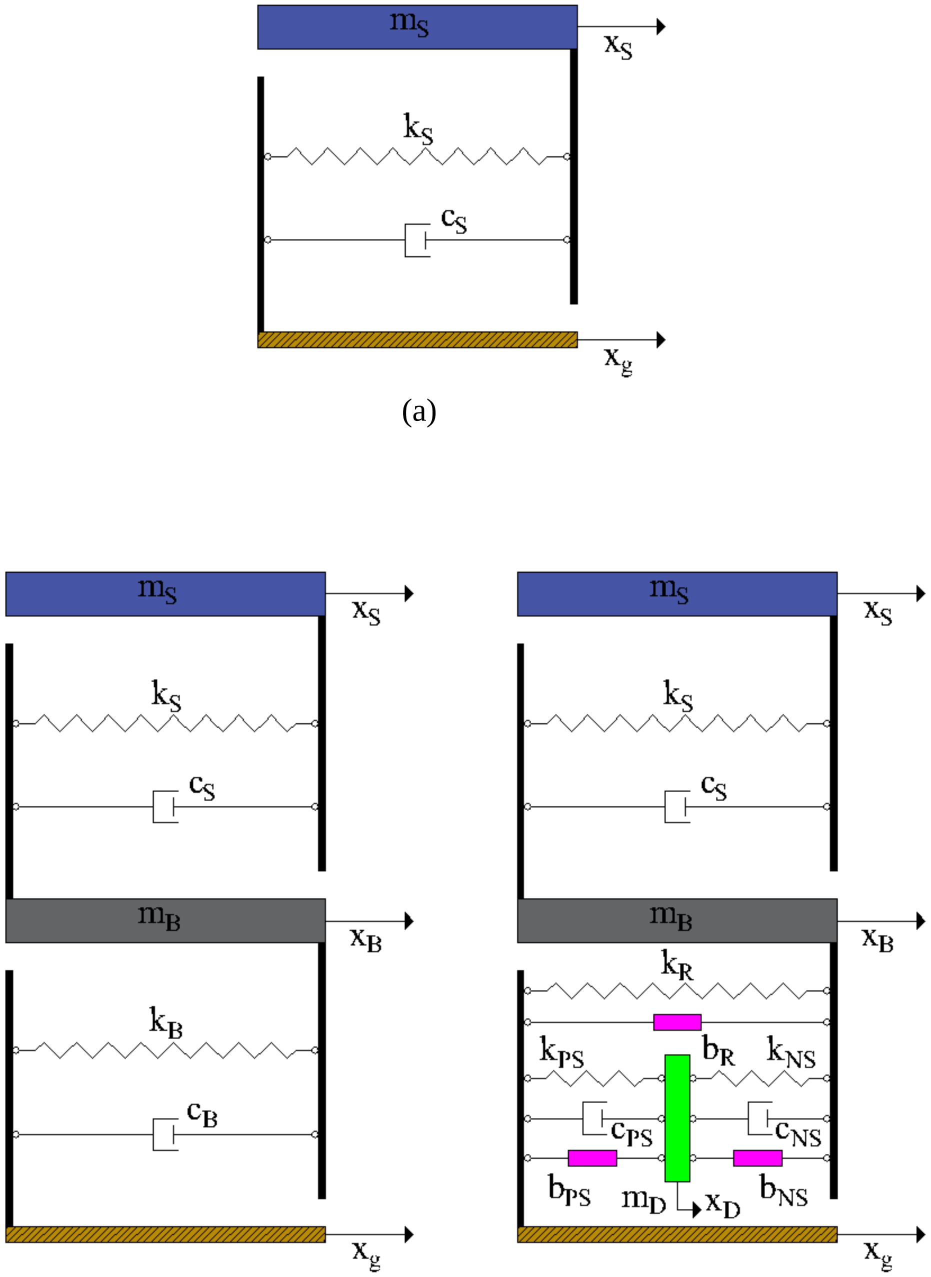

(a)

(b)

(c)

Figure 5.1: (a) Flexible structure on a fixed base, (b) flexible structure on a conventional or highly damped isolation base and (c) flexible structure on the extended seismic stiff base absorber configuration 3 (ESBA-3)

From the equations 5.3a-5.3c, $m_{tot} = m_S + m_B$ is the total mass of the structure, including both the mass of the superstructure (flexible structure) and the mass of the base, b_R, b_{NS} and b_{PS} are the inertance coefficients of the inerters that are located between the base and the structure, parallel to the negative stiffness and parallel to the positive stiffness elements, respectively. Again, the inertance coefficients are expressed as percentage of the total mass m_{tot}. The terms c_{NS} and c_{PS} are the damping coefficients that are parallel to the negative stiffness and parallel to the positive stiffness elements, respectively. Eventually, the terms k_R, k_{NS} and k_{PS} are the stiffness of the base, the negative and positive stiffness, respectively. The m_D quantity is the mass of the oscillating mass and $u_D = x_D - x_g$ is the relative to the ground displacement of the oscillating mass.

5.2 Extension of ESBA-3 configuration as a seismic protection for MDoF systems

In (Fig. 5.2(a)) and (Fig. 5.2(b)), a planar multi-story building, with n degrees of freedom, is modeled mounted on a conventional or highly damped base isolation and on the extended seismic stiff base absorption configuration 3 (ESBA-3), respectively. By adopting some assumptions as made in (Katsikadelis, 2020), including a preliminary static condensation method, which is applied to eliminate the (zero-mass) rotational degrees of freedom, the superstructure is modeled as follows:

- The total mass of the superstructure is concentrated at the floor levels.
- The slabs of the floors are considered rigid, as compared to the columns.
- The columns are inextensible and weightless, thus contributing only to the lateral stiffness.
- The interaction of the soil to the structure is not taken into account.
- The structure is considered to function within the elastic range.

From the aforementioned assumptions, the superstructure has n dynamic degrees of freedom, which equal to the total number of floors. They are represented by the horizontal displacements of the floor masses $m_{Sj} = 1,2,\dots,n$ and are collected into the vector $\boldsymbol{u_{Sr}}(t) = [u_{Sr1}(t)\ u_{Sr2}(t)\ \dots\ u_{Srn}(t)]^T$. The index r denotes the relative to the base displacement of the structure. The equations (5.2) and (5.3) still hold for MDoF systems. By considering the same ground excitation x_g, the matrices of the equation of motion are the following (in exact analogy of equation 4.3):

$$\boldsymbol{M}^{BI}_{(r_{BI})x(r_{BI})} = \begin{bmatrix} \boldsymbol{M}_{S,(n)x(n)} & \boldsymbol{M}_{S,(n)x(n)}\boldsymbol{\tau}_{S,(n)x(1)} \\ \boldsymbol{\tau}^T_{S,(1)x(n)}\boldsymbol{M}_{S,(n)x(n)} & m_B + m_{S,tot} \end{bmatrix}$$

$$\boldsymbol{C}^{BI}_{(r_{BI})x(r_{BI})} = \begin{bmatrix} \boldsymbol{C}_{S,(n)x(n)} & \boldsymbol{0}_{(n)x(1)} \\ \boldsymbol{0}_{(1)x(n)} & c_B \end{bmatrix}$$

$$\boldsymbol{K}^{BI}_{(r_{BI})x(r_{BI})} = \begin{bmatrix} \boldsymbol{K}_{S,(n)x(n)} & \boldsymbol{0}_{(n)x(1)} \\ \boldsymbol{0}_{(1)x(n)} & k_B \end{bmatrix}$$

$$\boldsymbol{\tau}^{BI}_{(r_{BI})x(1)} = \begin{bmatrix} \boldsymbol{M}_{S,(n)x(n)}\boldsymbol{\tau}_{S,(n)x(1)} \\ m_B + m_{S,tot} \end{bmatrix}$$

$$\boldsymbol{u}^{BI}_{(r_{BI})x(1)}(t) = \begin{bmatrix} \boldsymbol{u}_{Sr,(n)x(1)}(t) \\ u_B(t) \end{bmatrix} \tag{5.4}$$

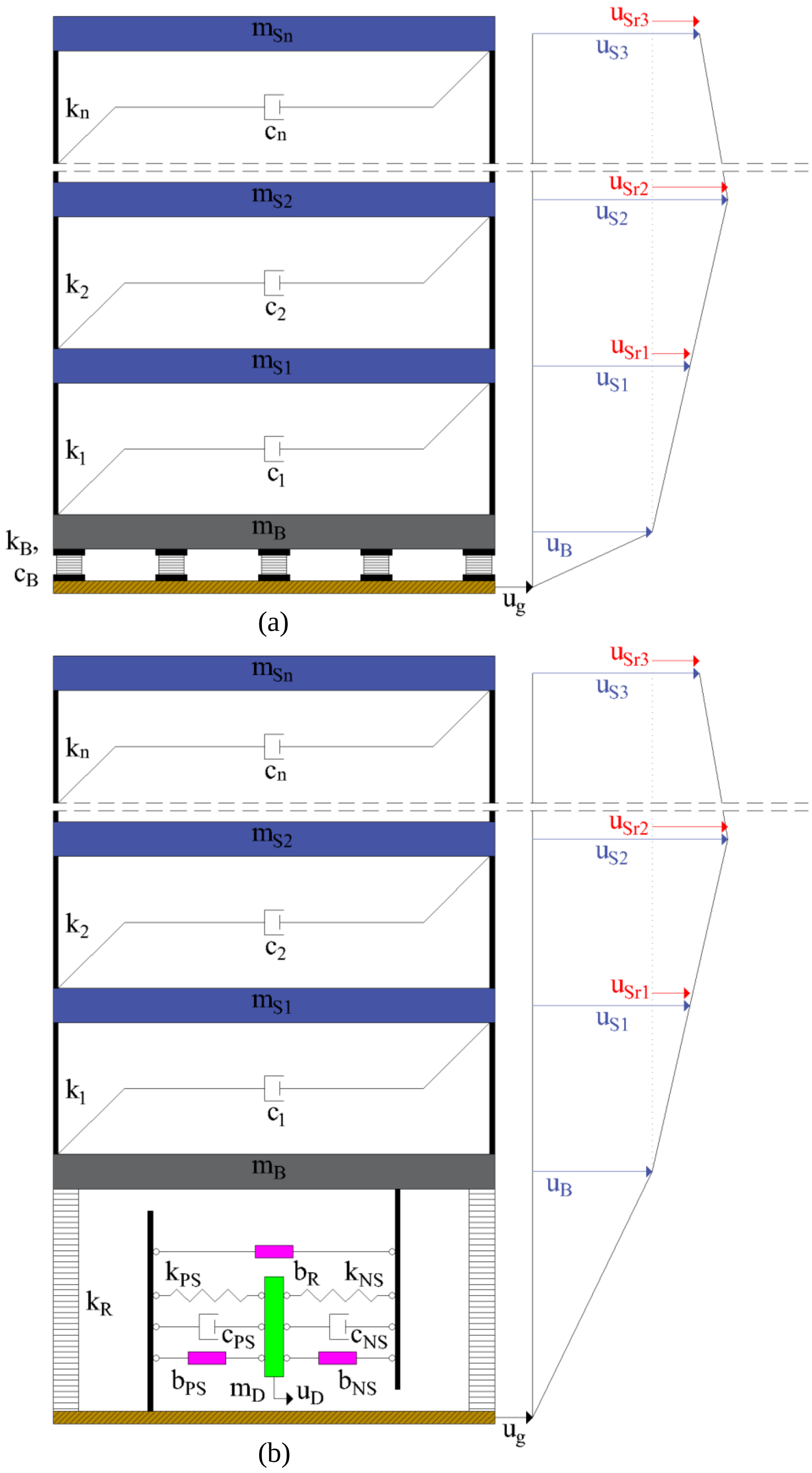

Figure 5.2: Multistory building with the proposed absorption base system, (a) sketch of the model mounted on a conventional or highly damped base isolation and (b) sketch of the model mounted on the extended seismic stiff absorption base configuration 3 (ESBA-3)

All the matrices of Equation (5.4) correspond to the matrix extension of Equations (5.2a) and (5.2b) for MDoF systems. From (Eq. 5.4), the index $r_{BI} = n + 1$ is the total degrees of freedom, of a planar superstructure of the aforementioned assumptions with n degrees of freedom, mounted on a conventional or highly damped base isolation. The terms $\boldsymbol{M}^{BI}$, $\boldsymbol{C}^{BI}$ and $\boldsymbol{K}^{BI}$ are the mass, damping and stiffness matrices of the total system, respectively, while the $\boldsymbol{M}_S$, the $\boldsymbol{C}_S$ and the $\boldsymbol{K}_S$ are the same matrices of the superstructure as if it is fixed on the ground, with nxn dimensions each. The vector $\boldsymbol{\tau}_S$ is the influence vector and according to (Chopra, 2011), it represents the displacements of the masses resulting from static application of a unit ground displacement. For the present case of the planar superstructure with its assumptions, the influence vector coincides with the unit vector $\mathbf{1} = [1\ 1\ ...\ 1]^T$, containing as many ones as the n degrees of freedom of the superstructure. The quantity $m_{S,tot} = \sum_{j=1}^{n} m_{Sj}$, is the total mass of the superstructure and is equal to the sum of the floor masses, n in total. The vector $\mathbf{0}$ with n dimension contains zero elements. From the above clarifications the relative to the ground, now, displacements of the superstructure can computed from:

$$\boldsymbol{u}_S(t) = \boldsymbol{u}_{Sr}(t) + u_B(t) \tag{5.5}$$

as the first term of the sum is the relative to the base displacement of the structure, while the second term is the relative to the ground base displacement.

The same exact logic, as in the case of the base isolation with respect to the equations (5.2), is followed for the ESBA-3 configuration that correspond to the matrix extension of equations (5.3). The matrices in this case, as formulated previously, in (Eq. 5.4) are the following:

$$\boldsymbol{M}^{ESBA-3}_{(r_{ESBA-3})x(r_{ESBA-3})} =$$

$$\begin{bmatrix} \boldsymbol{M}_{S,(n)x(n)} & \boldsymbol{M}_{S,(n)x(n)}\boldsymbol{\tau}_{S,(n)x(1)} & \mathbf{0}_{(n)x(1)} \\ \boldsymbol{\tau}^T_{S,(1)x(n)}\boldsymbol{M}_{S,(n)x(n)} & [m_{tot} + (b_R + b_{NS})m_{tot}] & -(b_{NS}m_{tot}) \\ \mathbf{0}_{(1)x(n)} & -(b_{NS}m_{tot}) & [m_D + (b_{NS} + b_{PS})m_{tot}] \end{bmatrix}$$

$$\boldsymbol{C}^{ESBA-3}_{(r_{ESBA-3})x(r_{ESBA-3})} = \begin{bmatrix} \boldsymbol{C}_{S,(n)x(n)} & \mathbf{0}_{(n)x(1)} & \mathbf{0}_{(n)x(1)} \\ \mathbf{0}_{(1)x(n)} & c_{NS} & -c_{NS} \\ \mathbf{0}_{(1)x(n)} & -c_{NS} & (c_{NS} + c_{PS}) \end{bmatrix}$$

$$\boldsymbol{K}^{ESBA-3}_{(r_{ESBA-3})x(r_{ESBA-3})} = \begin{bmatrix} \boldsymbol{K}_{S,(n)x(n)} & \mathbf{0}_{(n)x(1)} & \mathbf{0}_{(n)x(1)} \\ \mathbf{0}_{(1)x(n)} & (k_R + k_{NS}) & -k_{NS} \\ \mathbf{0}_{(1)x(n)} & -k_{NS} & (k_{PS} + k_{NS}) \end{bmatrix}$$

$$\boldsymbol{\tau}^{ESBA-3}_{(r_{ESBA-3})x(1)} = \begin{bmatrix} \boldsymbol{M}_{S,(n)x(n)}\boldsymbol{\tau}_{S,(n)x(1)} \\ m_B + m_{S,tot} \\ m_D \end{bmatrix}$$

$$\boldsymbol{u}^{ESBA-3}_{(r_{ESBA-3})x(1)}(t) = \begin{bmatrix} \boldsymbol{u}_{Sr,(n)x(1)}(t) \\ u_B(t) \\ u_D(t) \end{bmatrix} \tag{5.6}$$

All the matrices of Equation (5.6) correspond to the matrix extension of Equations (5.3a), (5.3b) and (5.3c) for MDoF systems. From (Eq. 5.6), the index $r_{ESBA-3} = n + 2$ is the total degrees of freedom, of a planar superstructure of the aforementioned assumptions with n degrees of freedom, mounted on the ESBA-3 configuration. The terms $\boldsymbol{M}^{ESBA-3}$, $\boldsymbol{C}^{ESBA-3}$ and $\boldsymbol{K}^{ESBA-3}$ are the mass, damping and stiffness matrices of the total system, respectively, while all the rest matrices, vectors and scalar quantities have been explained previously. The quantity $m_{tot} = m_{S,tot} + m_B = \sum_{j=1}^{n} m_{Sj} + m_B$, is the total mass of the superstructure and is equal to the sum of the floor masses and the mass of the base.

5.3 Numerical application: 3-story concrete building structure

5.3.1 Initial building structure

A planar 3-story concrete building with a typical symmetric plan is considered. From section (5.2), it is $n = 3$, regarding the matrix equations. The 3-story concrete building is considered to have a concentrated on the floor level mass of 80 Mgr per story (so, $m_{S,tot} = 3 * 80 = 240$ Mgr) and the concrete of the columns is taken to belong into the category of C20/25 MPa. From (EN 1992-1-1, 2004), C20/25 concrete has a secant modulus of elasticity of 29.96 GPa (defined from the following relation: $E_{cm} = 22\left[\frac{f_{cm}}{10}\right]^{0.3}$, where $f_{cm} = f_{ck} + 8$, in MPa and $f_{ck} = 20\,MPa$ for C20/25). From the (Fig. 5.3) below, a typical floor may include 16 columns per story and each column has a height of 4.0 m and a square cross section with a 0.4 m side. The effective stiffness of each column can be calculated from the relation: $k_{stc,eff} = \frac{0.5*12E_{cm}I_{sec}}{h^3}$, where $I_{sec} = \frac{b_{sq}^4}{12}$ the square section's with side b_{sq} moment of inertia, h the column's height and the term 0.5 is considered by adopting the recommendations of (EN 1998-1, 2004) for cracked concrete sections of the columns. From all these as data, the mass and stiffness matrix which will be used in equations (5.4) or (5.6) are the following:

$$M_{S,(3)x(3)} = 80\begin{bmatrix} 1 & 0 & 0 \\ 0 & 1 & 0 \\ 0 & 0 & 1 \end{bmatrix} \text{ (in Mgr)} \tag{5.7a}$$

$$K_{S,(3)x(3)} = 16 \cdot k_{stc,eff}\begin{bmatrix} 2 & -1 & 0 \\ -1 & 2 & -1 \\ 0 & -1 & 1 \end{bmatrix} \text{ (in kN/m)} \tag{5.7b}$$

By performing a classical model analysis, the 3-story concrete building, with those characteristics, the following vector, containing the natural periods, results: $T_{Si} = [0.408\ 0.146\ 0.101]$ (in sec). Finally, the damping matrix is indirectly defined by using the Rayleigh damping (Katsikadelis, 2020):

$$C_{S,(3)x(3)} = a_0 M_{S,(3)x(3)} + a_1 K_{S,(3)x(3)} \text{ (in kNs/m)} \tag{5.7c}$$

where a_0 and a_1 are coefficients that construct a proportional damping matrix to the mass and stiffness matrices. They are defined as:

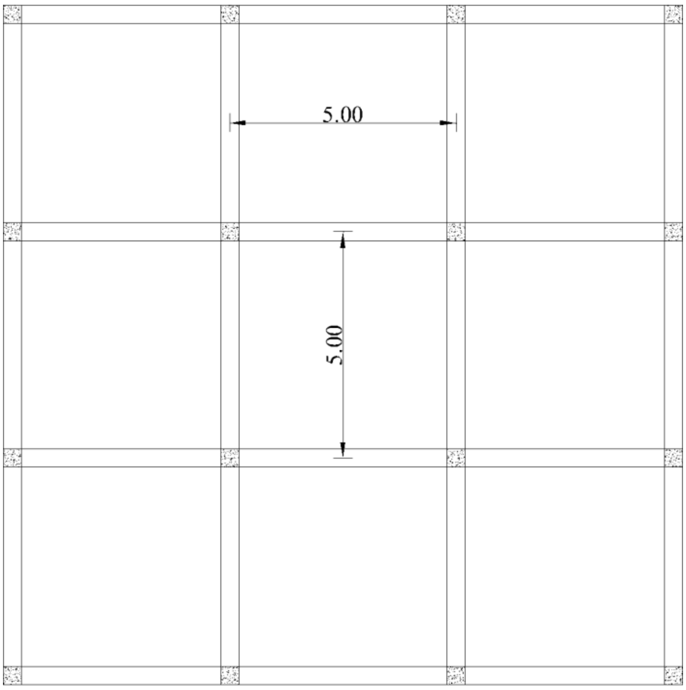

Figure 5.3: Ground floor plan of a typical floor of the structure (dimensions in m)

$$a_0 = \frac{2\xi\omega_n\omega_m}{\omega_n+\omega_m} \tag{5.7d}$$

$$a_1 = \frac{2\xi}{\omega_n+\omega_m} \tag{5.7e}$$

A reasonable assumption is made for the damping ratio ξ, that it is fixed for all the modes and is taken equal to 0.03, a typical value for a concrete building. The terms ω_n and ω_m can be the natural frequencies resulting from the first two eigenmodes.

5.3.2 Numerical results

The dynamic responses of the 3-story concrete building, firstly considered as fixed on the ground (noted as IN-from initial) and secondly mounted on the ESBA-3 configuration, the conventional (BI) and highly damped (HDBI) base isolation, are presented. For the ESBA-3 system the values of the parameters that correspond to the acceleration filter of 50% are selected again (values from Table 4.4), with a 1% of the total mass (including the mass of the base) corresponding to the mass of the oscillating mass. The mass of the base is selected to be 60 Mgr, so that the total mass of the 3 stories with the mass of the base, be equal to the total mass with which the optimization processes were performed. The same base mass is selected, also, for the conventional and highly damped base isolation cases. The stiffness and damping parameters of the base isolation emerge by considering the same frequency of the system, as in the case of ESBA-3, in order to have similar comparisons. So, in analogy with equations (4.30) and (4.31) the stiffness and damping of the base isolation are calculated as:

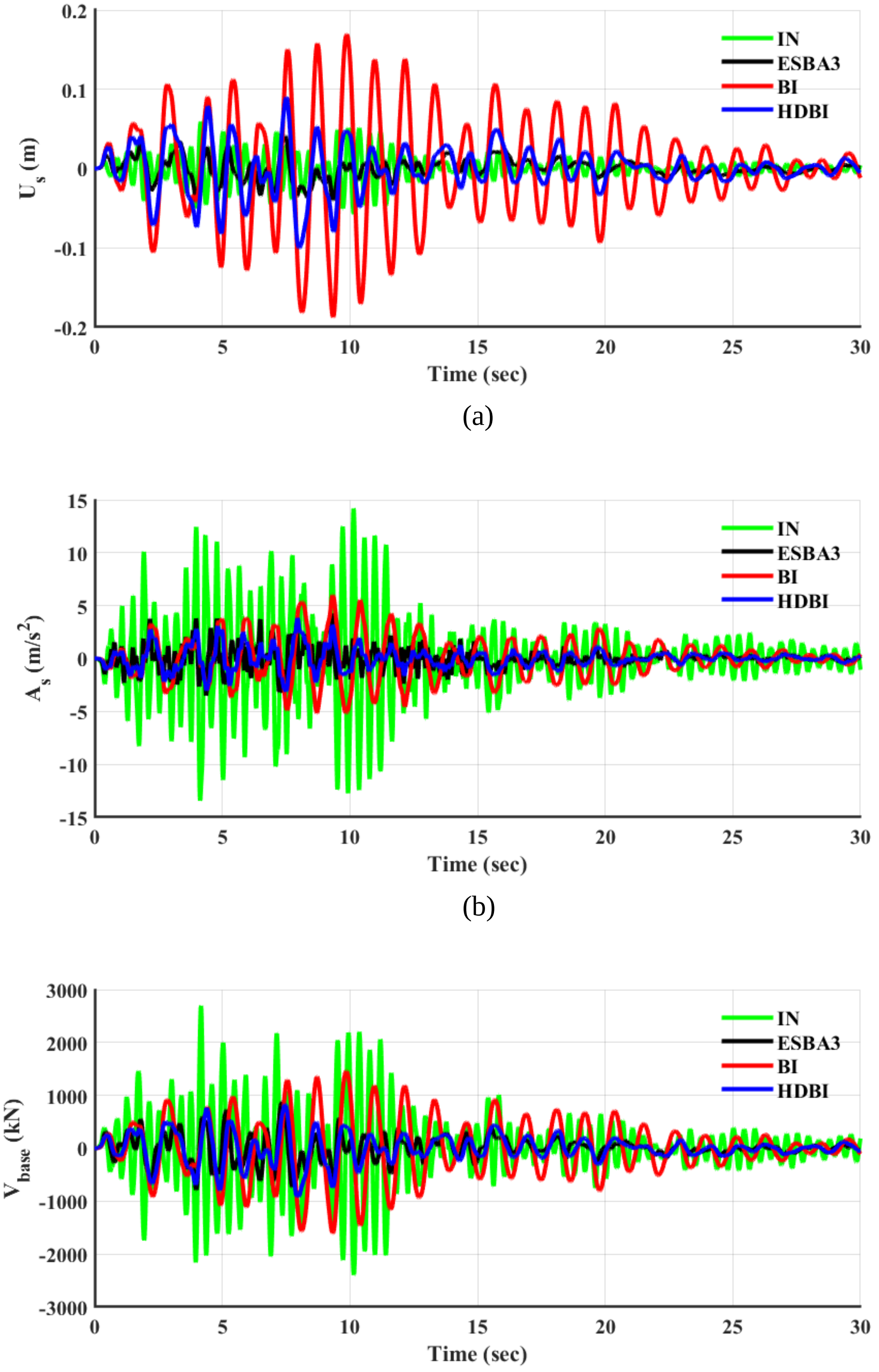

(a)

(b)

(c)

Figure 5.4: Comparative results, in terms of structure's (a) top floor relative to the ground displacement, (b) top floor absolute acceleration and (c) base shear between the fixed structure (IN), the conventional (BI) and highly damped (HDBI) base isolation and the ESBA-3 configuration (ESBA3), for an artificial acceleration

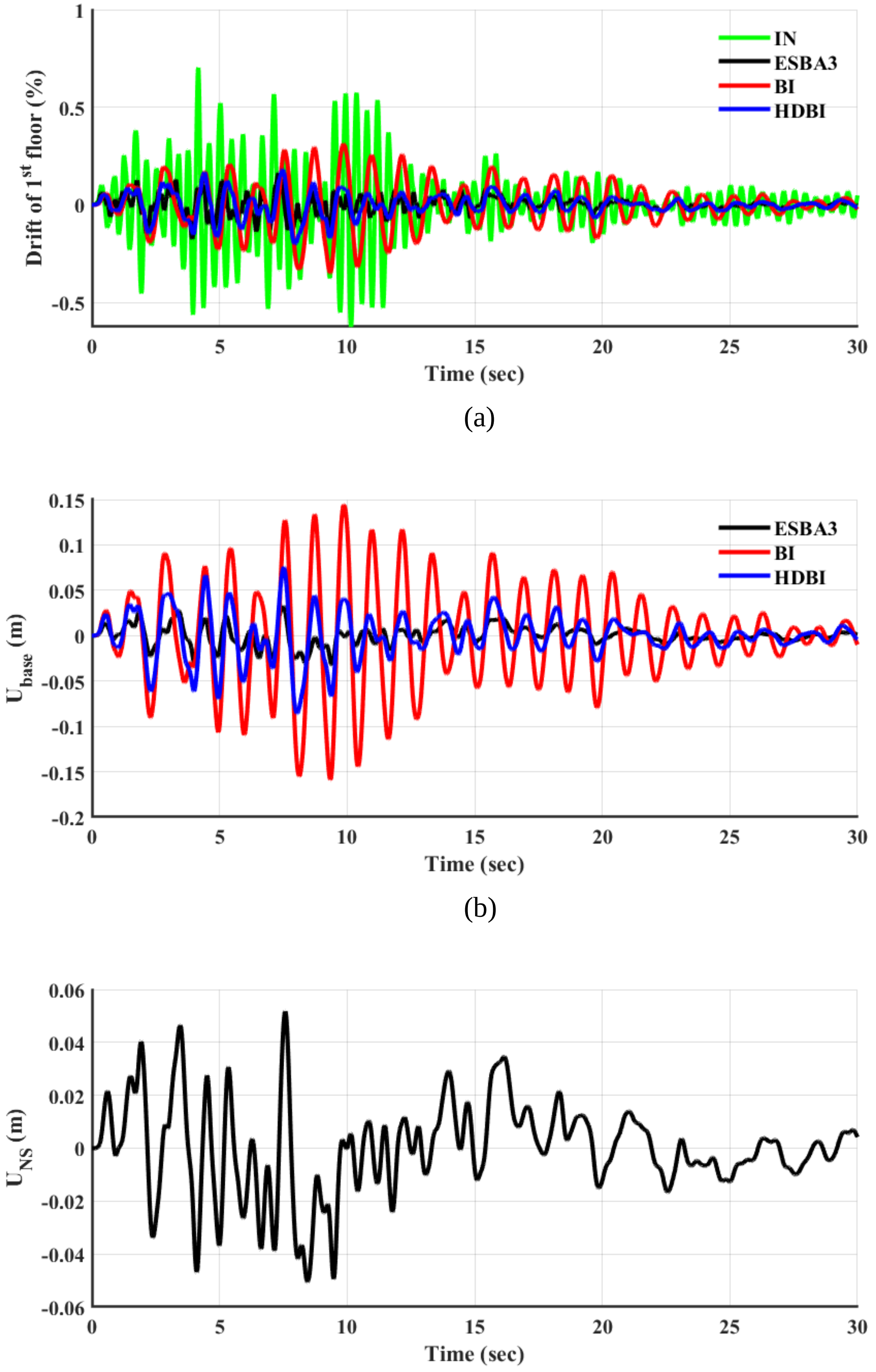

(a)

(b)

(c)

Figure 5.5: Comparative results, in terms of structure's (a) first floor drift, (b) base relative to the ground displacement and (c) NS stroke between the fixed structure (IN), the conventional (BI) and highly damped (HDBI) base isolation and the ESBA-3 configuration (ESBA3), for an artificial acceleration

$$k_{BI\ or\ HDBI} = m_{tot}\left(2\pi f_0^{ESBA-3\ for\ 50\%\ acceleration\ filter}\right)^2 \tag{5.8a}$$

$$c_{BI\ or\ HDBI} = 2m_{tot}\left(2\pi f_0^{ESBA-3\ for\ 50\%\ acceleration\ filter}\right)\zeta_{BI\ or\ HDBI} \tag{5.8b}$$

where $\zeta = 0.05$ for the BI case and $\zeta = 0.20$ for the HDBI case.

By implementing all these, (Fig. 5.4(a)), presents the relative to the ground displacement of the top floor of the fixed structure (IN) and for the ESBA-3 configuration (ESBA3), the conventional (BI) and highly damped (HDBI) base isolation, according to (Eq. 5.5). Due to the same artificial accelerogram of the optimization processes, the fixed structure developed a relative displacement of 0.059 m on the top floor. ESBA-3 noted a 0.041 m while the BI and HDBI cases a relative displacement of 0.188 m and 0.1 m, respectively. That means, the ESBA-3 configuration manages to reduce the top relative displacement to 30.51% of the fixed structure. Opposite to that, the BI increases the displacement by 218.64% of the initial and the HDBI by 69.49% of the initial. It is clearly observed that the ESBA-3 configuration develops a relative small value of the displacement, including the displacement of the base and the relative to the base displacement of the top floor.

The figure 5.4(b), displays the absolute acceleration of the top floor for the same four cases. The initial structure reached the value of 14.18 m/s^2, while with the aid of ESBA-3 configuration, this value becomes 4.25 m/s^2. This response is reduced by 70.03%. The same response is at 6.00 m/s^2 and 3.83 m/s^2 for the BI and HDBI cases, respectively, which correspond to a reduction of 57.69% and 72.99% of the initial. Again, the ESBA-3 notes a very satisfying performance as its response is located between that of the BI and HDBI systems.

The next figure (Fig. 5.4(c)), shows the shear base of the four cases. The artificial acceleration creates a shear base of 2694.5 kN to the fixed structure (this is calculated as the equivalent elastic forced of the base, which is equal to $16 \cdot k_{stc,eff} u_S^{1^{st}\ floor}(t)$). ESBA-3 configuration reached the value of 876.6 kN, while the BI and the HDBI yielded a base shear of 1606.8 kN and 913 kN, respectively. The base shear from the vibration absorption bases is reduced by 67.47%, 40.37% and 66.12% for all the systems with respect to the initial fixed structure. Again, the ESBA-3 achieves the best dynamic performance in this case.

The figure (5.5(a)) depicts the drift of the first floor. It is calculated as the % of the column's height and for the absorption bases is directly calculated from the equations (5.4) and (5.6), as the first floor is expressed from the relative to the base displacement. The drift of the fixed structure is 0.70%. The same response of the ESBA-3 system reaches the value of 0.18%, while the BI and HDBI have a drift of 0.35% and 0.20%, respectively. Again, the ESBA achieves the highest reduction of the initial structure by 74.29%. The conventional base notes a reduction of 50% and the highly damped base isolation decreases the drift by 71.43%.

The next figure (5.5(b)), includes the curves that refer to the relative to the ground displacement of the base, on which the structure is mounted, of all the vibration absorption base systems. As it can be clearly observed, the ESBA-3 configuration achieved the relatively small value of 0.033m, while the other two base isolations note a base displacement of 0.159 m (BI) and 0.086 m (HDBI). The biggest advantage of the proposed system is that it can reach a base displacement reduced by 79.25%, compared to the conventional base isolation and by 61.63% compared to the HDBI case.

Finally, (Fig. 5.5(c)) exhibits the time history of the NS stroke of the ESBA configuration. The maximum value of 0.052 m is reached, so as to note all the above performance issues.

The figures (5.6(a)-(c)) and (5.7(a)-(c)) depict the same exactly dynamic responses of the fixed structure and all the vibration absorption base systems, subjected to the Tabas Near Fault real earthquake. It has the highest PGA (0.854g) according to Table 4.5. Again, as it can be clearly noticed, the ESBA-3 configuration manages to outperform the other two base isolation systems, in terms of the structure's relative to the ground displacement, base shear and first floor drift and the base displacement. As far as the structure's absolute acceleration of the last floor, the ESBA-3 exhibits a maximum value, almost equal to that of the BI and slightly larger than that of the HDBI. More specifically, the fixed structure has a maximum relative displacement of 0.1 m, absolute acceleration of 30.29 m/s^2, base shear of 4313.1 kN and first floor drift 1.12%, while the ESBA-3 system presented the values of the same responses of: 0.088 m (12% reduced), 11.43 m/s^2 (62.26% reduced), 1428.1 kN (66.89% reduced) and 0.31% drift (72.32% reduced) and has a base displacement of 0.067 m (67% reduced compared to the 0.203 m of BI and 52.48% reduced with respect to the 0.141 m of the HDBI). Finally, a reasonable value of 0.119 m of NS stroke is yielded by the ESBA-3.

In (Fig. 5.8(a)), there are the maximum values of the fixed structure, the BI, the HDBI and the ESBA-3 configurations, subjected to all the real earthquakes. In more than half of the real earthquakes, the ESBA-3 system presents the lowest relative to the ground displacements compared to the fixed structure, the BI and HDBI. In all the earthquakes it is lowest than that of the base isolation systems. The maximum response is produced by the earthquake No 7, where the BI exhibits a displacement of 0.244 m, the HDBI 0.139 m and the ESBA 0.049 m, all larger than that of 0.045 m of the fixed structure.

In the next figure of (5.8(b)), the absolute acceleration of the top floor is depicted for all the four cases. In a little less than half of the real earthquakes, the ESBA-3 yields the lowest responses of the absolute acceleration, which is a very satisfying performance as, in the previous plots of the random acceleration and the Tabas NF, was not the lowest. The largest values emerge from earthquake No 11 (Tabas NF), which was analyzed earlier. The ESBA-3 has the same response of the BI system and is slightly larger than the value of 10.07 m/s^2 of the HDBI.

The figure (5.8(c)) includes the bars of the maximum values of the base shear from all the real earthquakes for all the cases. Again, as in the case of the absolute acceleration, in a little less than half of the earthquakes the ESBA-3 exhibits the lowest values. The most extreme values appear again in the Tabas NF earthquake (No 11). The ESBA-3 has the lowest value of 1428.1 kN compared to the base shears of the BI and the HDBI, which are 2051.4 kN and 1540 kN, respectively.

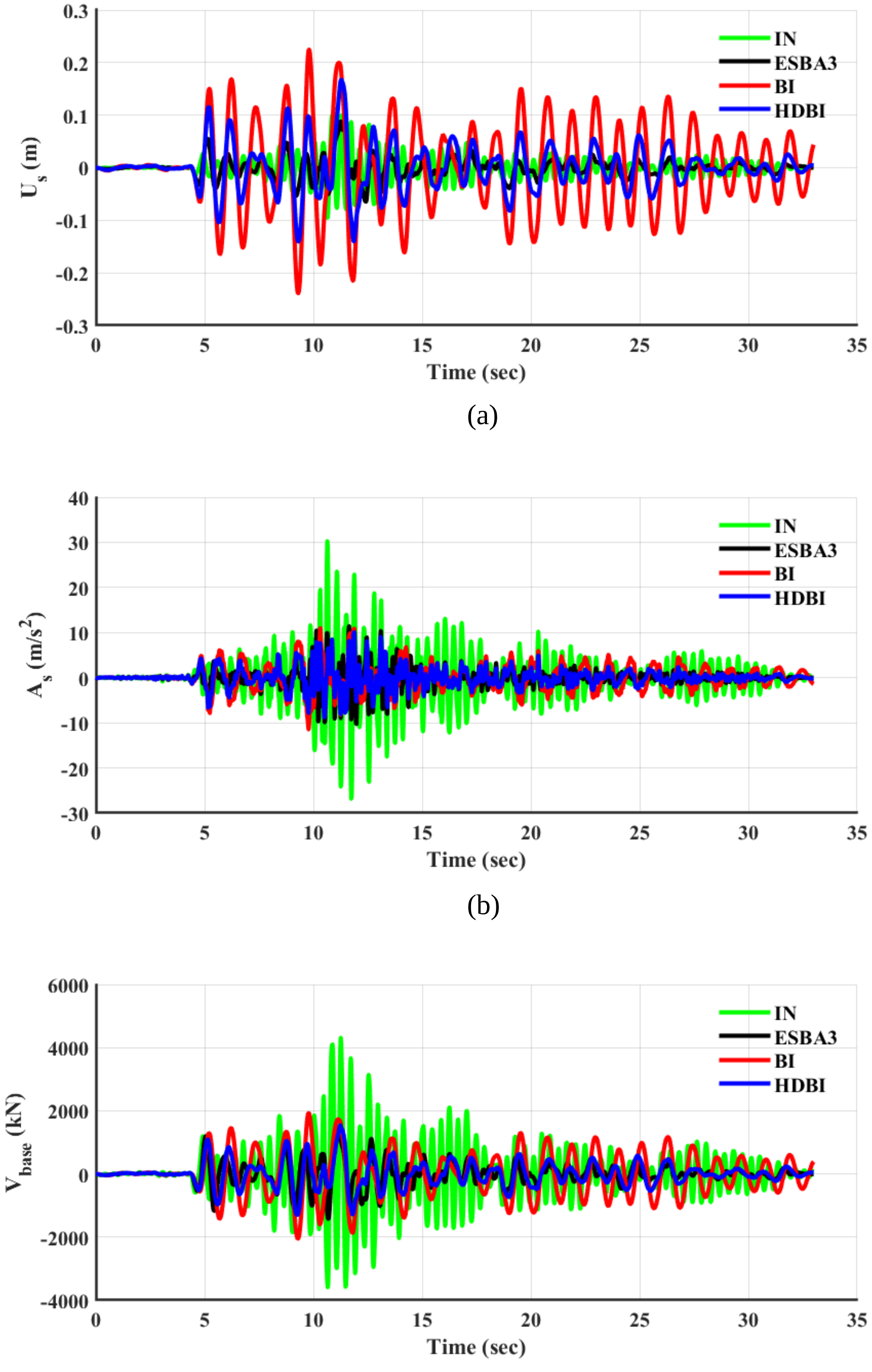

(a)

(b)

(c)

Figure 5.6: Comparative results, in terms of structure's (a) top floor relative to the ground displacement, (b) top floor absolute acceleration and (c) base shear between the fixed structure (IN), the conventional (BI) and highly damped (HDBI) base isolation and the ESBA-3 configuration (ESBA3), for the Tabas Near Fault earthquake

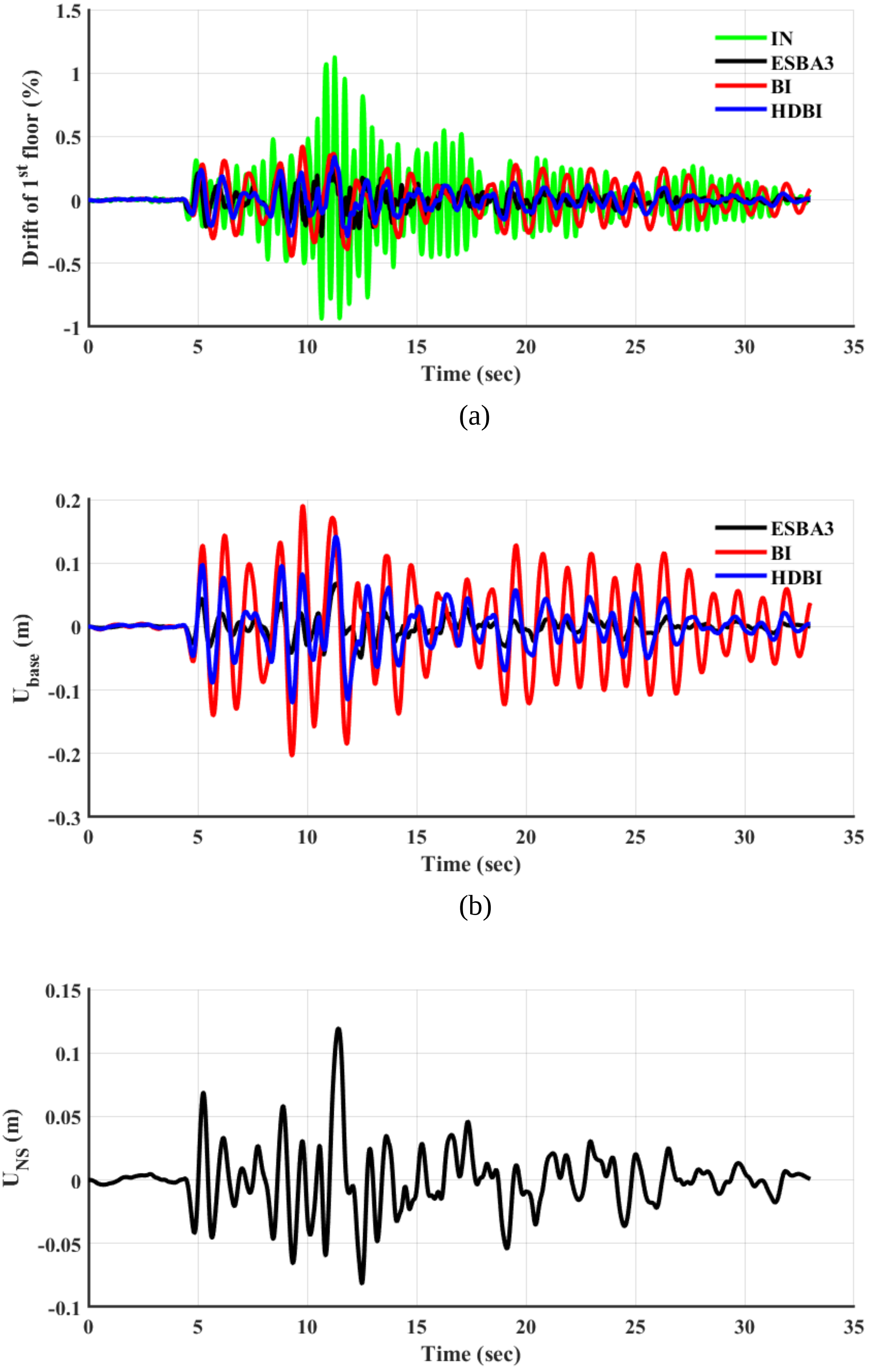

(a)

(b)

(c)

Figure 5.7: Comparative results, in terms of structure's (a) first floor drift, (b) base relative to the ground displacement and (c) NS stroke between the fixed structure (IN), the conventional (BI) and highly damped (HDBI) base isolation and the ESBA-3 configuration (ESBA3), for the Tabas Near Fault earthquake

In figure (5.9(a)), there are the drifts of the first floor for all the cases subjected to all the real earthquakes. Again, as in the previous cases of the absolute acceleration and base shear, in slightly less than half of the real earthquakes, the ESBA-3 configuration appears to have the lowest values of the drifts. In the rest earthquakes, the majority of them yield values that are slightly above the HDBI or between the BI and HDBI and in minor cases a bit larger than that of the base isolation systems. The largest response comes again from the Tabas NF earthquake, where ESBA-3 has a drift of 0.31% compared to that of 0.44% and 0.34% of the BI and HDBI, respectively.

In the next figure (5.9(b)), the curves, that depict the relative to the ground displacement of the base of all the three systems, are presented. The major advantage is that the ESBA-3 configuration exhibits the smallest values for this response in all the real earthquakes. The largest base displacement is due to the earthquake No7, where the BI reached the value of 0.207 m, the HDBI 0.118 m and the ESBA-3 0.039 m (which is reduced by 81.16% and 66.95% of the same responses of the BI and the HDBI, respectively).

Finally, in the figure (5.9(c)), there are the NS strokes of the ESBA-3, that are produced by the real earthquakes. The largest value is that from Tabas NF (No 11) earthquake, while in all the others the NS stroke does not exceed the approximate value of 0.07m, meaning that this configuration remains within constructional and engineering constraints and realizations.

The following figure (Fig. 5.10(a)-(e)) contains the mean maximum values of all the main dynamic responses of the relative to the ground displacement of the top floor, the absolute acceleration of the top floor, the base shear, the drift of the first floor, the relative to the ground displacement of the base and NS stroke for all the artificial, near fault and far fault earthquakes. In (Fig. 5.10(a)), the ESBA-3 has the lowest relative to the ground displacement of the systems (including the fixed structure) for all the earthquakes. It exhibits a mean displacement of 0.046 m for all the artificial accelerations, 0.034 m for all the real NF and 0.009 m for all the FF, while the BI has respectively for the same responses, 0.197 m, 0.127 m and 0.027 m. In (Fig. 5.10(b)), the ESBA-3 has a slightly larger performance of that of the HDBI, regarding the absolute acceleration of the top floor. More specifically, the mean values are 4.61 m/s^2, 4.96 m/s^2 and 1.2 m/s^2 for all the artificial, the NF and the FF earthquakes, while the same values for the fixed structure and the HDBI, respectively, are the following by earthquake category: 15.34 m/s^2, 3.89 m/s^2, 11.40 m/s^2, 4.64 m/s^2, 3.30 m/s^2 and 1.12 m/s^2. The next figure (5.10(c)) presents the base shear. Again, the ESBA-3 exhibits the same approximately behavior as the HDBI (in NF has a bit lower response). It yields a base shear of 997 kN, 693 kN and 211 kN, while the same responses of the fixed structure are 2775 kN, 1767 kN and 577 kN for all the artificial, NF and FF earthquakes, respectively. The ESBA-3 manages, again, to maintain the lowest values of all the systems in terms of the drift of the first floor (except the FF case where it has a minor increased performance compared to that of the HDBI) and the base displacement. The drift variates from 0.2% (for all the artificial accelerations) to 0.15% (for all the NF) and 0.04% (for all the FF). The displacement of the base of the ESBA-3 variated from

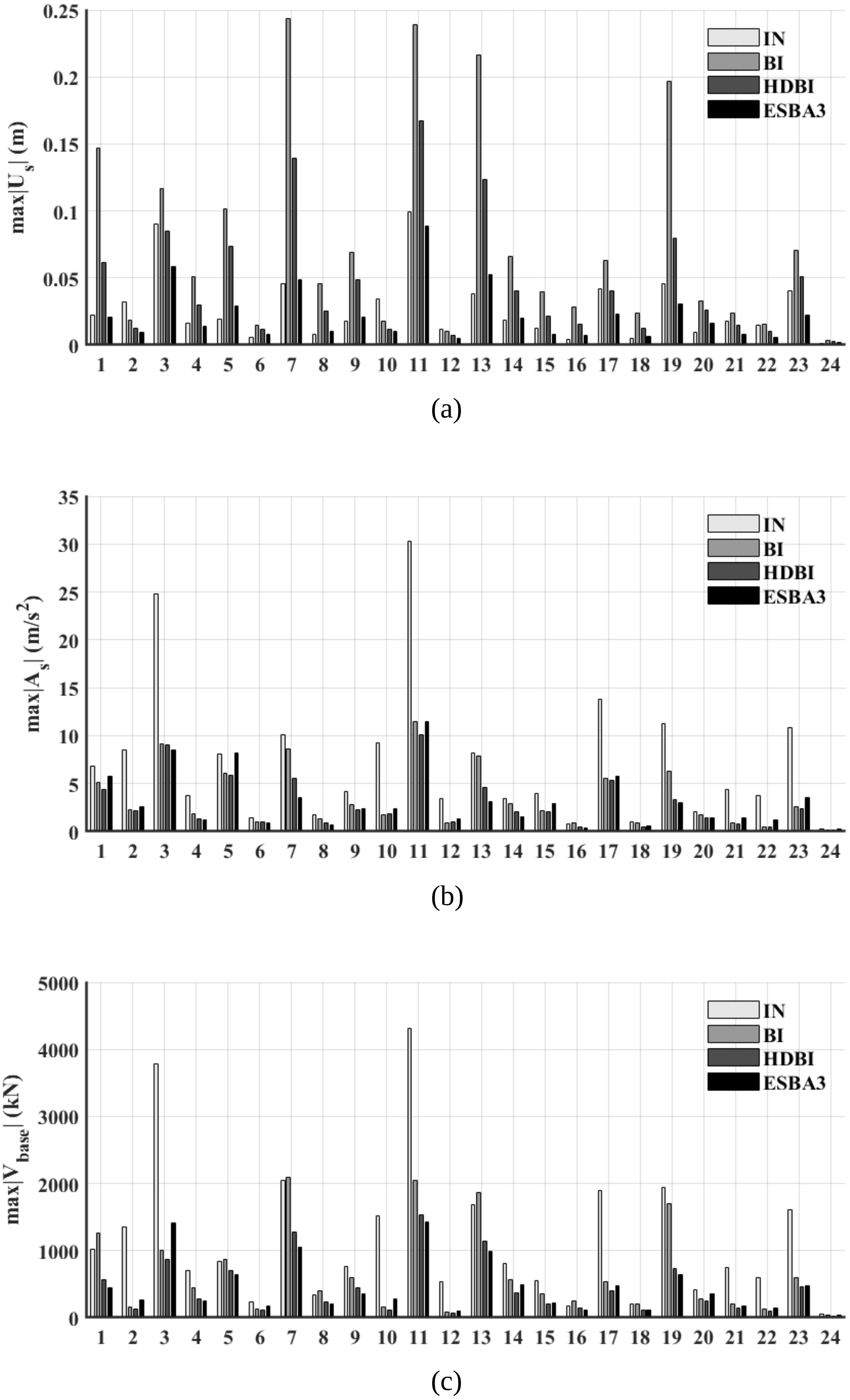

Figure 5.8: Main dynamic responses of (a) top floor relative to the ground displacement, (b) top floor absolute acceleration and (c) base shear between the fixed structure (IN), the conventional (BI) and highly damped (HDBI) base isolation and the ESBA-3 configuration (ESBA3), for all the near fault and far fault real earthquakes

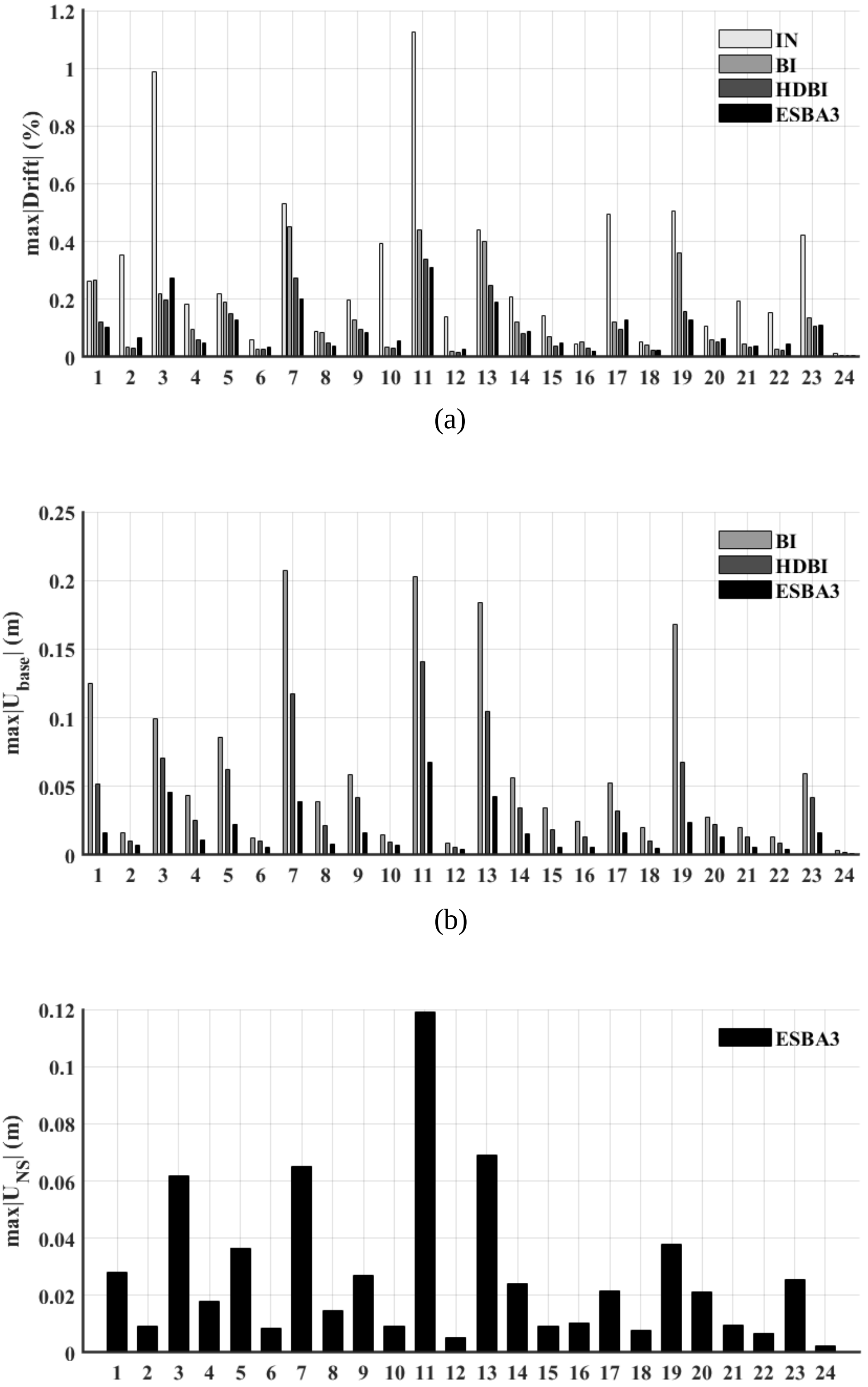

(a)

(b)

(c)

Figure 5.9: Main dynamic responses of (a) first floor drift, (b) relative to the ground base displacement and (c) NS stroke between the fixed structure (IN), the conventional (BI) and highly damped (HDBI) base isolation and the ESBA-3 configuration (ESBA3), for all the near fault and far fault real earthquakes

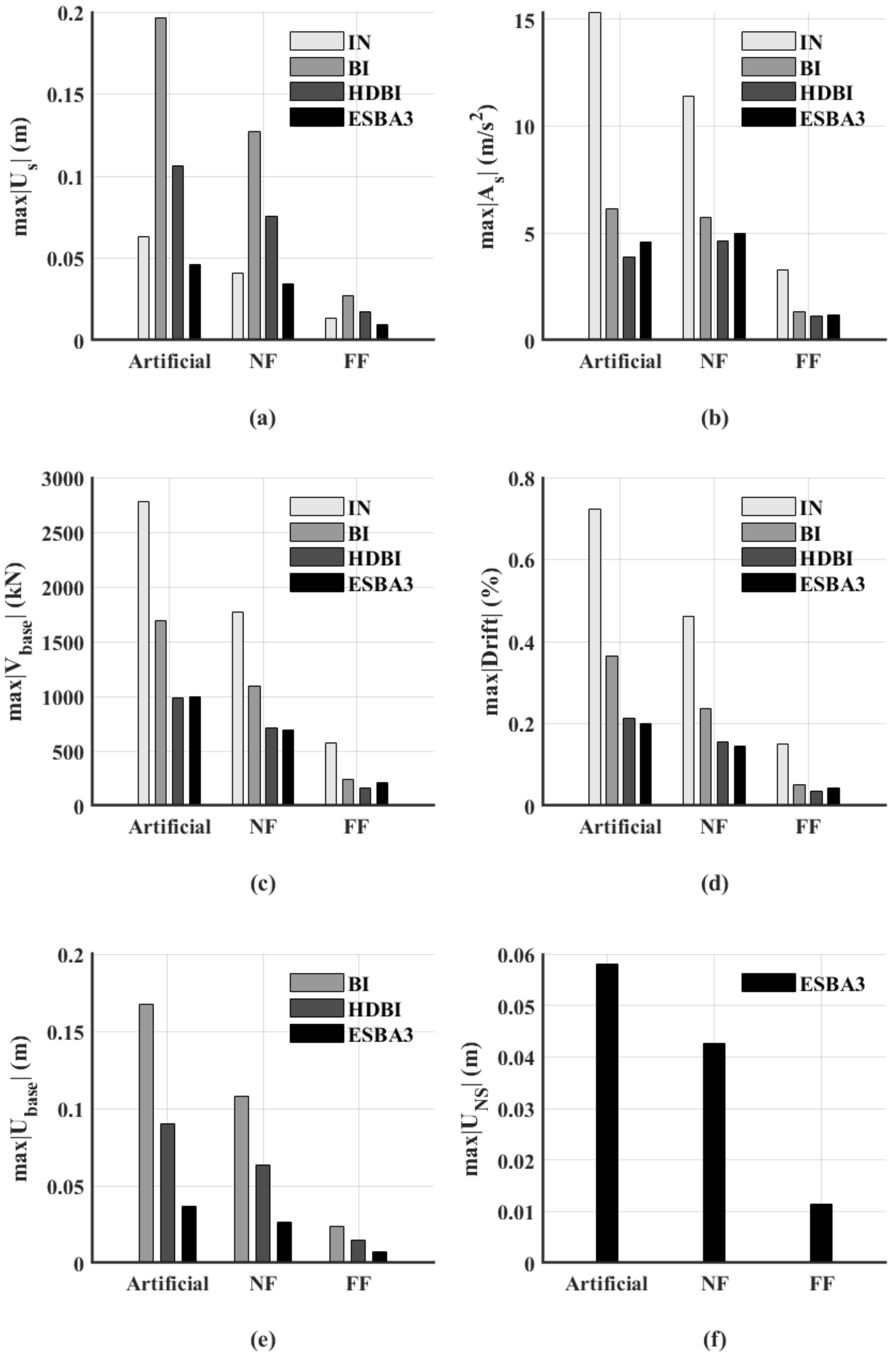

(a) (b)

(c) (d)

(e) (f)

Figure 5.10: Mean maximum values of dynamic responses of (a) top floor relative to the ground displacement, (b) top floor absolute acceleration, (c) base shear, (d) first floor drift, (e) relative to the ground base displacement and (f) NS stroke between the fixed structure (IN), the conventional (BI) and highly damped (HDBI) base isolation and the ESBA-3 configuration (ESBA3), for all the artificial accelerations and the near fault and far fault real earthquakes

0.037 m (all artificial earthquakes), to 0.027 m (all NF) and to 0.007 m (all FF). With the same earthquake category order, the BI and HDBI responses are 0.167 m, 0.108 m and 0.023 m and 0.09 m, 0.064 m and 0.014 m, respectively. Finally, in (Fig. 5.10(f)), it is noticed that the NS stroke is located within reasonable results, as it is 0.058 m for all the artificial, 0.043 m for all the NF and 0.011 m for all the FF.

For the analysis of the three-story building, only, a further investigation is conducted to compare the time history responses of the relative to the ground displacement of the top floor, the absolute acceleration of the top floor, the base shear, the drift of the first floor and the relative to the ground base displacement that correspond to the next figure below (Fig. 5.11 (a)-(e)) with the same order. As it can be clearly pointed, the decrease of the natural frequency of the conventional and highly damped base isolations (0.4 Hz now) leads to the increase of the relative to the ground displacement of the top floor and the base displacement, which becomes problematic from a certain point and beyond that. However, the rest of the responses decrease. The top displacement becomes now 0.274 m (BI) and 0.18 m (HDBI), which are 568.29% and 339.02%, respectively, higher than that of ESBA-3. Similar for the base isolation, BI and HDBI note the values of 0.265 m and 0.174 m for base displacement, which are higher by 703.03% and 427.27% by the ESBA-3. Quite small accelerations of 1.71 m/s^2 and 1.39 m/s^2, by the BI and HDBI respectively, are present, which are 59.76% and 67.29% lower than the response of the ESBa-3 configuration.

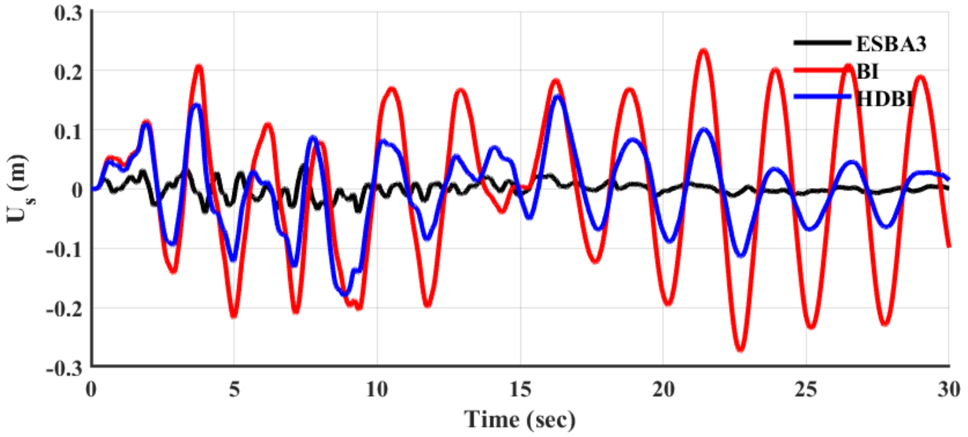

(a)

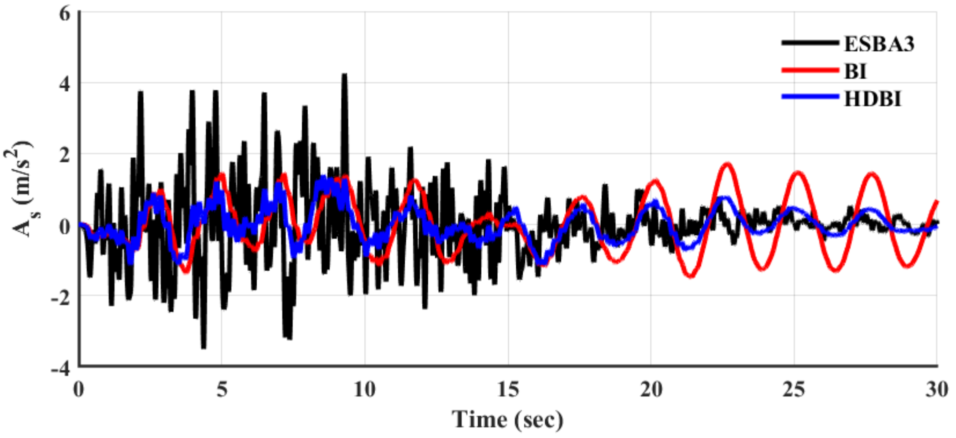

(b)

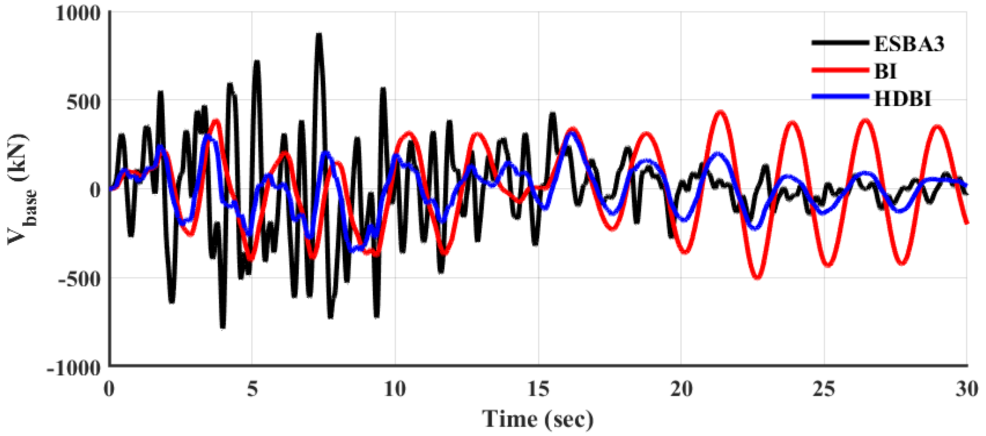

(c)

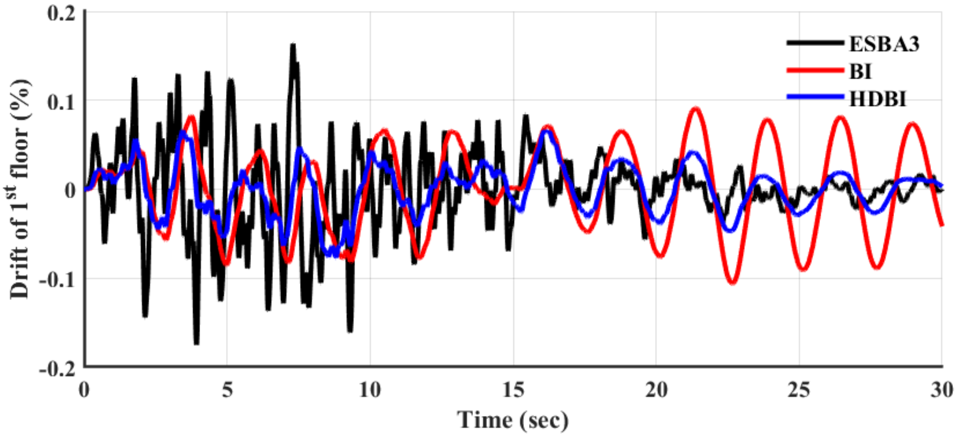

(d)

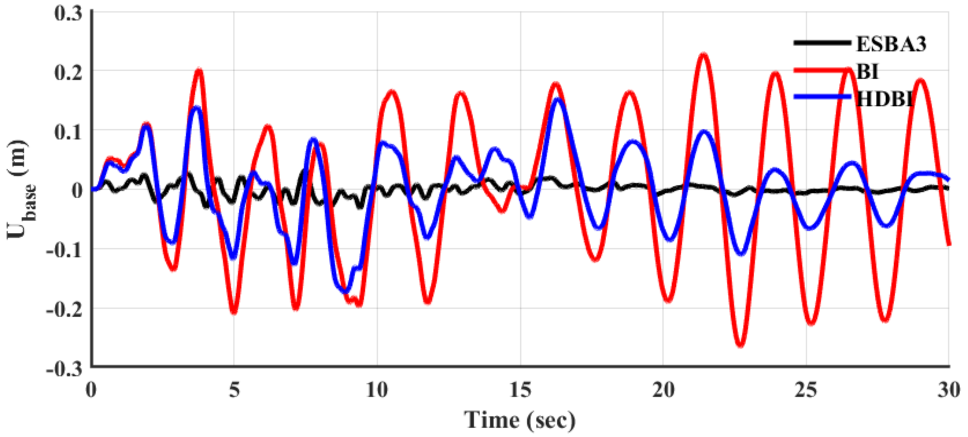

(e)

Figure 5.11: Comparative results, in terms of structure's (a) top floor relative to the ground displacement, (b) top floor absolute acceleration, (c) base shear, (d) first floor drift and (e) base relative to the ground displacement, between the ESBA-3 configuration (ESBA3) and the conventional (BI) and highly damped (HDBI) base isolation with natural frequency of 0.4 Hz of the base isolations, for the artificial acceleration

The base shear appears to be at 505 kN and 358 kN, approximately, for the BI and HDBI, lower by 42% and 59% approximately from the corresponding response of the ESBA-3 system. Finally, the drift of the first floor is achieved at 0.11% and 0.08% from the base isolation systems. These responses are decreased by 39% and 55.5% approximately from the drift yielded by the ESBA-3.

5.4 Numerical application: 5-story concrete building structure

5.4.1 Initial building structure

A planar 5-story concrete building with the same typical symmetric plan (Fig. 5.3), as of the 3-story building, is considered, now, in this section. From section (5.2), it is $n = 5$, regarding the matrix equations. This building is also considered to have the same concentrated mass on the floor of each story of 80 Mgr, (so, $m_{S,tot} = 5 * 80 = 400$ Mgr), the same concrete material, the same number of columns (since they share the same plan view) and the same column's height of 4m with the same cross section. From all these as data, the mass and stiffness matrix which will be used in equations (5.4) or (5.6) are the following:

$$M_{S,(5)x(5)} = 80\begin{bmatrix}1 & 0 & 0 & 0 & 0\\ 0 & 1 & 0 & 0 & 0\\ 0 & 0 & 1 & 0 & 0\\ 0 & 0 & 0 & 1 & 0\\ 0 & 0 & 0 & 0 & 1\end{bmatrix} \text{ (in Mgr)} \qquad (5.9a)$$

$$K_{S,(5)x(5)} = 16 \cdot k_{stc,eff}\begin{bmatrix}2 & -1 & 0 & 0 & 0\\ -1 & 2 & -1 & 0 & 0\\ 0 & -1 & 2 & -1 & 0\\ 0 & 0 & -1 & 2 & -1\\ 0 & 0 & 0 & -1 & 1\end{bmatrix} \text{ (in kN/m)} \qquad (5.9b)$$

By performing the classical model analysis, the 5-story concrete building, with those characteristics, the following vector, containing the natural periods, results: $T_{Si} = [0.638\ 0.219\ 0.139\ 0.108\ 0.095]$ (in sec). Finally, the damping matrix is indirectly defined by using again the Rayleigh damping (as in Eq. 5.7c):

$$C_{S,(5)x(5)} = a_0 M_{S,(5)x(5)} + a_1 K_{S,(5)x(5)} \text{ (in kNs/m)} \qquad (5.9c)$$

where a_0 and a_1 are the same coefficients that construct a proportional damping matrix to the mass and stiffness matrices and are defined by the same equations (5.7d) and (5.7e), by using the same value for ξ damping ratio of 0.03 and by considering the first two eigenmodes for computing the natural frequencies.

5.4.2 Numerical results

The dynamic responses of the 5-story concrete building, firstly considered as fixed on the ground (noted as IN-from initial) and secondly mounted on the ESBA-3 configuration, the conventional (BI) and highly damped (HDBI) base isolation, are presented. For the ESBA-3 system the values of the parameters that correspond to the acceleration filter of 50% are selected again (values from Table 4.4), with a 1% of the total mass (including the mass of the base, which is again selected to be the same mass of the 60 Mgr) corresponding to the mass of the oscillating mass. However, these values are modified analogically to the new total mass, in comparison to the 3-story building (Table 5.1). The frequency of the system is let to be unaltered, while the values of the negative stiffness element and that of the dampers that are parallel to the negative and positive stiffness elements are changed by 460/300, where 460(=5·80+60) Mgr is the total mass of the 5-story building with its base. The values of the inerters are identical to those of the 3-story case, as they express inertance by percentage of the total mass. Since the total mass has been modified, the inerter values refer now to it. The same base mass is selected, also, for the conventional and highly damped base isolation cases. The stiffness and damping parameters of the base isolation emerge by considering the same unchanged frequency of the system, as in the case of ESBA-3, in order to have similar comparisons. So, in analogy with equations (4.30) and (4.31) and by using the same equations of (5.8a) and (5.8b) with the new total mass, the stiffness and damping of the base isolation can be calculated.

Table 5.1: ESBA-3 configuration parameters for the response analysis of the 5-story building

f_0 (Hz)	k_{NS} (kN/m)	c_{NS} (kNs/m)	c_{PS} (kNs/m)	b_R (% ms)	b_{NS} (% ms)	b_{PS} (% ms)
0.9220	-16410.51	1288.79	1373.44	0.4993	0.2113	0.0001

By implementing all these, (Fig. 5.12(a)), presents the relative to the ground displacement of the top floor of the fixed structure (IN) and for the ESBA-3 configuration (ESBA3), the conventional (BI) and highly damped (HDBI) base isolation, according to (Eq. 5.5). Due to the same artificial accelerogram of the optimization processes, the fixed structure developed a relative displacement of 0.12 m on the top floor. ESBA-3 noted a 0.065 m while the BI and HDBI cases a relative displacement of 0.193 m and 0.118 m, respectively. That means, the ESBA-3 configuration manages to reduce the top relative displacement to 45.83% of the fixed structure. Opposite to that, the BI increases the displacement by 60.83% of the initial and the HDBI notes an approximate same response to that of the initial (reduced just by 1.67%). It is clearly observed that the ESBA-3 configuration develops a relative small value of the displacement, including the displacement of the base and the relative to the base displacement of the top floor.

The figure 5.12(b), displays the absolute acceleration of the top floor for the same four cases. The initial structure reached the value of 13.06 m/s^2, while with the aid of ESBA-3 configuration, this value becomes 5.37 m/s^2. This response is reduced by 58.88%. The same response is at 5.71 m/s^2 and 4.32 m/s^2 for the BI and HDBI cases, respectively, which correspond to a reduction of 56.28% and 66.92% of the initial. Again, the ESBA-3 notes a very satisfying performance as its response is located between that of the BI and HDBI systems.

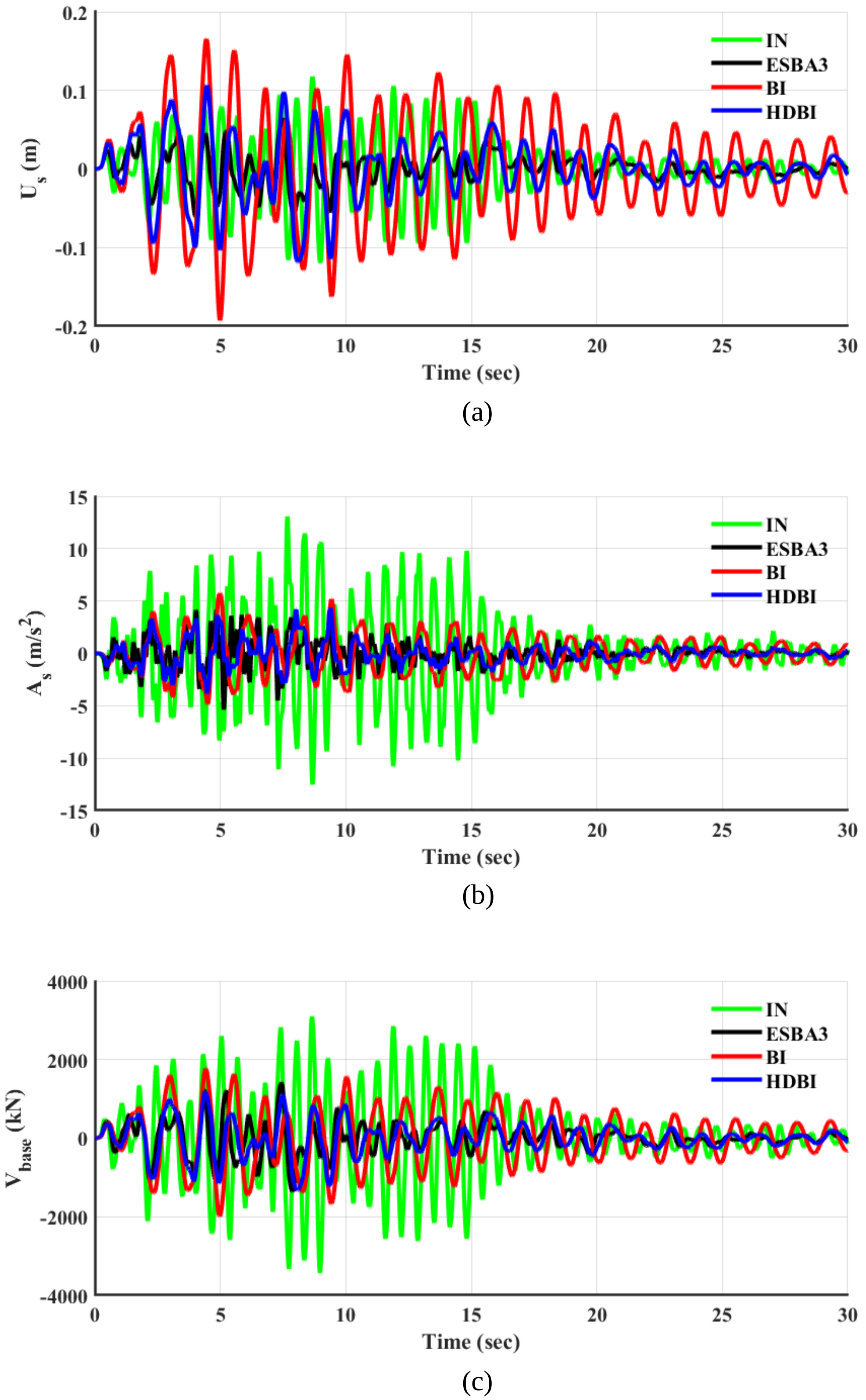

Figure 5.12: Comparative results for the 5-story building, in terms of structure's (a) top floor relative to the ground displacement, (b) top floor absolute acceleration and (c) base shear between the fixed structure (IN), the conventional (BI) and highly damped (HDBI) base isolation and the ESBA-3 configuration (ESBA3), for an artificial acceleration

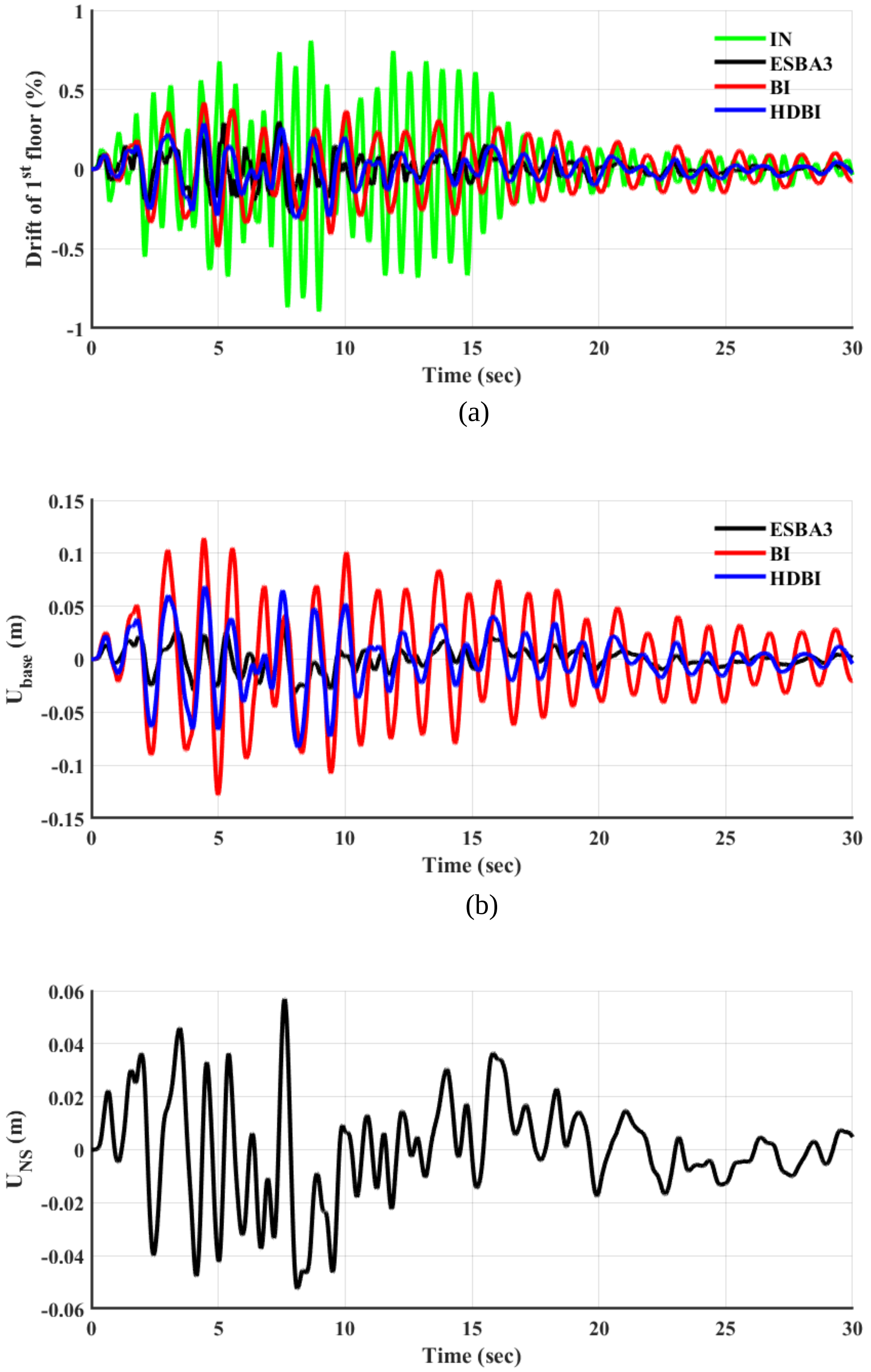

(a)

(b)

(c)

Figure 5.13: Comparative results for the 5-story building, in terms of structure's (a) first floor drift, (b) base relative to the ground displacement and (c) NS stroke between the fixed structure (IN), the conventional (BI) and highly damped (HDBI) base isolation and the ESBA-3 configuration (ESBA3), for an artificial acceleration

The next figure (Fig. 5.12(c)), shows the shear base of the four cases. The artificial acceleration creates a shear base of 3431.2 kN to the fixed structure (this is calculated as the equivalent elastic forced of the base, which is equal to $16 \cdot k_{stc,eff} u_S^{1^{st}\,floor}(t)$). ESBA-3 configuration reached the value of 1418 kN, while the BI and the HDBI yielded a base shear of 1987.9 kN and 1320.3 kN, respectively. The base shear from the vibration absorption bases is reduced by 58.67%, 42.06% and 61.52% for all the systems with respect to the initial fixed structure. Again, the ESBA-3 achieves a satisfying performance as its response is relatively close to that of the HDBI.

The figure (5.13(a)) depicts the drift of the first floor. It is calculated as the % of the column's height and for the absorption bases is directly calculated from the equations (5.4) and (5.6), as the first floor is expressed from the relative to the base displacement. The drift of the fixed structure is 0.89%. The same response of the ESBA-3 system reaches the value of 0.30%, while the BI and HDBI have a drift of 0.49% and 0.31%, respectively. Again, the ESBA achieves the highest reduction of the initial structure by 66.29%. The conventional base notes a reduction of 44.94% and the highly damped base isolation decreases the drift by 65.17%. As it emerged from the above, the ESBA-3 exhibits the best performance compared to the other two vibration absorption systems.

The next figure (5.13(b)), includes the curves that refer to the relative to the ground displacement of the base, on which the structure is mounted, of all the vibration absorption base systems. As it can be clearly observed, the ESBA-3 configuration achieved the relatively small value of 0.036m (a very close value to that of the 3-story building), while the other two base isolations note a base displacement of 0.128 m (BI) and 0.083 m (HDBI). The biggest advantage of the proposed system is that it can reach a base displacement reduced by 71.88%, compared to the conventional base isolation and by 56.63% compared to the HDBI case.

Finally, (Fig. 5.13(c)) exhibits the time history of the NS stroke of the ESBA configuration. The maximum value of 0.057 m is reached, so as to note all the above performance issues.

The figures (5.14(a)-(c)) and (5.15(a)-(c)) depict the same exactly dynamic responses of the fixed structure and all the vibration absorption base systems, subjected to the Tabas Near Fault real earthquake. It has the highest PGA (0.854g) according to Table 4.5. Again, as it can be clearly noticed, the ESBA-3 configuration manages to outperform the other two base isolation systems, in terms of the structure's relative to the ground displacement, base shear and first floor drift and the base displacement. As far as the structure's absolute acceleration of the last floor, the ESBA-3 exhibits a maximum value, slightly larger to that of the BI and a bit larger than that of the HDBI. More specifically, the fixed structure has a maximum relative displacement of 0.163 m, absolute acceleration of 20.55 m/s^2, base shear of 4848.2 kN and first floor drift 1.26%, while the ESBA-3 system presented the values of the same responses of: 0.132 m (19.02% reduced), 14.11 m/s^2 (31.34% reduced), 2441.4 kN (49.64% reduced) and 0.52% drift (58.73% reduced) and has a base displacement of 0.076 m (73.24% reduced compared to the 0.284 m of BI and 50.97% reduced with respect to the 0.155 m of the HDBI). Finally, a reasonable value of 0.136 m of NS stroke is yielded by the ESBA-3.

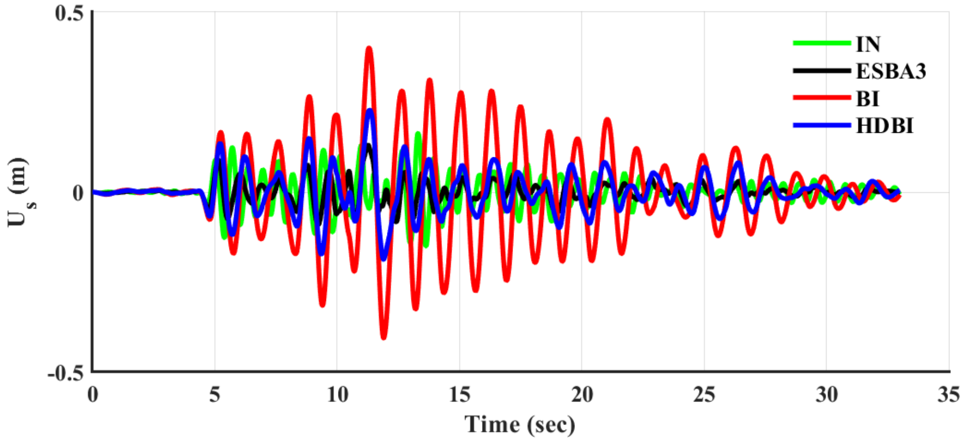

(a)

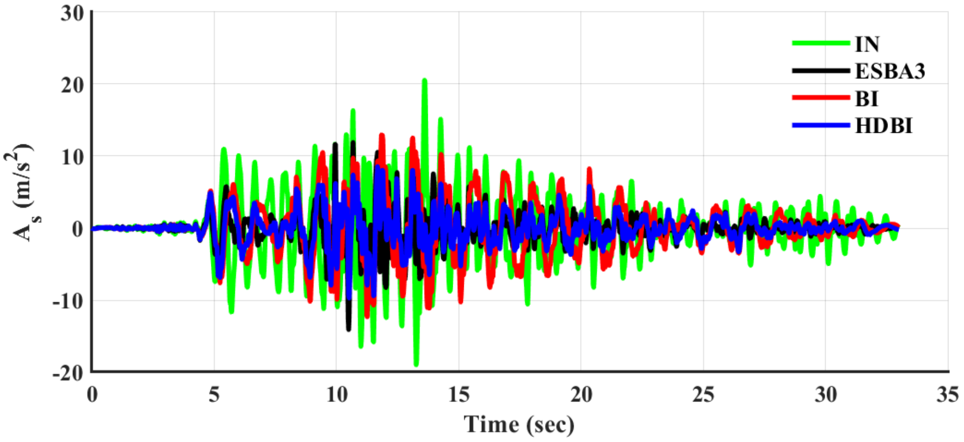

(b)

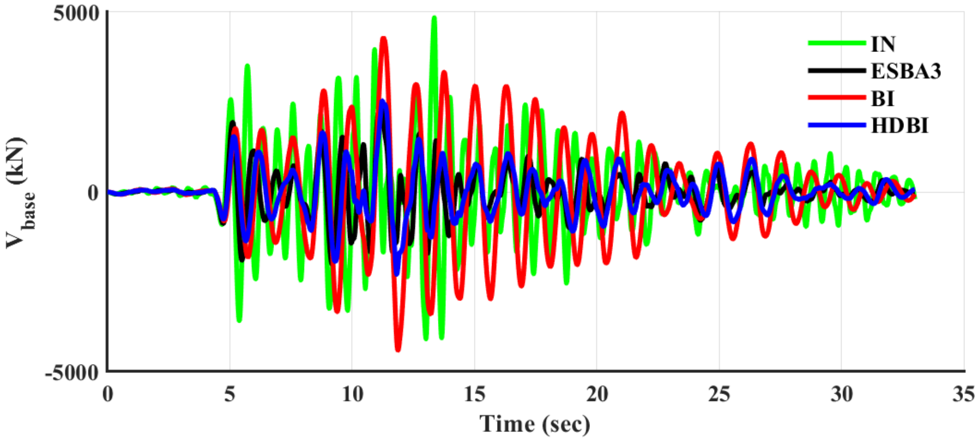

(c)

Figure 5.14: Comparative results for the 5-story building, in terms of structure's (a) top floor relative to the ground displacement, (b) top floor absolute acceleration and (c) base shear between the fixed structure (IN), the conventional (BI) and highly damped (HDBI) base isolation and the ESBA-3 configuration (ESBA3), for the Tabas Near Fault earthquake

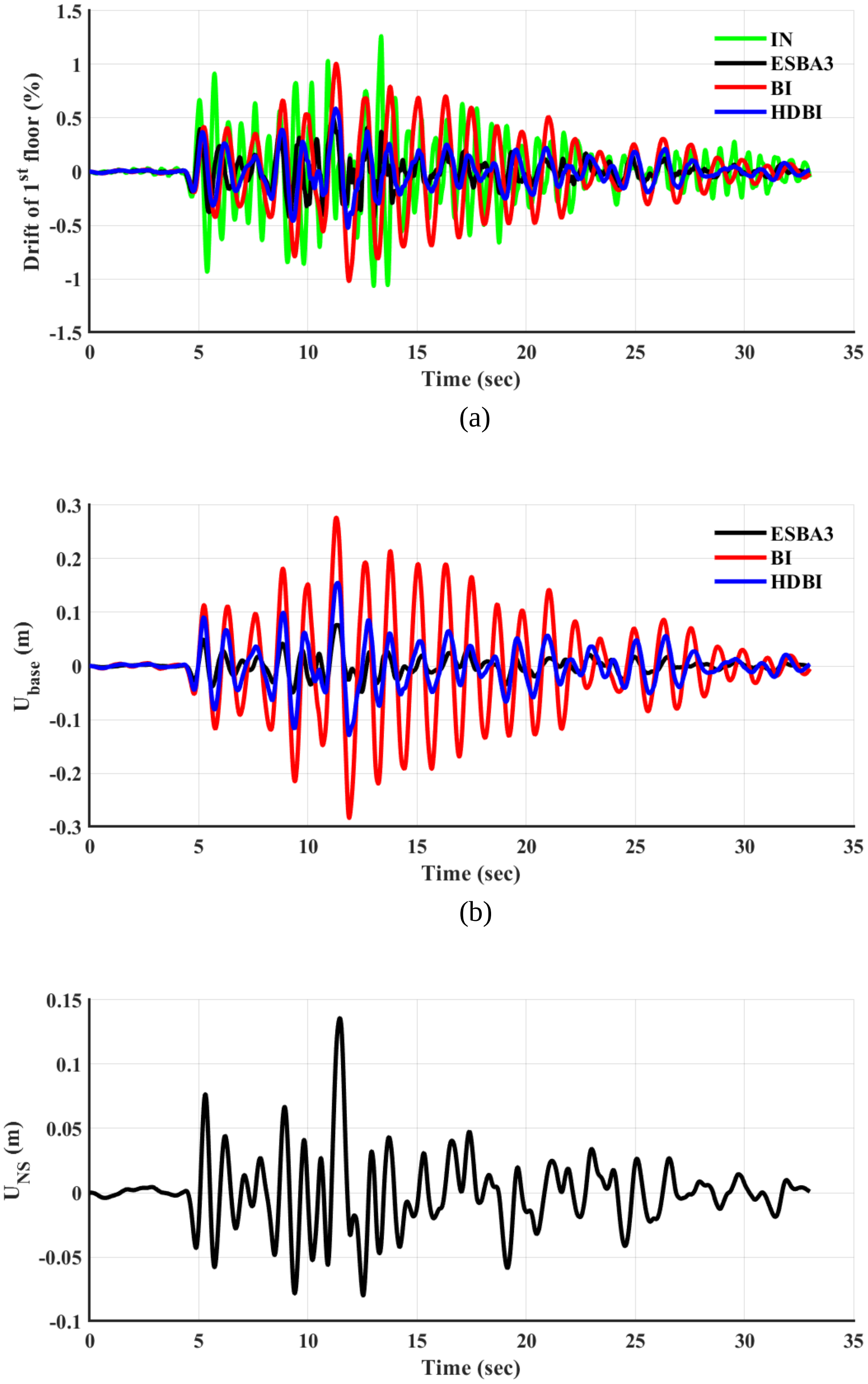

(a)

(b)

(c)

Figure 5.15: Comparative results for the 5-story building, in terms of structure's (a) first floor drift, (b) base relative to the ground displacement and (c) NS stroke between the fixed structure (IN), the conventional (BI) and highly damped (HDBI) base isolation and the ESBA-3 configuration (ESBA3), for the Tabas Near Fault earthquake

In (Fig. 5.16(a)), there are the maximum values of the fixed structure, the BI, the HDBI and the ESBA-3 configurations, subjected to all the real earthquakes. In the majority of the real earthquakes, the ESBA-3 system presents the lowest relative to the ground displacements compared to the fixed structure, the BI and HDBI. In all the earthquakes it is lowest than that of the base isolation systems. The maximum response is produced by the earthquake No 11, analyzed earlier, where the BI exhibits a displacement of 0.406 m, the HDBI 0.228 m and the ESBA 0.132 m. The ESBA-3 manages to exhibit the smallest displacement.

In the next figure of (5.16(b)), the absolute acceleration of the top floor is depicted for all the four cases. In a quarter of the real earthquakes, the ESBA-3 yields the lowest responses of the absolute acceleration, which is a satisfying performance as, in the previous plots of the random acceleration and the Tabas NF, was not the lowest. The largest values emerge from earthquake No 11 (Tabas NF), which was analyzed earlier. The ESBA-3 has a slightly larger response than that of the BI system and is a bit larger than the value of 9.74 m/s^2 of the HDBI.

The figure (5.16(c)) includes the bars of the maximum values of the base shear from all the real earthquakes for all the cases. In a little less than half of the earthquakes the ESBA-3 exhibits the lowest values. The most extreme values appear again in the Tabas NF earthquake (No 11). The ESBA-3 has the lowest value of 2441.4 kN compared to the base shears of the BI and the HDBI, which are 4408.1 kN and 2536.6 kN, respectively.

In figure (5.17(a)), there are the drifts of the first floor for all the cases subjected to all the real earthquakes. In slightly more than half of the real earthquakes, the ESBA-3 configuration appears to have the lowest values of the drifts. In the rest earthquakes, the half of them approximately, yield values that are between the BI and HDBI and in the other half cases a bit larger than that of the base isolation systems. The largest response comes again from the Tabas NF earthquake, where ESBA-3 has a drift of 0.52% compared to that of 1.02% and 0.59% of the BI and HDBI, respectively.

In the next figure (5.17(b)), the curves, that depict the relative to the ground displacement of the base of all the three systems, are presented. The major advantage is that the ESBA-3 configuration exhibits the smallest values for this response in all the real earthquakes. The largest base displacement is due to the earthquake No11, where the BI reached the value of 0.284 m, the HDBI 0.155 m and the ESBA-3 0.076 m (which is reduced by 73.24% and 50.97% of the same responses of the BI and the HDBI, respectively, as previously mentioned).

Finally, in the figure (5.17(c)), there are the NS strokes of the ESBA-3, that are produced by the real earthquakes. The largest value is that from Tabas NF (No 11) earthquake (0.136 m), while in all the others the NS stroke does not exceed the approximate value of 0.08m, meaning that this configuration remains within constructional and engineering constraints and realizations, especially for a 5-story building.

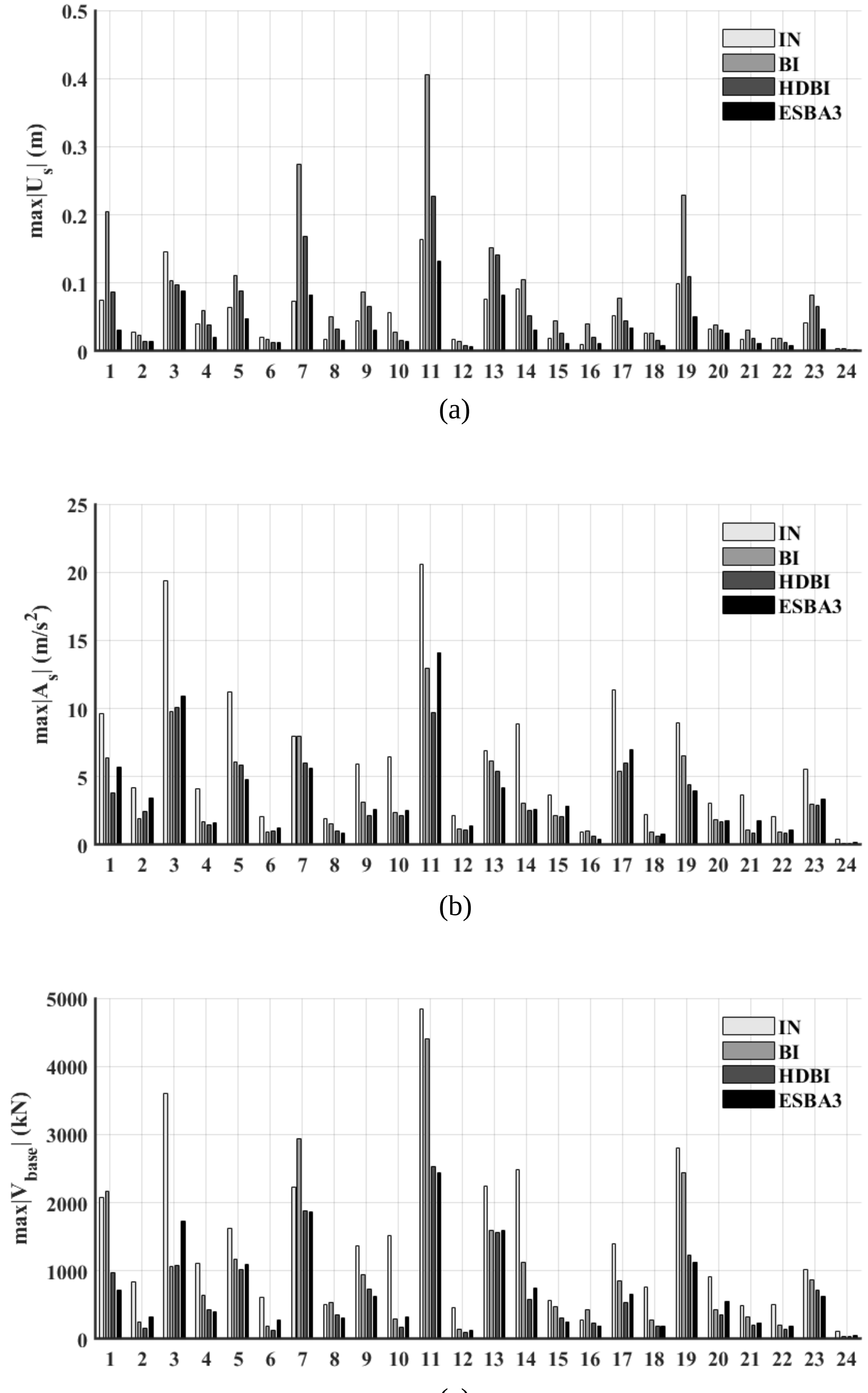

(a)

(b)

(c)

Figure 5.16: Main dynamic responses, for the 5-story building, of (a) top floor relative to the ground displacement, (b) top floor absolute acceleration and (c) base shear between the fixed structure (IN), the conventional (BI) and highly damped (HDBI) base isolation and the ESBA-3 configuration (ESBA3), for all the near fault and far fault real earthquakes

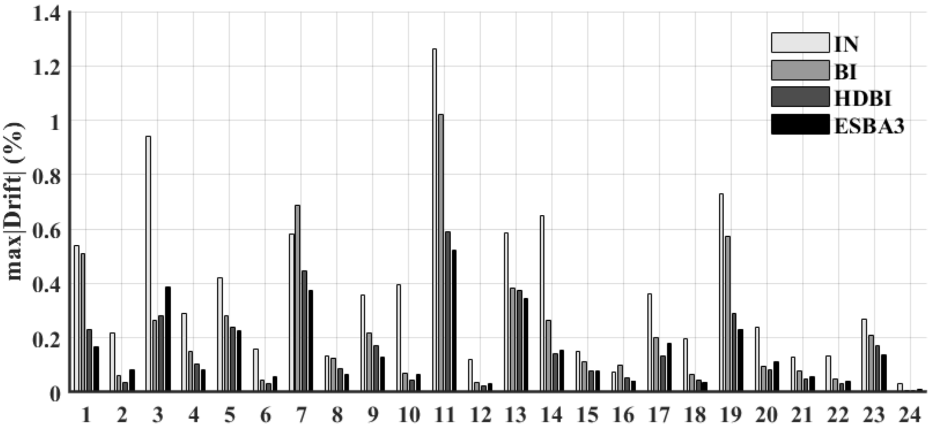

(a)

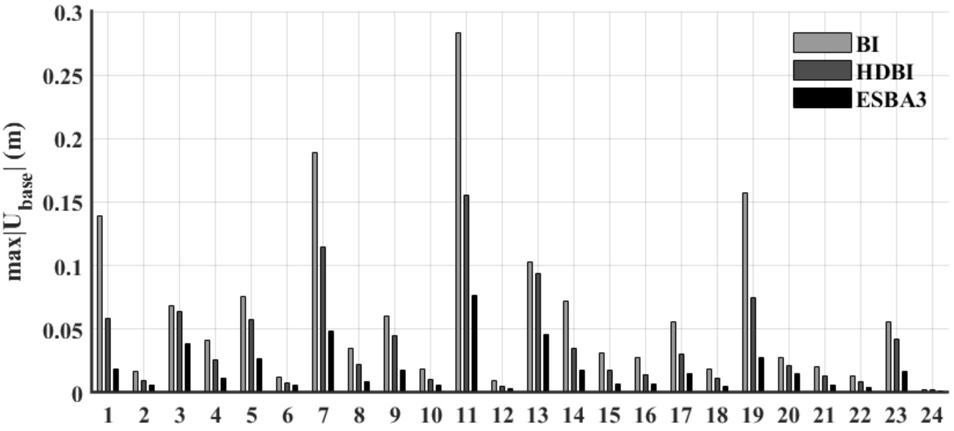

(b)

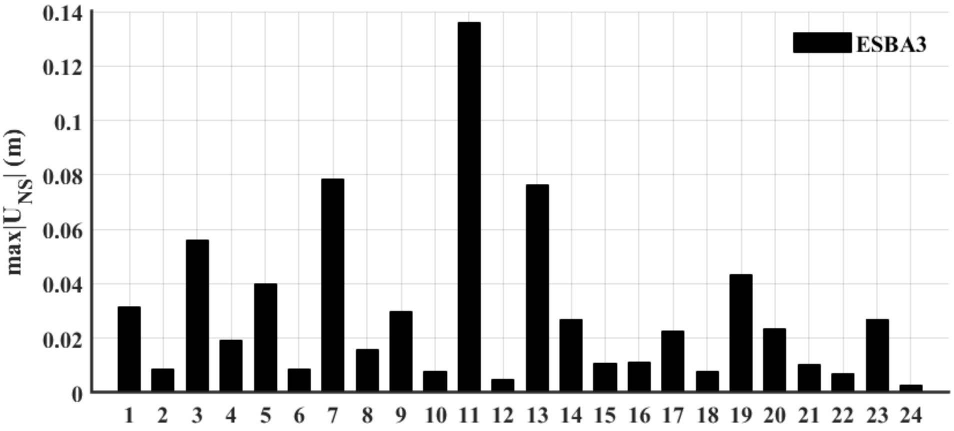

(c)

Figure 5.17: Main dynamic responses, for the 5-story building, of (a) first floor drift, (b) relative to the ground base displacement and (c) NS stroke between the fixed structure (IN), the conventional (BI) and highly damped (HDBI) base isolation and the ESBA-3 configuration (ESBA3), for all the near fault and far fault real earthquakes

The following figure (Fig. 5.18(a)-(e)) contains the mean maximum values of all the main dynamic responses of the relative to the ground displacement of the top floor, the absolute acceleration of the top floor, the base shear, the drift of the first floor, the relative to the ground displacement of the base and NS stroke for all the artificial, near fault and far fault earthquakes.

In (Fig. 5.18(a)), the ESBA-3 has the lowest relative to the ground displacement of the systems (including the fixed structure) for all the earthquakes. It exhibits a mean displacement of 0.072 m for all the artificial accelerations, 0.053 m for all the real NF and 0.014 m for all the FF, while the BI has respectively for the same responses, 0.233 m, 0.15 m and 0.036 m.

In (Fig. 5.18(b)), the ESBA-3 is located between the responses of the BI and HDBI for all the artificial and NF earthquakes, while it has a slightly larger performance of that of both the base isolation systems, regarding the absolute acceleration of the top floor. More specifically, the mean values are 5.32 m/s^2, 5.57 m/s^2 and 1.5 m/s^2 for all the artificial, the NF and the FF earthquakes, while the same values for the fixed structure (it has the largest values) and the HDBI (it has the smallest values), respectively, are the following by earthquake category: 14.93 m/s^2, 4.5 m/s^2, 9.56 m/s^2, 4.94 m/s^2, 3.21 m/s^2 and 1.3 m/s^2.

The next figure (5.18(c)) presents the base shear. Again, the ESBA-3 exhibits the same approximately behavior as the HDBI (in artificial has a bit lower response, whereas in NF a little larger). In FF it is located intermediately of the BI and HDBI. It yields a base shear of 1526 kN, 1081 kN and 307 kN, while the same responses of the fixed structure are 3804 kN, 2022 kN and 842 kN for all the artificial, NF and FF earthquakes, respectively.

The ESBA-3 manages, again, to maintain the lowest values of all the systems in terms of the drift of the first floor (except the FF case where it has a minor increased performance compared to that of the HDBI) and the base displacement. The drift variates from 0.33% (for all the artificial accelerations) to 0.24% (for all the NF) and 0.06% (for all the FF). The displacement of the base of the ESBA-3 variated from 0.039 m (all artificial earthquakes), to 0.029 m (all NF) and to 0.008 (all FF). With the same earthquake category order, the BI and HDBI responses are 0.159 m, 0.103 m and 0.025 m and 0.092 m, 0.064 m and 0.014 m, respectively.

Finally, in (Fig. 5.18(f)), it is noticed that the NS stroke is located within reasonable results, as it is 0.063 m for all the artificial, 0.047 m for all the NF and 0.012 m for all the FF.

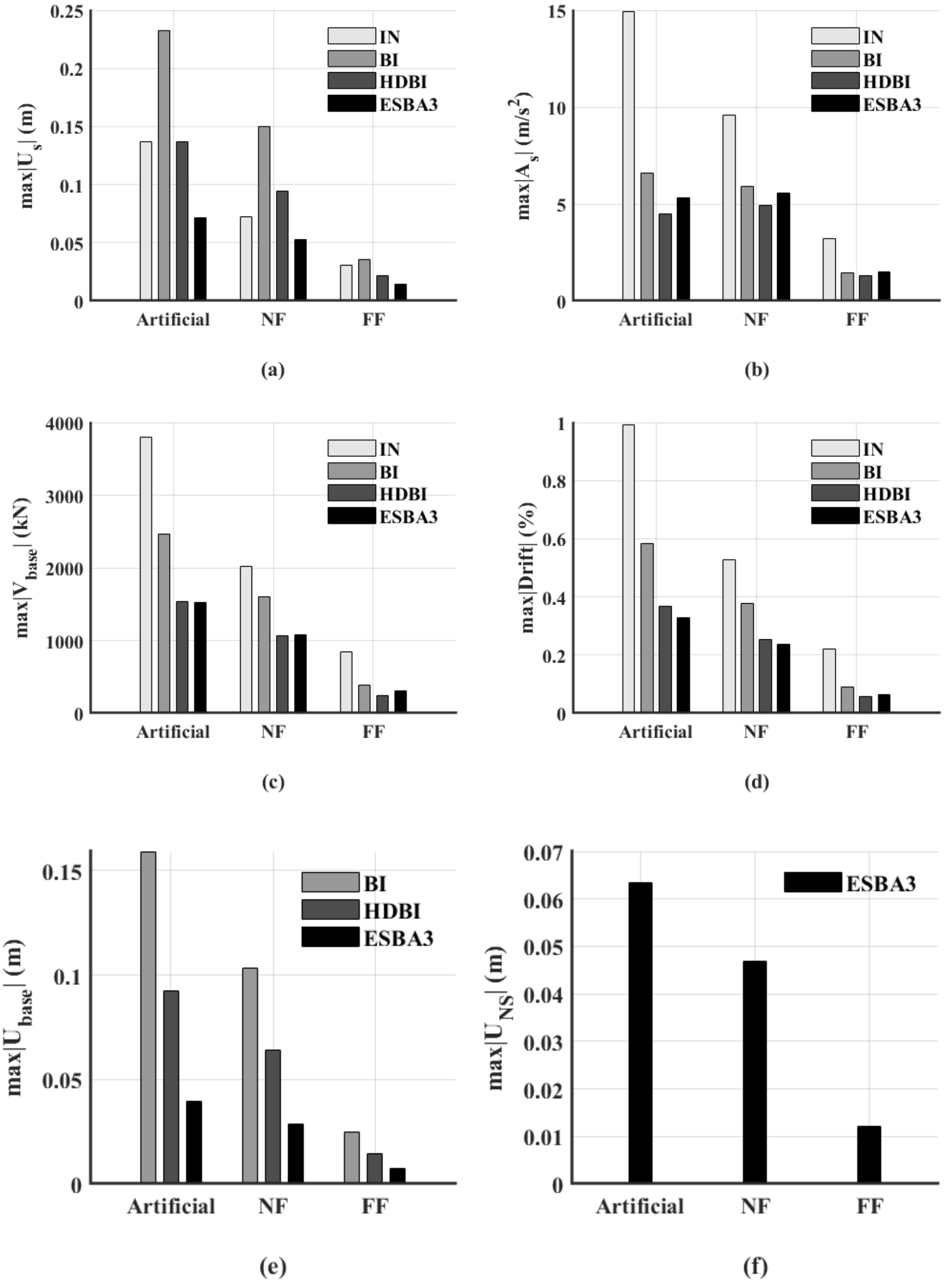

Figure 5.18: Mean maximum values of dynamic responses, for the 5-story building, of (a) top floor relative to the ground displacement, (b) top floor absolute acceleration, (c) base shear, (d) first floor drift, (e) relative to the ground base displacement and (f) NS stroke between the fixed structure (IN), the conventional (BI) and highly damped (HDBI) base isolation and the ESBA-3 configuration (ESBA3), for all the artificial accelerations and the near fault and far fault real earthquakes

6 DETUNING PHENOMENA AND GEOMETRIC NONLINEAR NEGATIVE STIFFNESS

6.1 Sensitivity analysis

6.1.1 One parameter sensitivity analysis

Once the optimal values of the parameters of the ESBA-3 configuration have been essentially established for an SDoF system and then tested on a 3-story and subsequently on a 5-story building, the next step is to perform a sensitivity analysis. This analysis is attempted to investigate how much the system's response deflects from its initial by altering the ESBA-3 configuration values of its parameters from their respective optimal ones (detuning phenomena). In this section (6.1.1), the variation of one parameter at a time (while all the rest remain intact) is chosen in the interval of $[0.8\ 1.2]P_{opt}$, where P_{opt} is the optimal value of the examined parameter. That means a variation of 20% from the initial original optimal values of the parameters is examined. The case of the ESBA-3 configuration with the acceleration filter of 50% is studied by considering the 3-story building of the section (5.3). In total 8 parameters are examined, that of the system's stiffnesses k_{NS}, k_R and k_{PS}, the artificial dampers of c_{NS} and c_{PS}, the inerter parameters of b_R and b_{NS} and since the b_{PS} was almost equal to 0, is not examined. Finally, the variation of the oscillating mass is searched separately in the interval of $[0.1\ 2]m_D$. The responses of the top floor relative to the ground displacement, top floor absolute acceleration, base shear, relative to the ground base displacement and the NS stroke with respect to the optimal ones of the 3-story building mounted on the ESBA-3 are presented. The whole system is subjected to all the artificial accelerations and the average responses are compared to the optimal ones.

In the following figure (6.1 (a)-(c)), there are the responses of the 3-story building with its ESBA-3 base by altering the values of the stiffness elements by 20%. Considering the top displacement, the negative stiffness has the largest impact, as it variates nearly from 1.12 to 0.96 of the optimal value for ±20% variation of the parameter value, while the structure stiffness exhibits minor variations for the most of the values. For the top acceleration, all the parameters yield nearly the same variation limits, with the structure stiffness k_R presenting slightly larger limits. As far as the base shear, the negative stiffness has the lowest variations from 1.06 to 0.97, while the structure stiffness has the largest from 0.84 to 1.16. Regarding the base displacement, the k_R seems to have a somewhat greater variation to the system rather than the negative stiffness, as the deviation fluctuates from 1.1 to 0.96. Finally, the negative stiffness presents the highest effect on the negative stiffness stroke as for a 20% increase of the parameter's value, the NS stroke is amplified to nearly 1.18 of the initial value. Overall, the negative stiffness k_{NS} and the structure stiffness k_R have a greater influence on the system responses (up to 18%), compared to the positive stiffness (up to 8%).

The next figure (6.2 (a) and (b)), includes the variation of the responses of the system, by considering a 20% alteration of the values of the damping coefficients. Considering the top displacement the positive damping seems to produce a minor influence as it variated from 0.99 to 1.01, while the negative from 1.02 to 0.99. Considering the top

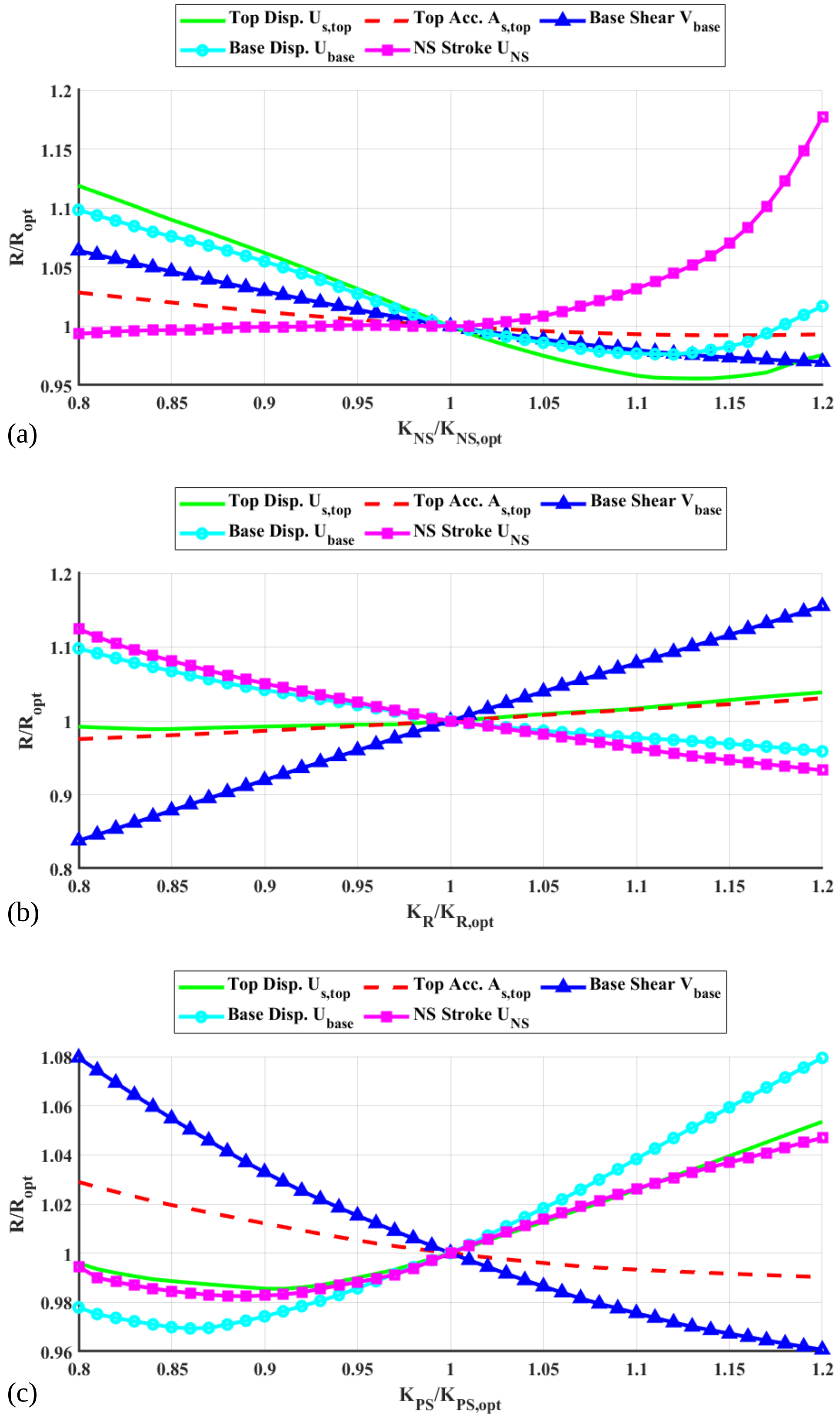

Figure 6.1: One parameter sensitivity analysis, considering 20% variation of the stiffness elements. (a) Negative stiffness k_{NS}, (b) structure stiffness k_R and (c) positive stiffness k_{PS}

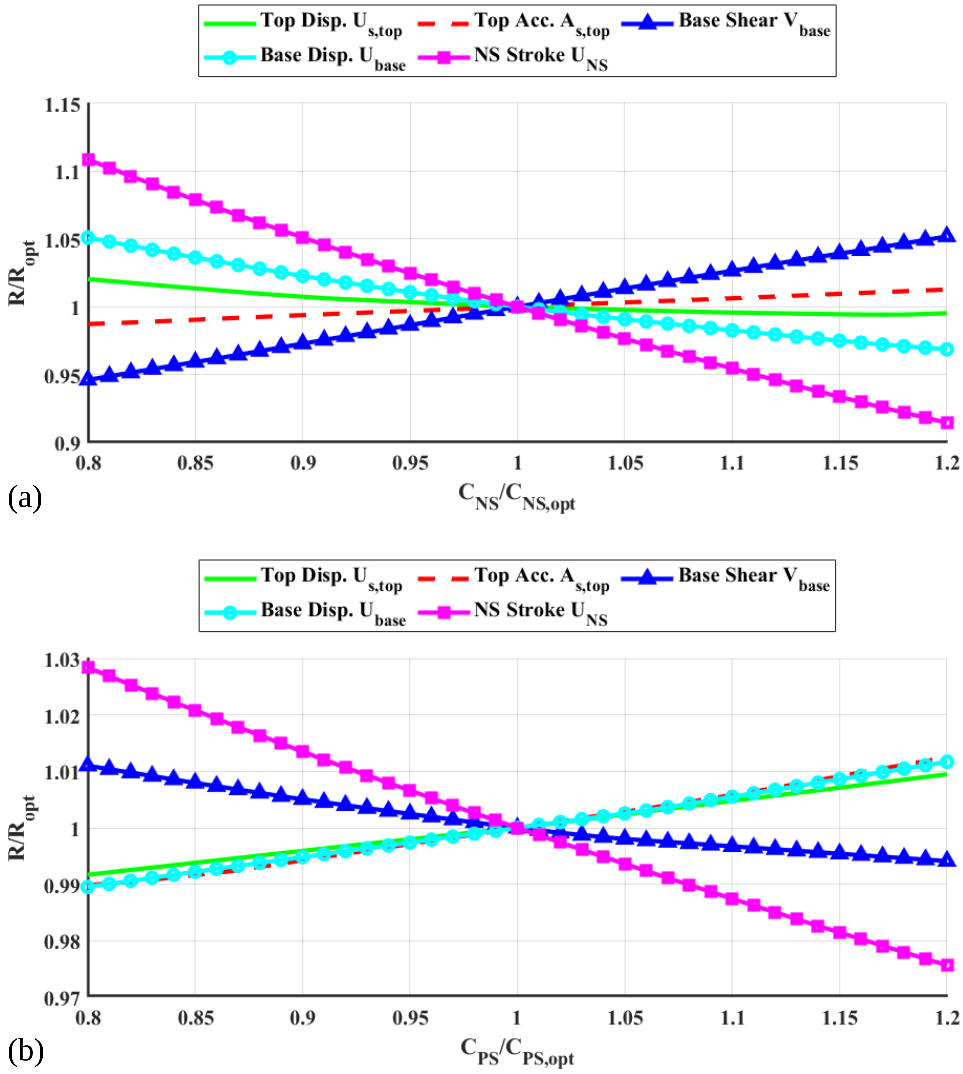

Figure 6.2: One parameter sensitivity analysis, considering 20% variation of the damping coefficients. (a) Negative damping coefficient c_{NS} and (b) positive damping coefficient c_{PS}

acceleration, both the damping coefficients present the same variation from 0.99 to 1.01. A variation up to 5% is observed with respect to the base shear from the negative damping, while the same response is only 1% for the positive. The same exactly variations (with opposite direction to that of the base shear) apply to the base displacement for both the damping coefficients. Finally, the largest variation is noted by the negative damping coefficient, regarding the NS stroke. It reaches an upper limit of 10% variation, while the same is lower than 3% for the positive damping coefficient. From all the above, it can be noticed that the negative damping coefficient has a larger impact on the system (up to 10% of the system responses variations) compared to that of the positive (up to 3% variations).

The figure below (6.3(a) and (b)), contains the variations of the system responses for a ±20% changing from the optimal values of the inerters that connect the base of the structure with the ground (b_R) and the inerter that is located parallel to the negative stiffness elements. As it can be seen, the variations for most of the system responses are similar to that of the positive damping coefficient, as up to 3% are the changes of

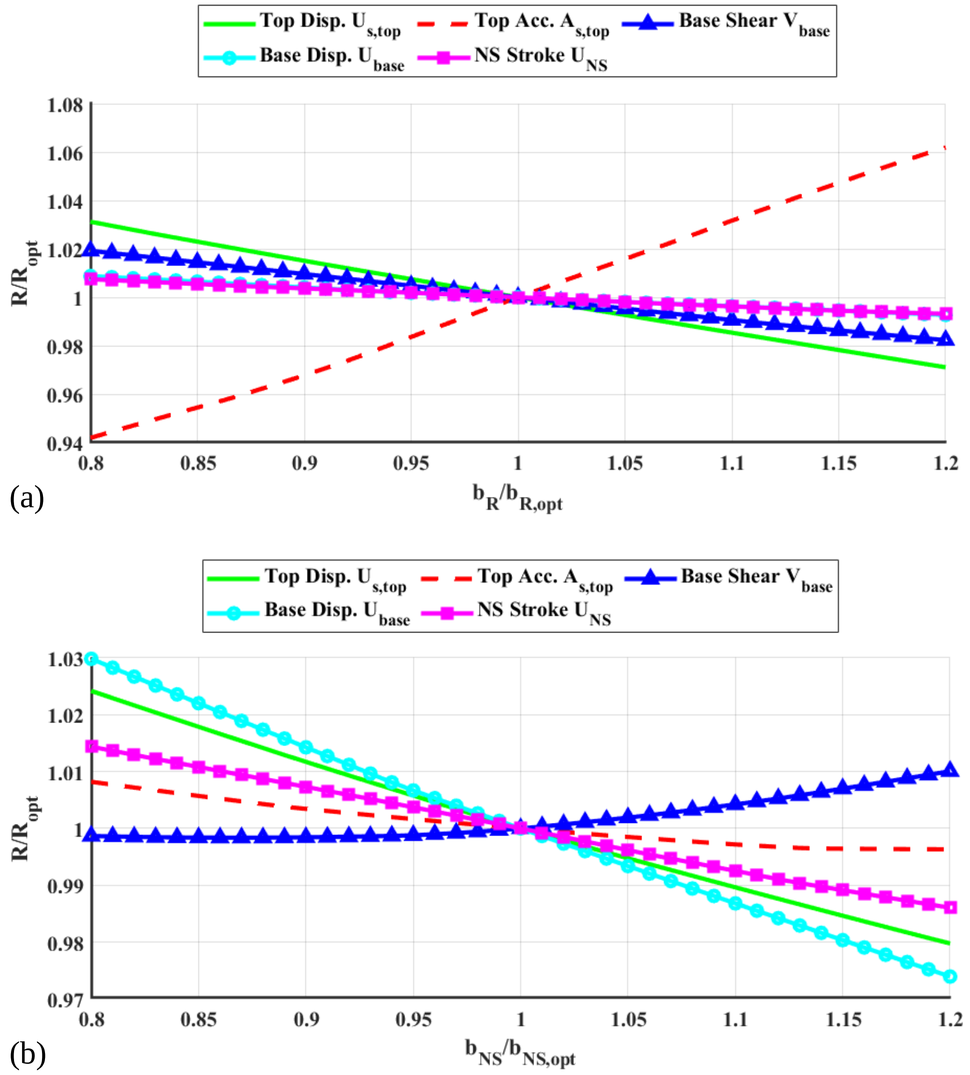

Figure 6.3: One parameter sensitivity analysis, considering 20% variation of the inerter values. (a) Inerter between the base structure and the ground b_R and (b) inerter parallel to the negative stiffness element b_{NS}

the values. The only differences is that the base shear follows an opposite trend in each case, as well as the top absolute acceleration and the latter response notes a variation of up to 6% for the b_R inerter. Due to that, this inerter has a larger consequence to the system responses than that located in parallel with the negative stiffness element.

Finally, in figure (6.4) the influence of the additional mass is examined. The variation of the mass takes place from 0.1 to 2 times of the initial mass. As it can be clearly observed, the variation of the additional mass has little to no impact on the structure's top displacement and acceleration. A 1% variation to the responses of the base displacement and NS stroke is noted. As the additional mass increases, the responses referring to the base are decreased. Finally, a 2% variation is discernible with respect to the base shear. If the responses, which are connected to the superstructure, are concerned, then a tenth of the initial mass of the oscillating mass could be adopted to further mitigate the constructional issues of the mass. However, if the base responses are of utmost importance, then the same or even increased values of the mass can be considered.

From all the above, the most crucial parameters that affect the global behavior of the system, is that of the stiffnesses and especially that of the negative stiffness. This parameter presented the highest variation in the system responses of 18% of all the parameters. However, for a variation of 20% of the values of the parameters from their respective optimal ones, the system noted reasonable alterations to its responses, without even developing extreme values for any of the responses of any of the examined parameters. Thus, it can be concluded that the system is not vulnerable to detuning effects, considering the sensitivity analysis that performed in this section.

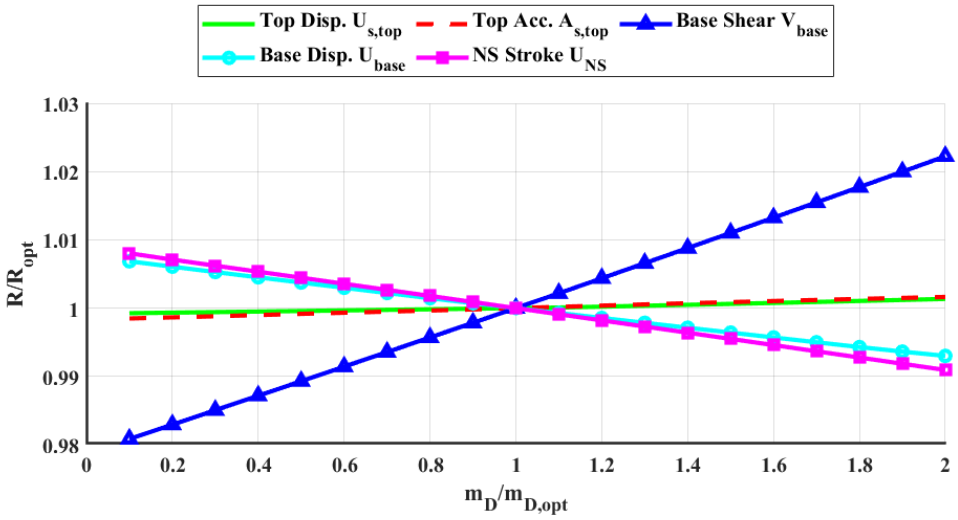

Figure 6.4: One parameter sensitivity analysis, considering a variation from 10% to 200% of the initial mass of the oscillating mass

6.1.2 Two parameter sensitivity analysis

A further investigation is performed to examine the detuning phenomena by considering a simultaneous variation of two parameters of the systems Again, the same conditions, as in the previous section (6.1.1), apply for this sensitivity analysis. All the possible couples of the free design parameters of the negative stiffness, the damping coefficients and the inerter values can be examined. For the sake of brevity of the present thesis, only four parameter combinations are listed. As it observed in the case of the one parameter sensitivity analysis, the negative stiffness parameter and subsequently the artificial damping parallel to the negative stiffness element have the largest influence on the system's dynamic performance. That is why the first parameter combination is that of the negative stiffness k_{NS} and its parallel damping c_{NS}. The second couple (following the same logic) is that of the negative stiffness and its parallel inerter b_{NS}. The other two combinations are related to the elements that produce similar resisting forces, like the two damping coefficients and the two inerters. In this case, three responses of the system are presented. The top floor absolute acceleration is chosen (as an indicative response of the superstructure) and the base displacement and the NS stroke, which refer to the base of the system.

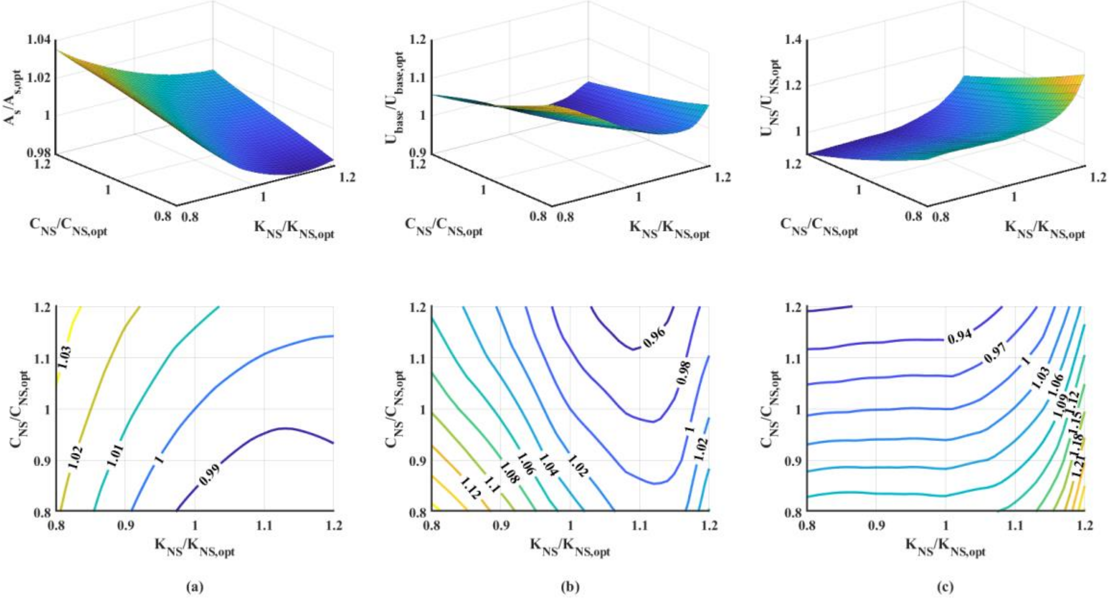

Figure 6.5: Sensitivity analysis and detuning effects of the top floor absolute acceleration (a), base displacement (b) and NS stroke (c) by varying the free design variables k_{NS} and c_{NS} from their optimal values

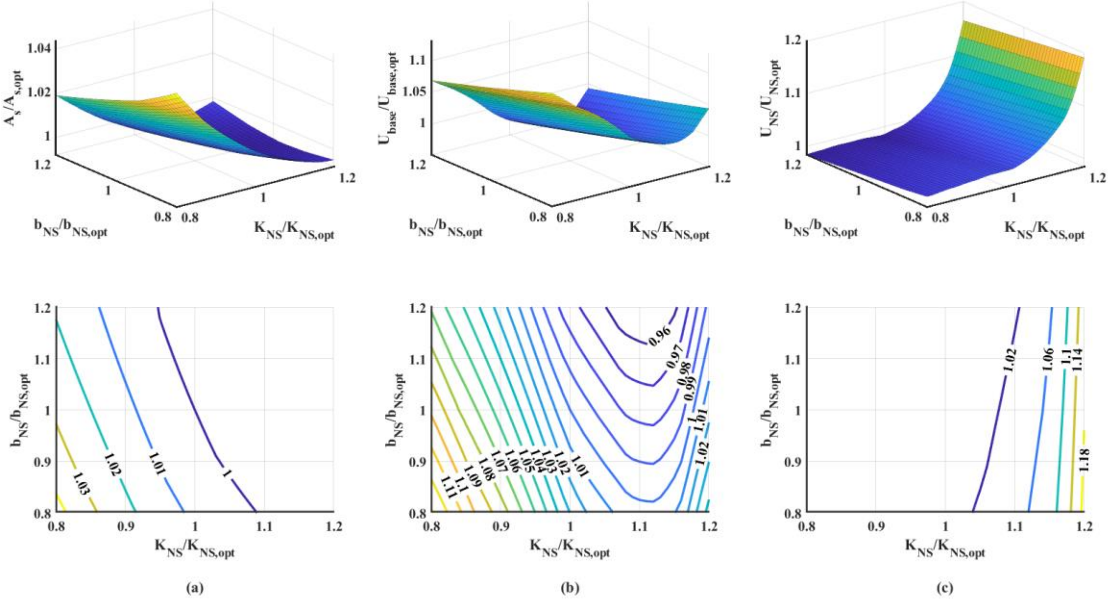

Figure 6.6: Sensitivity analysis and detuning effects of the top floor absolute acceleration (a), base displacement (b) and NS stroke (c) by varying the free design variables k_{NS} and b_{NS} from their optimal values

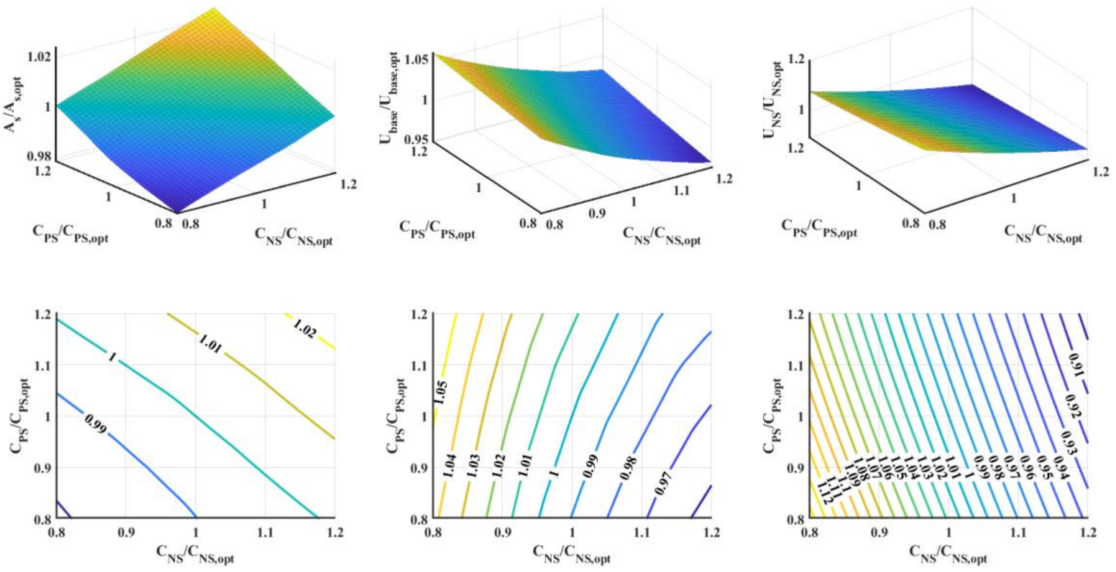

(a) (b) (c)

Figure 6.7: Sensitivity analysis and detuning effects of the top floor absolute acceleration (a), base displacement (b) and NS stroke (c) by varying the free design variables c_{NS} and c_{PS} from their optimal values

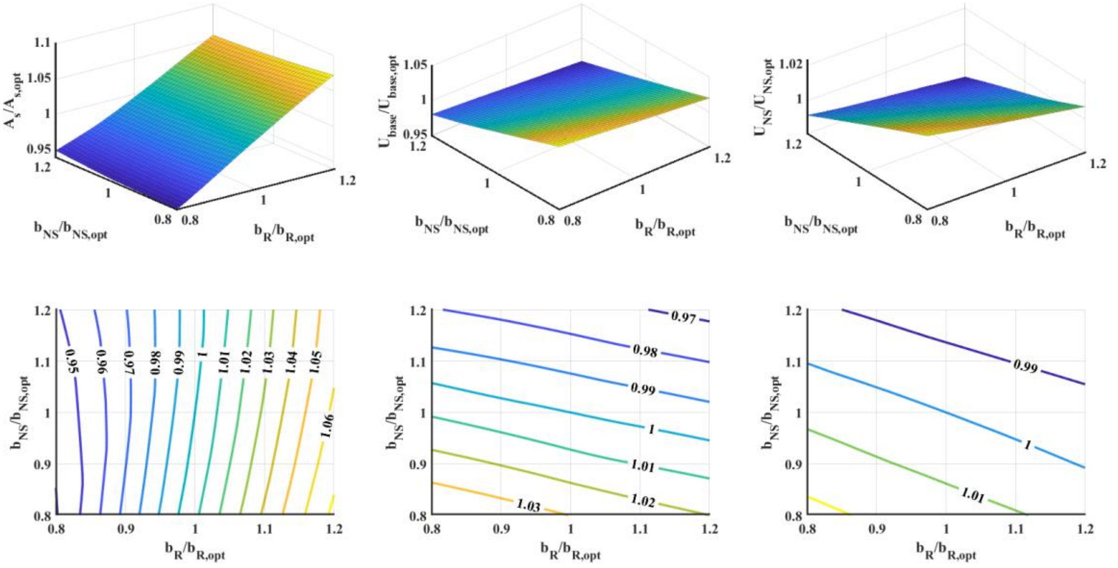

(a) (b) (c)

Figure 6.8: Sensitivity analysis and detuning effects of the top floor absolute acceleration (a), base displacement (b) and NS stroke (c) by varying the free design variables b_R and b_{NS} from their optimal values

Figure (6.5(a)-(c)), exhibits the surface plots and their equivalent contours of the simultaneous variation of the negative stiffness and the damping coefficient parallel to it. As it can be noticed, the absolute acceleration decreases by 2% at the lowest, where the negative stiffness is increased by 10% and the damping is lowered by 20%. The highest increase is noted by 3.5%, where the stiffness has the lowest value and the damping the highest. As far as the base displacement, this response is elevated to maximum by 16.5% for a simultaneous decrease by 20% of both the parameters, while nearly 5% is the lowest response when the damping achieves the highest value and the stiffness an approximate 10% increase. Finally, a nearly 30% amplification of the NS stroke is observed when the stiffness notes its highest value and the damping its lowest. At the exact opposite direction of the parameters' values, there is the lowest value of the stroke, that of roughly 10% decreased.

The next figure (6.6(a)-(c)), includes the surface plots and their equivalent contours of the simultaneous variation of the negative stiffness and the inerter parallel to it. As it can be observed, the absolute acceleration decreases by 1% at the lowest, where the negative stiffness and inertance increase. The highest increase is noted by slightly above 3%, where the stiffness and inertance obtain their lowest values. As far as the base displacement, this response is elevated to maximum by 13% for a simultaneous decrease by 20% of both the parameters, while nearly 5% is the lowest response when the inertance achieves the highest value and the stiffness an approximate 10% increase. Finally, a nearly 19% amplification of the NS stroke is observed when the stiffness notes its highest value and the inertance its lowest. At the exact opposite direction of the parameters' values, there is the lowest value of the stroke, that of roughly 1.5% decreased.

The next figure of (6.7(a)-(c)), contains the surface plots and their equivalent contours of the simultaneous variation of the negative and positive damping coefficients. As it can be seen, the absolute acceleration decreases by over 2% at the lowest, where the negative and positive damping coefficients receive their lowest values. The highest increase is noted by above 2%, where both the parameters have their highest values. As far as the base displacement, this response is elevated to maximum by 6% for a simultaneous decrease by 20% of the negative damping and 20% increase of the positive damping, while nearly 4.5% is the lowest response in the opposite direction of the variation of the parameters. Finally, a nearly 14.5% amplification of the NS stroke is observed when both damping coefficients obtain their lowest values. At the exact opposite direction of the parameters' values (20% increase for both), there is the lowest value of the stroke, that of roughly 10.5% decreased.

The last figure of (6.8(a)-(c)), presents the surface plots and their equivalent contours of the simultaneous variation of the negative and structure (external) inertance. As it can be noted, the absolute acceleration decreases by 6% at the lowest, where all the inertances receive their lowest values. The highest increase is noted by above 7%, where the external inertance has the highest value and the negative the lowest. As far as the base displacement, this response is elevated to maximum by a bit lower than 4% for a simultaneous decrease by 20% of both the parameters, while nearly above 3% is the lowest response when the two parameters receive their highest values. Finally, a nearly 2.3% amplification of the NS stroke is observed when both the external and negative inertances obtain their lowest values. At the exact opposite direction of the parameters' values (20% increase for both), there is the lowest value of the stroke, that of roughly 2% decreased.

Considering the top absolute acceleration, only in the case of the inertances (Fig. 6.8(a)), it can be observed that the one parameter (the external inertance specifically) influences the variation of the response. In the rest three cases both the parameters can have an effect on the response. The same approximately apply to the last two cases of both the damping coefficients and the inerters where the positive damping coefficient and the external inerter exhibit a smaller influence on this response compared to that of their counterpart parameter. Finally, by observing the NS stroke, the cases that involve the negative stiffness are those that one parameter does not have any special influence on the response variation. This is the negative stiffness up to a point compared to the negative damping coefficient and the negative inerter in the other case.

From all the above, again, it is shown that the negative stiffness is the most susceptible parameter for the variation of the responses, as it manages to exhibit a nearly 30% increase in the NS stroke in relation with the negative damping coefficient. On the contrary, the least effect on the system appears to be in the case of the inerters, as the maximum alteration of the optimal response is roughly at 7%. However, by a simultaneous variation of two parameters by ±20%, the system developed a reasonable deviation from its initial response, without noting extreme values. So, again, it is shown that the system is not vulnerable to detuning phenomena.

6.2 Geometric nonlinear negative stiffness

6.2.1 Realization of the negative stiffness element with pre – compressed springs

Negative stiffness is predominantly attained through specific mechanical designs that utilize conventional positive stiffness pre-stressed elastic mechanical elements. These elements, include post-buckled beams, plates, shells and pre-compressed springs that are arranged in suitable geometric configurations. This thesis applies configurations that employ pre-compressed springs into the mechanisms to achieve negative stiffness. The preference for such configurations arises from their simple design and the ease of controlling negative stiffness. These particular arrangements have the capability to provide the required negative stiffness to be applied in structural systems, such as the seismic protection of buildings.

By adopting the configuration in two dimensions proposed by (Kapasakalis A. K., 2020), based on the work of (Antoniadis, Kanarachos, Gryllias, & Sapountzakis, 2018), the negative stiffness in this work is realized. The two dimensional configuration is chosen as an effective horizontal seismic protection mechanism. According to (Fig. 6.9(b)), the negative stiffness element, as located in the position between the superstructure base and the additional mass, can be realized by a vertical pre-compressed spring with positive stiffness k_H, which supports the mass m_S by an articulated mechanism that includes a rigid link.

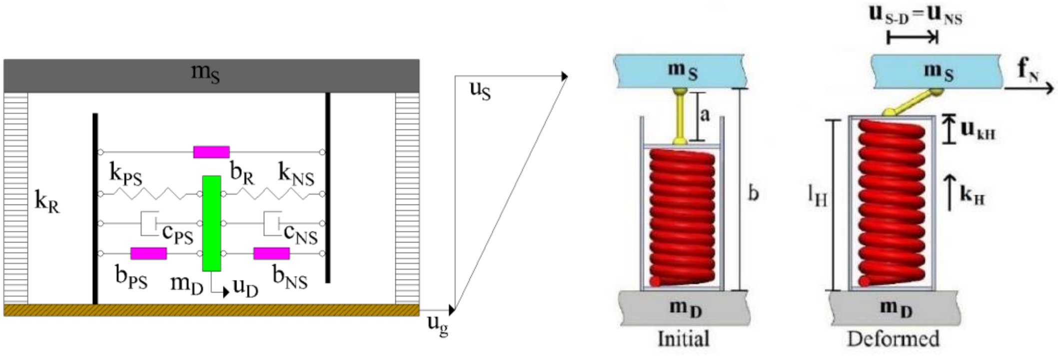

(a) (b)

Figure 6.9: (a) ESBA-3 proposed system and (b) negative stiffness element configuration

According to this mechanism, the equations of motion, which refer to the ESBA-3 configuration, are the following, in analogy with equations (4.8) and (4.9) by considering a ground excitation in the form of x_g:

$$[m_S + b_R m_S]\ddot{u}_s + (b_{NS} m_S)(\ddot{u}_s - \ddot{u}_D) + c_{NS}(\dot{u}_S - \dot{u}_D) + k_R u_S \\ + f_{NS}(u_{NS}) \;\; = -m_S \ddot{x}_g \tag{6.1}$$

$$[m_D + b_{PS} m_S]\ddot{u}_D - (b_{NS} m_S)(\ddot{u}_s - \ddot{u}_D) + c_{PS}\dot{u}_D - c_{NS}(\dot{u}_S - \dot{u}_D) \\ + k_{PS} u_D - f_{NS}(u_{NS}) = -\, m_D \ddot{x}_g \tag{6.2}$$

Where u_S and u_D are the relative to the ground displacements of the base and the additional mass. The term $f_{NS}(u_{NS})$ is the nonlinear force exerted by the positive stiffness spring and it depends on the relative displacement of the base and the oscillating mass (NS stroke).

The potential energy of the spring is the following:

$$U_{NS}\big(u_{NS}(u_D)\big) = \frac{1}{2} k_H (l_H - l_{HI})^2 \tag{6.3}$$

Where l_H and l_{HI} are the length of the spring in a randomly deformed instant and the initial undeformed length of the spring, respectively. Subsequently, the nonlinear force can be computed from the potential energy as follows:

$$f_{NS}(u_{NS}) = \frac{\partial U_{NS}}{\partial u_D} = \frac{\partial U_{NS}}{\partial u_{NS}} = -k_H\left(1 + \frac{l_{HI} - b}{\sqrt{a^2 - u_{NS}^2}}\right) u_{NS} = \\ -k_H\left(1 + c_I \frac{1}{\left(1 - \frac{u_{NS}^2}{a^2}\right)^{\frac{1}{2}}}\right) u_{NS} \tag{6.4}$$

From the equation (6.4), a is the length of the articulated mechanism (rigid link) that connects the additional mass with the base structure, b is the total length of the fully compressed spring and the articulated mechanism when those elements are coincidental (Fig. 6.9(b) initial) and the parameter c_I will be defined immediately after equation (6.5). Since the nonlinear force is available now, the negative stiffness emerges as below:

$$k_{NS} = \frac{\partial f_{NS}}{\partial u_D} = \frac{\partial f_{NS}}{\partial u_{NS}} = -k_H\left(1 + \frac{l_{HI}-b}{a}\frac{1}{\left(1-\frac{u_{NS}^2}{a^2}\right)^{\frac{3}{2}}}\right) = -k_H\left(1 + c_I\frac{1}{\left(1-\frac{u_{NS}^2}{a^2}\right)^{\frac{3}{2}}}\right) \tag{6.5}$$

The length of the spring can be defined as:

$$l_H = b - (a^2 - u_{NS}^2)^{\frac{1}{2}} \tag{6.6}$$

And the parameter c_I is:

$$c_I = \frac{l_{HI}-b}{a} \tag{6.7}$$

A realistic design of the ESBA-3 configuration is depicted in the figure (6.10) below. It follows the same logic as in the work of (Kapasakalis A. K., 2020). The vibration absorption system can be comprised by four in total devices, suitably located at the corners beneath of the base, on which the building with a plan floor of the figure (5.3) is mounted. At the columns locations, rigid elements can be considered that can withstand the large forces. Each device, now, is considered to bear eight positive stiffness springs of the vertical configuration of the figure (6.9(b)).

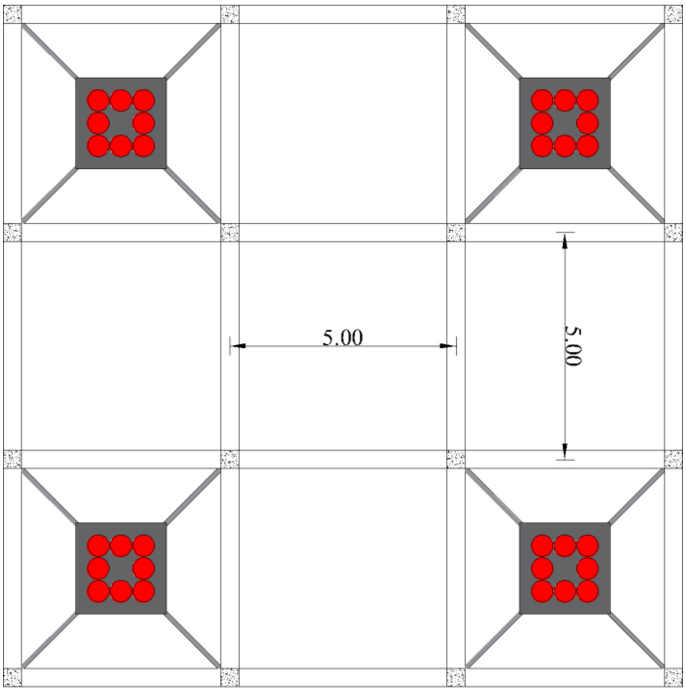

Figure 6.10: Layout of the ESBA-3 configuration devices and their respective positions in the base

So, by considering the ESBA-3 configuration with its parameters, which correspond to the 50% acceleration filter, the negative stiffness emerged at the value of -10702.5 kN/m according to the optimization process of the Chapter 4. That value corresponds to a negative stiffness of -334.45 kN/m per spring per device. For the realization of the positive stiffness spring, the comments from (Antoniadis, Kanarachos, Gryllias, & Sapountzakis, 2018) are adopted. The equivalent positive stiffness of the spring, that implements the negative stiffness, is yielded from equation (6.5) by considering a negative stiffness stroke of zero value. In this case the negative stiffness is configured at a 1% increased value of the respective optimal one. That means, $k_{NS}(u_{NS}=0)=1.01k_{NS}$ and it is -337.8 kN/m. However, the value of the parameter c_I remains unknown. This is set as a free design parameter. Three cases of the c_I parameter are considered, that of -0.01, -0.05 and -0.1. An analytical presentation of the last case follows, while only the results of the rest two values are included in the Tables (6.1) and (6.2). Generally, small values of the c_I parameter are chosen so as to guarantee a linear behavior as far as possible. Thus, for $c_I=-0.1$ and a zero NS stroke, a positive stiffness of k_H=375.33 kN/m is produced. The second parameter of a can be defined again from equation (6.5) (for a given, now, positive stiffness and the same c_I value) by considering the maximum value of the NS stroke. In this case the negative stiffness is set to be 10% less than the optimal one. That is $k_{NS}\left(u_{NS}=u_{NS,max}\right)=0.9k_{NS}$. It is -301.01 kN/m. The maximum NS stroke, as it also appears in the figure (5.5(c)), is 0.052m. Apart from the maximum NS stroke, a very small value of the order u_0=0.001 m is added to the NS stroke. A value close to 0, like the u_0 , is selected so that an almost symmetric response around u=0 is obtained. From these data, the parameter a equals to 0.0872 m for $c_I=-0.1$.

6.2.2 Nonlinear curves

A comparison is made between the nonlinear realization of the ESBA-3 configuration, for the $c_I=-0.1$ parameter and the respective linear one. The linear is considered to be the same exactly case as in the section (5.3). The nonlinear one has the same exact parameters as the linear that refer to the 3-story building and adopts the configuration analyzed in the previous section (6.2.1). Both systems are subjected to the same random artificial acceleration that used in the optimization processes. The yielding results are presented in the figure (6.11) that follows.

Prior to that, it is worth mentioning that all analyses are performed with the same Newmark algorithm, with the difference that a portion of it is modified to include this geometric nonlinearity. The geometric nonlinearity is included in the negative stiffness (Eq. 6.5), as it depends on the NS stroke. So, by taking the pseudo-code algorithm of the section (4.2.4), all alterations performed are highlighted with red to distinguish the old steps with the current ones to compute the nonlinear responses.

Algorithm: Constant average acceleration method (NS stroke)

```
Determine parameters $\gamma$ and $\beta$ (=0.5 and 0.25, respectively for constant average acceleration method)
Step 1: Initial calculations
```

```
    1.1 Initial conditions $\boldsymbol{u}(0), \dot{\boldsymbol{u}}(0), u_{NS,init}, \boldsymbol{K}_{init} = f(k_{NS} = g(u_{NS,init}))$ (Eq. 5.6 & 6.5)
    1.2 Initial load $\boldsymbol{p}(0) = -\boldsymbol{\tau}\ddot{\boldsymbol{x}}_g(0)$
    1.3 Initial acceleration: $\ddot{\boldsymbol{u}}(0) = [\boldsymbol{M}]^{-1}(\boldsymbol{p}(0) - \boldsymbol{C}\dot{\boldsymbol{u}}(0) - \boldsymbol{K}_{init}\boldsymbol{u}(0))$
    1.4 Select $\Delta t$
    1.5 Compute: $\mathbf{a}_1 = \frac{1}{\beta(\Delta t)^2}\boldsymbol{M} + \frac{\gamma}{\beta\Delta t}\boldsymbol{C}$; $\mathbf{a}_2 = \frac{1}{\beta\Delta t}\boldsymbol{M} + \left(\frac{\gamma}{\beta} - 1\right)\boldsymbol{C}$;
        $\mathbf{a}_3 = \left(\frac{1}{2\beta} - 1\right)\boldsymbol{M} + \Delta t(\frac{\gamma}{2\beta} - 1)\boldsymbol{C}$
    1.6 Compute: $\widehat{\boldsymbol{K}}_{init} = \boldsymbol{K}_{init} + \mathbf{a}_1$
Step 2: Calculations for each time step, $i = 0, 1, 2, \ldots$
    2.1 $\widehat{\boldsymbol{P}}_{i+1} = -\boldsymbol{\tau}\ddot{\boldsymbol{x}}_{g,i+1} + \mathbf{a}_1\boldsymbol{u}_i + \mathbf{a}_2\dot{\boldsymbol{u}}_i + \mathbf{a}_3\ddot{\boldsymbol{u}}_i$
    2.2 Solve: $\widehat{\boldsymbol{K}}_i\boldsymbol{u}_{i+1} = \widehat{\boldsymbol{P}}_{i+1} \;\; => \;\; \boldsymbol{u}_{i+1} = [\widehat{\boldsymbol{K}}_i]^{-1}\widehat{\boldsymbol{P}}_{i+1}$
    2.3 $\dot{\boldsymbol{u}}_{i+1} = \frac{\gamma}{\beta\Delta t}(\boldsymbol{u}_{i+1} - \boldsymbol{u}_i) + \left(1 - \frac{\gamma}{\beta}\right)\dot{\boldsymbol{u}}_i + \Delta t\left(1 - \frac{\gamma}{2\beta}\right)\ddot{\boldsymbol{u}}_i$
    2.4 $\ddot{\boldsymbol{u}}_{i+1} = \frac{1}{\beta(\Delta t)^2}(\boldsymbol{u}_{i+1} - \boldsymbol{u}_i) - \frac{1}{\beta\Delta t}\dot{\boldsymbol{u}}_i - \left(\frac{1}{2\beta} - 1\right)\ddot{\boldsymbol{u}}_i$
    2.5 $u_{NS,i+1} = \left(u_{base,i+1} - u_{add.mass,i+1}\right) + u_{NS,init}$ (NS stroke computation)
    2.6 $k_{NS,i+1} = f(u_{NS,i+1})$ (Eq. 6.5), update $\boldsymbol{K}_{i+1}{}^{ESBA-3}$(Eq. 5.6), update
        $\widehat{\boldsymbol{K}}_{i+1} = \boldsymbol{K}_{i+1}{}^{ESBA-3} + \mathbf{a}_1$
Step 3: Repetition for the next time step. Replace $i$ by $i + 1$ and implement steps 2.1 to 2.6 for the next time step
```

Since the $c_I = -0.1$ parameter has a small value, a quasi linear behavior is expected. That is why the same procedure, as in the linear problem, is followed here, considering the change and update of the whole system's stiffness within the steps 2.1 to 2.6 (as they appear in the above pseudo-code). Moreover, the next step is considered to change infinitesimally with its previous, so that is why, again, the stiffness, used to yield the next displacements, can be changed with the previous practically displacements (NS stroke).

By implementing all these, in figure (6.11(a) to (f)) the top floor relative to the ground displacement, the top floor absolute acceleration, the base shear, the drift of the first floor, the relative to the ground displacement of the base and the NS stroke of the ESBA-3 configuration with the nonlinear negative stiffness realization with $c_I = -0.1$, are presented and compared with the same responses of the respective linear one. As it can be clearly observed, all curves, referring to the nonlinear realization, are in quite satisfactory agreement with the responses yielded from the same linear problem. In the biggest part of each curve/response of the nonlinear realization there is complete coincidence with the curve of the linear one, with the exception of some regions and peaks where there is a slight deviation. More specifically, in (Fig. 6.11(a)), the nonlinear configuration notes a maximum relative displacement of 0.042 m (3.39% increased with respect to the linear displacement of 0.041 m), while the acceleration of

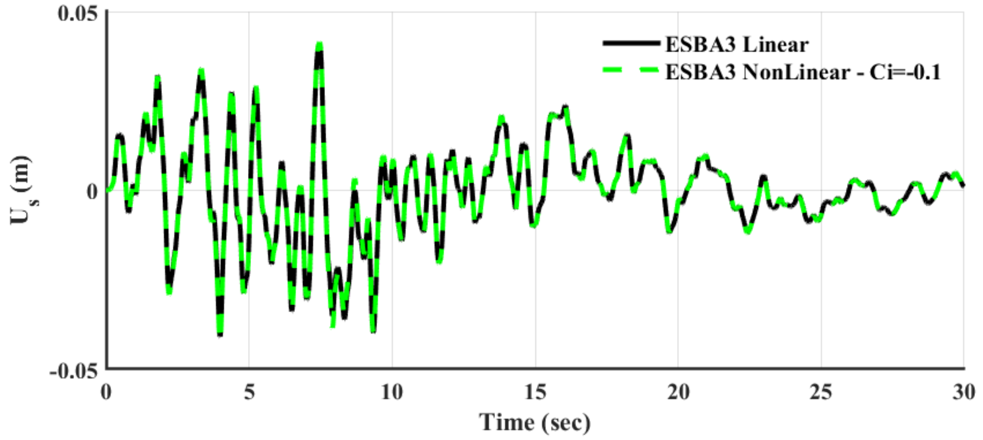
0.05
0
-0.05
U_s (m)
0
5
10
15
20
25
30
Time (sec)
ESBA3 Linear
ESBA3 NonLinear - Ci=-0.1

(a)

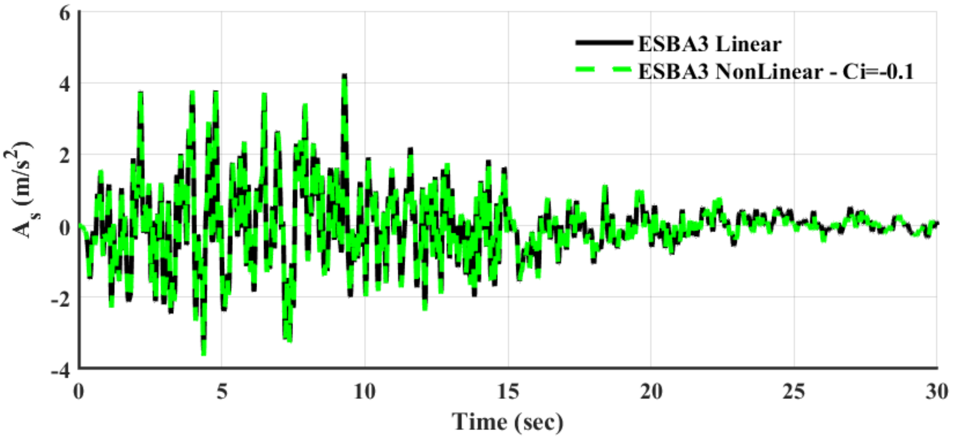
6
4
2
0
-2
-4
A_s (m/s^2)
0
5
10
15
20
25
30
Time (sec)
ESBA3 Linear
ESBA3 NonLinear - Ci=-0.1

(b)

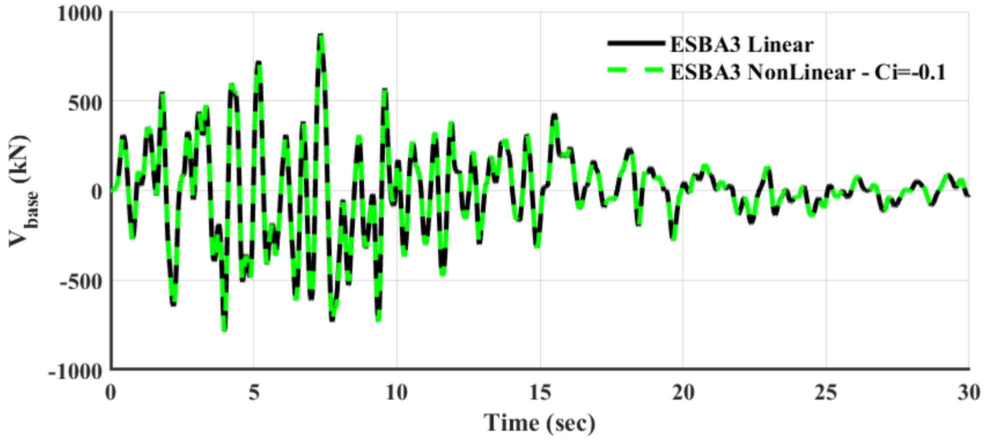
1000
500
0
-500
-1000
V_base (kN)
0
5
10
15
20
25
30
Time (sec)
ESBA3 Linear
ESBA3 NonLinear - Ci=-0.1

(c)

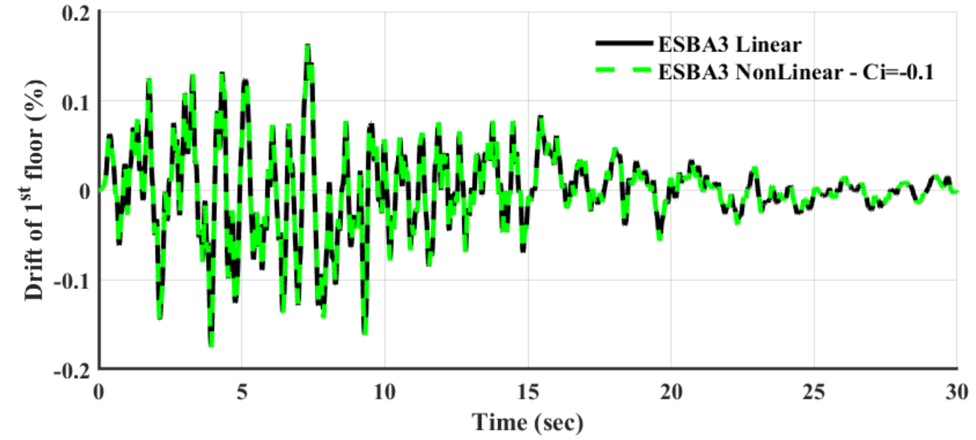

(d)

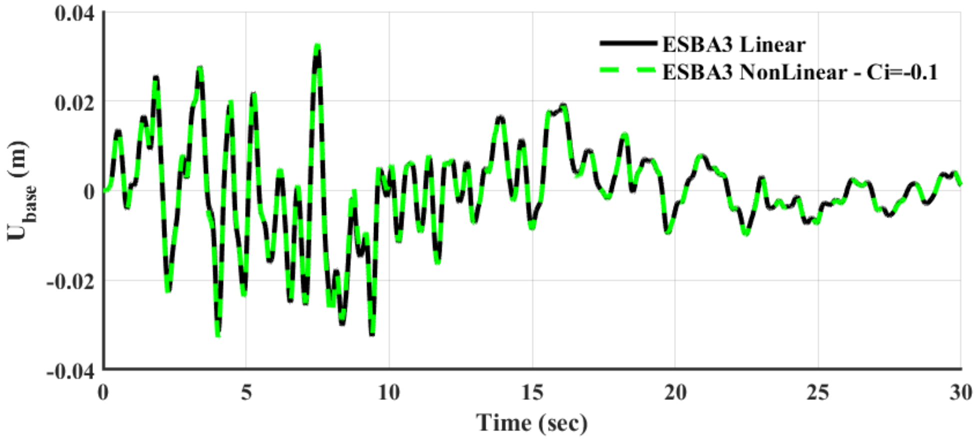

(e)

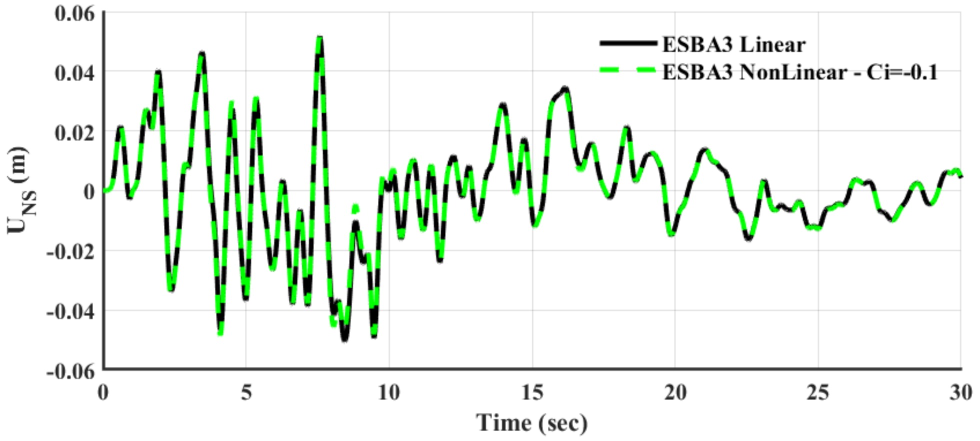

(f)

Figure 6.11: Dynamic responses of the ESBA-3 system (50% acceleration filter), considering linear NS and non-linear NS (for c_i=-0.1) for the random acceleration. (a) Top floor relative to the ground displacement of the 3-story building, (b) top floor absolute acceleration of the 3-story building, (c) base shear, (d) drift of the first floor, (e) relative to the ground base displacement and (f) NS stroke

the top floor in Fig. 6.11(b), appears to be 4.26 m/s^2 a value slightly over by 0.29% of the 4.25 m/s^2 of the linear problem. In figure 6.11(c), the base shear of the nonlinear problem reaches the same value of the linear of 876.57 kN (in particular only a 0.0007% difference), which means the responses fully coincide together. The same tendency of the extremely close behavior is depicted in the figure (6.11(d)), where the drift of the first floor is 0.175% for both cases, which is translated into a 0.15% difference with respect to the linear problem, if more digits for accuracy are considered. Finally, the figures 6.11(e) and 6.11(f) show the displacement responses that are related to the base. The relative to the ground base displacement and the NS stroke are 3.28 cm and 5.13 cm, respectively, which means there is an increase by 0.94% compared to the base displacement of 3.25 cm of the linear problem and a decrease by 0.8% with respect to the linear NS stroke of 5.17 cm.

The following figure (6.12) contains the variation of the negative stiffness over the NS stroke, according to Eq. (6.5), considering all the positive stiffness springs that compose the negative stiffness. It variates between the imposed limits of the 90% and the 101% of the optimal value.

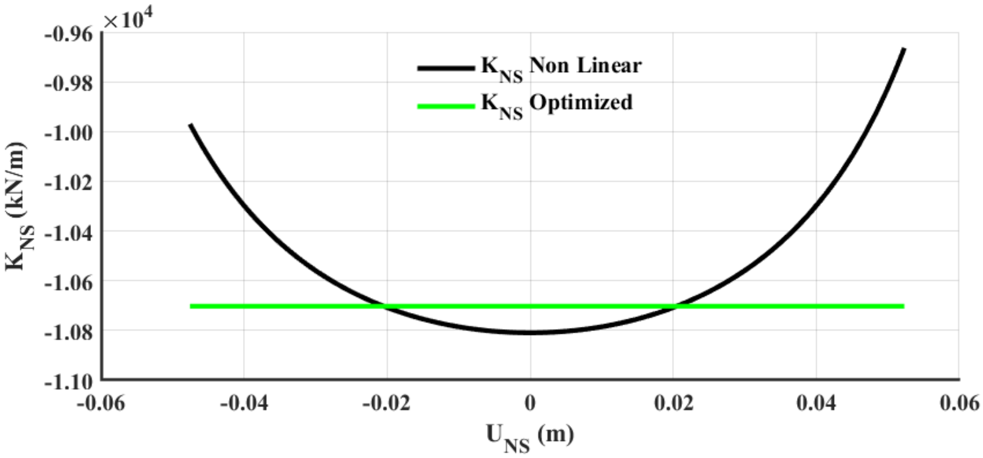

Figure 6.12: Variation of the generated negative stiffness, of the proposed configuration of ESBA-3, over the NS stroke

The Table (6.1) below, contains the parameters k_H (per spring) and a that are necessary to compute the nonlinear responses for all three cases of the parameter c_I.

Table 6.1: Values of parameters k_H and α for various cases of the c_I parameter

c_I	k_H (kN/m)	a (m)
-0.01	341.21	0.0587
-0.05	355.58	0.0727
-0.1	375.33	0.0872

The next table (6.2), includes all the maximum dynamic responses, for all three cases of the c_I parameter, compared to the maximum respective dynamic responses of the linear problem (expressed in % deviation). The (-) sign declares that the response is larger than that of the linear one. As it can be observed, the increase of the c_I parameter leads to the growth of the deviation of the responses that are related to the superstructure (relative to the ground displacement and absolute acceleration of the top floor and the first floor drift) with respect to the same linear ones. In those responses, and especially in the displacement, the largest difference of the 3.39% of the nonlinear problem, compared to the linear, is noted. All these responses appear to be larger than the linear ones. In reference with the responses related to the base, such as the base shear, the base displacement and the NS stroke, the first and the third one follow an opposite pattern than that of the responses of the superstructure, while the second follows a random scheme. The amplification of the c_I parameter results to the decrease of the deviation from the linear responses of the base shear and the NS stroke, all lower from the linear problem. The base displacement lowers and increases. All the base displacements are larger than that of the linear statement of the problem.

Table 6.2: Differences (in %) of the maximum dynamic responses of various nonlinear cases with respect to the linear ones

c_I	**% difference from U_S^{Linear}**	**% difference from A_S^{Linear}**	**% difference from V_{base}^{Linear}**	**% difference from $Drift_{1^{st}}^{Linear}$**	**% difference from U_{base}^{Linear}**	**% difference from $U_{NS\ stroke}^{Linear}$**
-0.01	-0.9894	-0.0619	0.0453	0.0428	-0.4569	1.2921
-0.05	-2.7426	-0.2284	0.0119	-0.1056	-0.3750	1.0084
-0.1	-3.3924	-0.2878	7.4760e-04	-0.1457	-0.9422	0.7990

As concluded, the negative stiffness can be realized with positive stiffness pre-compressed springs that develop a nonlinear behavior very close to that of the linear problem. For various values of the c_I parameter that controls the nonlinearity, the largest deviation from the linear problem comes from the largest value of that parameter and reached the 3.39% from the same response of the linear problem. From the time histories of the dynamic responses, the nonlinear configuration is in agreement with the linear cases to a very satisfying extent.

6.2.3 Realization of the ESBA-3 configuration

The next step is to implement the ESBA-3 configuration with realizable elements.

- Starting from the additional mass, this element can be realized by considering a concrete material with density of $\rho_{conc} = 2400$ kg/m^3. Since the ESBA-3 can be realized by four devices, each one can include an oscillating mass of 750 kg, which corresponds to the one fourth of the 1% of the total mass of the superstructure. If a square floor plan is assumed with a height of 0.25 m, then the sides of it are defined as: $s_{sq} = \sqrt{\frac{750}{2400 \cdot 0.25}} \approx 1.12$ m. Figure (6.13) shows an indicative model of the additional mass.

- The negative stiffness, as it was analyzed in the section (6.2.2), can be realized with eight positive stiffness pre-compressed helical springs per device, having a numerical positive stiffness of 375.33 kN/m. This, can be produced by implementing the theory of mechanical springs, provided by (Budynas & Keith, 2011). The spring rate, or scale, or the stiffness can be defined by the following relation:

  $$k_{spr} = \frac{d^4 G}{8 D^3 N} \tag{6.8}$$

  where, d is the wire diameter of the helical spring, G is the shear modulus of the spring's material, D is the mean coil diameter which equals to the external diameter subtracting the wire diameter and N is the number of coils of the helical spring. By considering a 26 mm wire diameter, 80.77 GPa steel material, 161 mm external diameter (which corresponds to a 135 mm mean diameter) and five coils and using the (6.8) equation, the positive stiffness is realized as 375.04 kN/m, very close to the theoretical one. A mean diameter larger than five times the wire diameter can ensure a linear behavior of the spring. In this way, the length of this spring, when it is fully compressed, is defined as $l_{min} = N \cdot d = 0.13\ m$ and subsequently, the length of the spring, when it is fully undeformed, is demanded to be $l_{HI} = l_{min} + a = 0.217\ m$. So, the length b can be computed with the aid of the equation (6.7) and emerges as 0.226 m. It is almost 9 mm larger than the undeformed length l_{HI} and this renders the articulated mechanism functional. Figure (6.14) depicts a five coil helical spring that can be used to realize the negative stiffness element.
- Continuing with the base stiffness k_R, from the optimization procedure, it reached the value of 30072.51 kN/m. The realization of the positive stiffness elements is possible in various ways, like, conventional steel spiral springs, simple elastomeric bearings (or any type of special bearings), or even conventional structural elements (Kapasakalis, Antoniadis, & Sapountzakis, 2022). For the ESBA-3 configuration, simple elastomeric bearings (SI series elastomeric isolators) are chosen to realize the k_R stiffness. They can be found in the catalogue of (FIP INDUSTRIALE, 2010). The series of SI elastomeric isolators are reinforced rubber bearings made up of alternating layers of steel laminates and hot-vulcanized rubber. From the catalogue, a maximum design displacement is required to choose from. The k_R stiffness is directly connected to the maximum base displacement. From (Fig. 6.11) the maximum base displacement for the nonlinear problem is 3.28 mm, which is way too lower than the 100 mm, the lowest design displacement category from the catalogue. So, by considering two SI isolators per device, the stiffness that corresponds to each isolator is 3759.06 kN/m. From a maximum design displacement of 100 mm and by adopting a hard type elastomeric compound, the SI-H 450/54 type of isolator is chosen. (Fig. 6.15) shows a similar SI isolator that can be used to generate the k_R stiffness.

- The same exactly apply to the positive stiffness element k_{PS}. From the optimization process, the total positive stiffness was 23150.97 kN/m. This term is connected to the maximum displacement of the additional oscillating mass. The nonlinear problem produced a maximum displacement of 3.12 cm. Again, elastomeric isolators from the same series (SI-H for 100 mm maximum design displacement) can be used to realize the positive stiffness. As, before, by utilizing two isolators per device, each isolator should generate 2893.87 kN/m. That value, corresponds to the type of SI-H 400/50 (the previous product from the same series of the k_R isolator). The same figure (6.15) shows the isolator that can be used for the k_{PS} stiffness.
- Considering the damping coefficient that is parallel to the negative stiffness element c_{NS}, the total value of 840.51 kNs/m emerged from the optimization procedure. If six parallel elements are implemented per device, then 35.02 kNs/m correspond to each device. Since this is a low value, linear artificial dampers of the series LD1110 for a maximum design stroke of 100 mm, can be used according to the catalogue of (ITT ENIDINE Inc., 2020). The figure (6.16) depicts a linear artificial damper that can be used to generate the c_{NS} damping coefficient.
- Similar configuration can be used to implement the damping coefficient parallel to the positive stiffness element c_{PS}, as the values produced in this case are quite close to that of the negative damping coefficient. The total damping in this case is 895.72 kNs/m. By considering again, as previously, six parallel artificial dampers per ESBA-3 device, then a value of 37.32 kNs/m per damper corresponds. This is a very close value to the negative stiffness damper and as a consequence, the same LD1110 configuration can be used also in this case. The figure (6.16) applies to this case.
- The ideal inerter can be defined as *a mechanical two-node (two-terminal), one-port device with the property that the equal and opposite force applied at the nodes is proportional to the relative acceleration between the nodes*, according to (Smith, 2002). A very brief reference is made to the flywheel-based mechanical inerter, patented by (Smith, 2002). This device can be practically realized via a suitable arrangement of rack, pinions, gears and a flywheel, as it can be seen in the figure (6.17). This arrangement has the capacity to transform the linear movement of the rack into rotational one of the pinions, gears and the flywheel. The one terminal, which is the ending of the rack, moves linearly to the other terminal, in which the system that contains all the rotational elements is connected. So, the linear movement of the rack renders the rotation of the first gear that is in direct contact with it, via its pinion. Then, the rotational movement is transferred from on gear to another via a pinion-gear contact rotation. The number of gears can be from one to several, which the last one ends up rotating the flywheel. Finally, the rotation of the flywheel creates an inertial force from its rotational inertia (angular mass). This configuration generates an inertial force that can be described from the following relation:

$$F_{in} = b_f(\ddot{x}_1 - \ddot{x}_2) \tag{6.9a}$$

where the term $\ddot{x}_1 - \ddot{x}_2$ is the relative acceleration between the two terminals and the b_f is the inertance, having dimensions of mass. This is defined as:

$$b_f = m_f \left(\frac{r_f}{r_{pf}}\right)^2 \left[\prod_{i=1}^{n_g} \left(\frac{r_i}{r_{pi}}\right)^2\right] \tag{6.9b}$$

where, n_g is the number of gears, m_f is the mass of the flywheel and r_i, r_{pi}, r_f and r_{pf} are the radius of the gears, the pinions, the flywheel and the flywheel pinion, respectively. From the equation (6.9b), by simply adjusting the gear ratios or by adding gear sets, very high values of inertance can be achieved. So, by considering the external inertance b_R of the ESBA-3 configuration, a total value of 0.4993m_S=149790 kg is required, according to the optimization procedure. If two inerter elements, per device, are implemented, then an inertance of 18723.75 kg is demanded per element. By considering two gears with 3 gear-to-pinion ratio each and a flywheel with a 4 ratio of its gear to its pinion, then a flywheel of mass of 14.447 kg is needed to satisfy this configuration.

- Following the same exact logic, the inerter parallel to the negative stiffness element can be realized with the same exact configuration. The total inertance required, according to the optimization, is 0.2113m_S=63390 kg. Again, by considering two inerter elements per device, an inertance of 7923.75 kg corresponds to every element. By adopting the same configuration of two gears with a gear-to-pinion ratio of 3 and a ratio for the flywheel gear-to-pinion of 4, a mass of 6.114 kg of the flywheel is required to generate this inertance. The figure (6.17) applies to this case.
- Finally, the inerter element, parallel to the positive stiffness element, can be omitted, since an almost equal to 0 value emerged from the optimization. For lower acceleration filters, this inerter can be realized with a similar way as the two previous inerters.

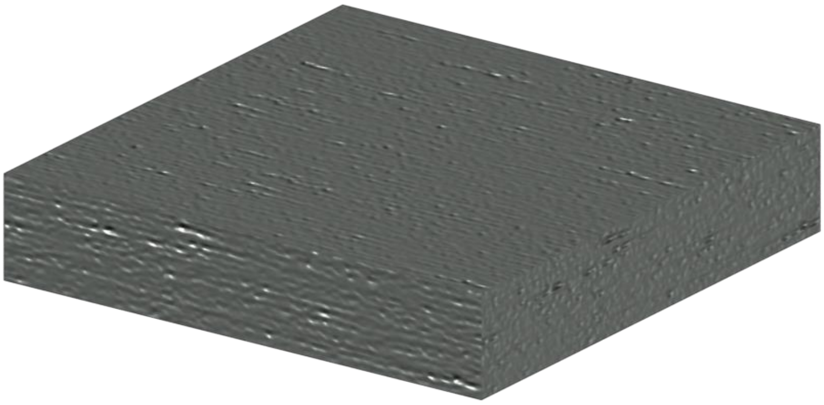

Figure 6.13: Concrete square floor plan additional oscillating mass

Figure 6.14: Five coil helical spring used to realize the negative stiffness element

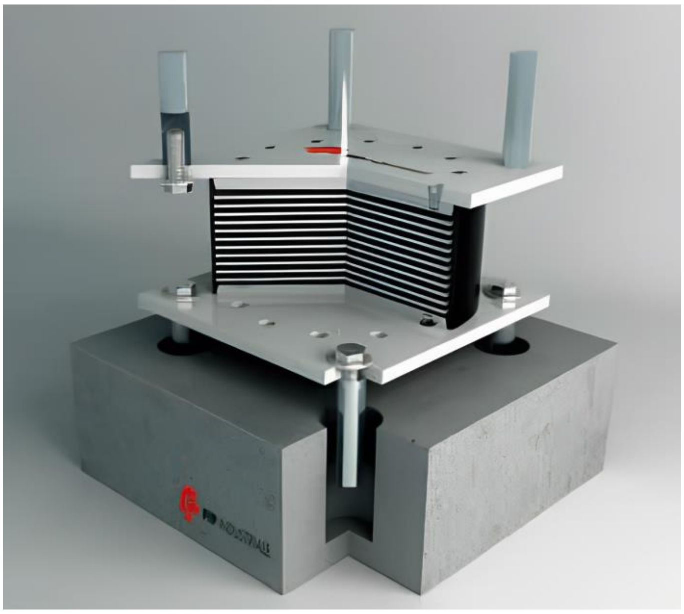

Figure 6.15: SI elastomeric isolator (from FIP INDUSTRIALE) used to realize the k_R and k_{PS} stiffnesses

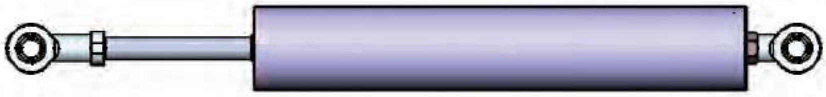

Figure 6.16: Linear damping device used to produce the c_{NS} and c_{PS} damping coefficients

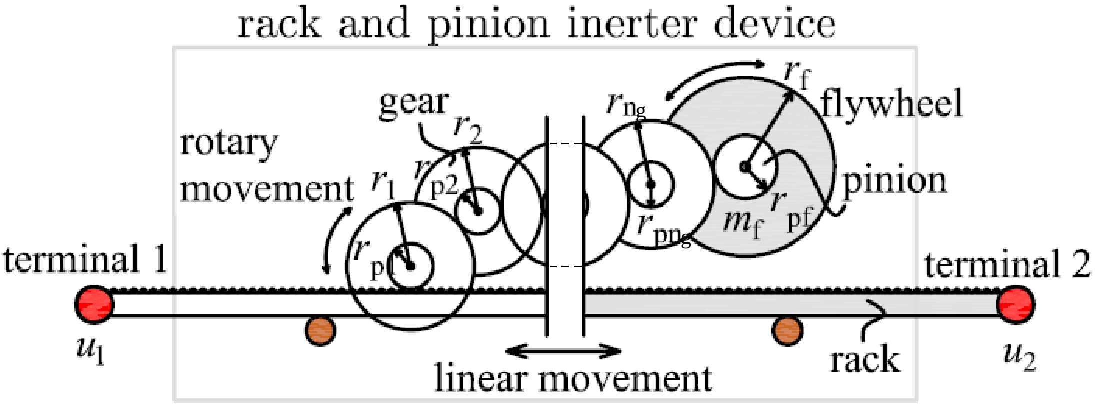

Figure 6.17: Rack and pinion inerter device used to generate the inertance of the ESBA-3 configuration

7 CONCLUSIONS AND FUTURE WORK

7.1 Summary-conclusions

This postgraduate thesis introduces several variations of the Stiff Base Absorber system, which is based on the KDamper concept, by incorporating inerter elements at different locations. The optimal parameters for each system are determined through an optimization process, considering engineering criteria and constraints. These dynamic vibration absorbers, which will be referred to hereafter as extended seismic base absorbers (ESBA), are designed with an additional constraint, that of an acceleration filter to assess the system’s efficiency. The selection of optimal parameters is based on the maximum structure acceleration, expressed as a percentage of the peak ground acceleration (PGA). A database of artificial accelerograms, compatible with EC8 response spectra, is generated to define the ground motion input in the optimization process. Real earthquake records are then utilized to evaluate the dynamic behavior of the single-degree-of-freedom (SDOF) system, comparing it to a conventional low and high damping base isolation. The most effective vibration control system is further extended for implementation as a stiff seismic base absorber for multi-story structures, with system parameters determined through the optimization process, previously stated for a SDOF system. The dynamic responses of a three-story and a five-story building, modeled as shear frames, are compared under different scenarios, initially fixed base, placed on the proposed vibration absorption base, and contrasted with the low and the high damping conventional base isolations approaches of the same or different natural frequency. The efficiency of the proposed extended stiff seismic base absorber is demonstrated by subjecting the multi-degree-of-freedom (MDOF) buildings to both artificial and real near-fault and far-fault earthquake excitations. Sensitivity analyses are conducted to investigate the system's vulnerability to detuning phenomena by varying one parameter at a time and two parameters simultaneously. Additionally, the thesis explores a realistic displacement-dependent configuration for the negative stiffness (NS) element and compares the nonlinear dynamic behavior of the system with the initially expected linear response. Finally, an indicative design of the proposed vibration absorption system is provided, regarding its comprising elements.

Based on the yielded results and the dynamic responses obtained, a multitude of remarks can be made:

- All the ESBA configurations are realistically designed, as they incorporate an additional mass of relatively low value and they predict a variation of all the consisting stiffness elements.
- The optimal system parameters are selected based on engineering criteria with proper constraints and limitations, which lead to a realizable design within technological capabilities.
- All the ESBA systems are designed according to seismic codes, as the input ground excitation comes from a database of artificial accelerograms that are compatible with the EC8 response spectra.
- From all the proposed extended stiff base seismic absorbers, the ESBA-3 configuration, with the largest imposed limit of the inerter element ($b_{max} =$

0.5), proved to be the most efficient in terms of the structure's displacement and the NS stroke, for the most of the values of the acceleration filters (expressed as % of the PGA).

- Very important is the fact that the addition of the inerter parallel to the positive stiffness element (k_{PS}) has little to no contribution to the highest acceleration filters, since its value is zero, for the ESBA-3 configuration and from this point the two proposed systems (ESBA-1 and ESBA-3) coincide together, in terms of the dynamic responses.
- The SDoF system controlled with ESBA-3 manages to retain the structure absolute acceleration and base shear at acceptable levels, while at the same time the structure relative displacement is significantly low, compared to the conventional base isolation.
- The superstructure dynamic behavior of the examined three-story building controlled with ESBA-3 is greatly improved. More specifically, the structure's relative to the ground displacement is the lowest, compared to the fixed structure and the high damping isolation base. Regarding the absolute acceleration and the base shear, ESBA-3 maintains those values at acceptable levels and is in fact, very close to the corresponding values of the high damping base isolation system. The first floor drifts are drastically improved and again ESBA-3 exhibits a similar behavior to that of the high damping BI. Finally, the base displacement is dramatically lower compared to that of the BI and HDBI (below of 4 cm, in contrast with the 17 cm (approximately) of the BI for the artificial acceleration), while the NS stroke is observed to remain to quite reasonable ranges of a few centimeters.
- The decrease of the base isolation's natural frequency, in an attempt to enhance its behavior, leads to a considerable increase of the structure's relative displacement and base displacement (27.4 cm and 26.5 cm), which becomes problematic compared to the corresponding dynamic responses of the ESBA-3 configuration.
- By analogically altering the optimal values of the ESBA-3 system, with respect to the total superstructure mass, the same exact behavior in terms of the dynamic responses of the five-story building structure is exhibited. Again, the ESBA-3 is a suitable seismic stiff base absorber.
- From the uniparametric and biparametric sensitivity analyses, it seems that the ESBA-3 configuration is not sensitive to detuning phenomena.
- The displacement-dependent configuration for the realization of the NS stroke, for various values of the c_I parameter, yielded a nonlinear behavior that proved to be equivalent to the initially defined linear problem.
- The imposed constraints led to the realization of all the parameters/elements/components within reasonable technological capabilities. Thus, the implementation of the ESBA-3 configuration is feasible by utilizing conventional structural elements. In this way, retrofitting is possible.

7.2 Future work

The content of this thesis sought to investigate several topics in terms of the vibration absorption systems. However, there are also topics that were not addressed. The following are research directions that can greatly extend the present work:

- The investigation of alternative realistic configurations for the realization of the negative stiffness element and the inerters using conventional structural elements that can generate the required elastic and inertial forces, specifically in relation to their applications in Civil Engineering structures.
- Employing commercial Finite Element software to evaluate the aforementioned applications. The simulations should incorporate realistic constitutive models for both the superstructure and the components of the proposed vibration absorbers. In the present work, linear models are used for the modelling of all the examined applications, with the exception of the geometric nonlinearity for the realization of the negative stiffness element. Material nonlinearity should also be considered for the superstructure modelling, in case of extreme earthquake excitations.
- Conducting experiments on realistic scaled structural systems to validate the proposed dynamic vibration absorbers for seismic protection. The experiments should involve the implementation of simple configurations with pre-compressed springs to achieve the negative stiffness element and flywheel-based mechanical inerters to achieve inertance.
- Assessing the feasibility of implementing the proposed dynamic vibration absorbers as viable retrofitting solutions for existing building structures, while considering the impact of soil-structure interaction effects.

REFERENCES

Alia, O. M., & Mandava, R. (2011). The variants of the harmony search algorithm: an overview. *Artificial Intelligence Review, 36*(1), 49-68. Retrieved from https://doi.org/10.1007/s10462-010-9201-y

Antoniadis, I. A., Kanarachos, S. A., Gryllias, K., & Sapountzakis, I. E. (2018). KDamping: A stiffness based vibration absorption concept. *Journal of Vibration and Control, 24*(3), 588-606. doi:10.1177/1077546316646514

Attary, N., Symans, M., & Nagarajaiah, S. (2015). Development of a rotation-based negative stiffness device for seismic protection of structures. *Journal of Vibration and Control, 23*(5), 853-867. doi:10.1177/1077546315585435

Budynas, G. R., & Keith, N. J. (2011). *Shigley's Mechanical Engineering Design.* New York, NY: McGraw-Hill.

Carrella, A., Brennan, M., & Waters, T. (2007). Static analysis of a passive vibration isolator with quasi-zero-stiffness characteristic. *Journal of Sound and Vibration, 301*(3), 678-689. doi:https://doi.org/10.1016/j.jsv.2006.10.011

Chopra, A. K. (2011). *Dynamics of Structures Theory and Applications to Earthquake Engineering (Fourth eDition).* Pearson.

De Angelis, M., Giannini, R., & Paolacci, F. (2010). Experimental investigation on the seismic response of a steel liquid storage tank equipped with floating roof by shaking table tests. *Earthquake Engineering & Structural Dynamics, 39*(4), 377-396. doi:https://doi.org/10.1002/eqe.945

De Domenico, D., & Ricciardi, G. (2018). Improving the dynamic performance of base-isolated structures via tuned mass damper and inerter devices: A comparative study. *Structural Control and Health Monitoring, 25*(10), e2234. doi:https://doi.org/10.1002/stc.2234

De Domenico, D., Impollonia, N., & Ricciardi, G. (2018). Soil-dependent optimum design of a new passive vibration control system combining seismic base isolation with tuned inerter damper. *Soil Dynamics and Earthquake Engineering, 105*(37), 37-53. doi:https://doi.org/10.1016/j.soildyn.2017.11.023

De Domenico, D., & Ricciardi, G. (2018). An enhanced base isolation system equipped with optimal tuned mass damper inerter (TMDI). *Earthquake Engineering & Structural Dynamics, 47*(5), 1169-1192. doi:https://doi.org/10.1002/eqe.3011

Den Hartog, J. P. (1956). *MECHANICAL VIBRATIONS.* New York, Toronto, London: McGRAW-HILL BOOK COMPANY.

Dong, L., & Lakes, R. (2013). Advanced damper with high stiffness and high hysteresis damping based on negative structural stiffness. *International Journal of Solids and Structures, 50*(14), 2416-2423. doi:https://doi.org/10.1016/j.ijsolstr.2013.03.018

Dyskin, A. V., & Pasternak, E. (2012). Mechanical effect of rotating non-spherical particles on failure in compression. *Philosophical Magazine, 92*(28-30), 3451-3473. doi:10.1080/14786435.2012.704421

EN 1992-1-1, E. C. (2004). *Eurocode 2: Design of concrete structures - Part 1-1 : General rules and rules for buildings.* Brussels: CEN.

EN 1998-1, E. C. (2004). *Eurocode 8: Design of structures for earthquake resistance -Part 1 : General rules, seismic actions and rules for buildings.* Brussels: CEN.

Fenz, D. M., & Constantinou, M. C. (2006). Behaviour of the double concave Friction Pendulum bearing. *Earthquake Engineering & Structural Dynamics, 35*(11), 1403-1424. doi:https://doi.org/10.1002/eqe.589

FIP INDUSTRIALE. (2010, July). ELASTOMERIC ISOLATORS series SI. Italy. Retrieved from https://www.elemka.gr/media/lggdgyzv/fip_si.pdf

FRAHM, H. (. (1911, April). *USA Patent No. 0989958.* Retrieved from https://www.freepatentsonline.com/0989958.html

Geem, Z. W., Kim, J. H., & Loganathan, G. (2001). A New Heuristic Optimization Algorithm: Harmony Search. *SIMULATION, 76*(2), 60-68. doi:10.1177/003754970107600201

Haskett, T., Breukelman, B., Robinson, J., & Kottelenberg, J. (2003). Tuned mass dampers under excessive structural excitation. *Report of the Motioneering Inc.* Retrieved from https://www.researchgate.net/publication/266094150_Tuned_mass_dampers_under_excessive_structural_excitation

Ibrahim, R. (2008). Recent advances in nonlinear passive vibration isolators. *Journal of Sound and Vibration, 314*(3), 371-452. doi:https://doi.org/10.1016/j.jsv.2008.01.014

ITT ENIDINE Inc. (2020, September 3). Infrastructure Products. New York, USA. Retrieved from https://www.enidine.com/CorporateSite/media/itt/Resources/TechnicalData/Seismic_Products_Catalog.pdf?ext=.pdf

Jaglinski, T., Kochmann, D., Stone, D., & Lakes, R. (2007). Composite Materials with Viscoelastic Stiffness Greater Than Diamond. *Science, 315*(5812), 620-622. doi:10.1126/science.1135837

Kalogerakou, M. E., Kapasakalis, K. A., Antoniadis, I. A., & Sapountzakis, E. J. (2023). Vertical seismic protection of structures with inerter-based negative stiffness absorbers. *Bulletin of Earthquake Engineering, 21*(3), 1439-1480. doi:10.1007/s10518-021-01284-w

Kampitsis, A., Kapasakalis, K., & Via-Estrem, L. (2022). An integrated FEA-CFD simulation of offshore wind turbines with vibration control systems. *Engineering Structures, 254*, 113859. doi:https://doi.org/10.1016/j.engstruct.2022.113859

Kangda, M. Z., & Bakre, S. (2020). Performance Evaluation of Moment-Resisting Steel Frame Buildings Under Seismic and Blast-Induced Vibrations. *Journal of Vibration Engineering & Technologies, 8*(1), 1-26. doi:10.1007/s42417-018-0027-2

Kapasakalis, A. K. (2020). *Dynamic vibration absorbers in civil engineering structures [Doctoral dissertation, National Technical University of Athens].* Athens: National Technical University of Athens Digital Respiratory. Retrieved from https://dspace.lib.ntua.gr/xmlui/handle/123456789/50866

Kapasakalis, K. A., & Sapountzakis, E. J. (2022). Vibration Absorption using KDamper-based Devices with Extreme Geometric Nonlinearity,. *International Journal of Mechanics, 16*, 15-27. doi:10.46300/9104.2022.16.3

Kapasakalis, K. A., Alamir, C.-H. T., Antoniadis, I. A., & Sapountzakis, E. J. (2021). Frequency-Based Design of the KDamper Concept for Seismic Isolation of Bridges. *Proceedings of the 14th International Conference on Vibration Problems* (pp. 169-191). Singapore: Springer Nature Singapore. doi:https://doi.org/10.1007/978-981-15-8049-9_11

Kapasakalis, K. A., Alvertos, A. E., Antoniadis, I. A., & Sapountzakis, E. J. (2022). A negative stiffness dynamic base absorber for seismic retrofitting of residential buildings. *Structural Control and Health Monitoring, 29*(12), e3127. doi:https://doi.org/10.1002/stc.3127

Kapasakalis, K. A., Antoniadis, I. A., & Sapountzakis, E. J. (2019). CONTROL OF MULTI STOREY BUILDING STRUCTURES WITH A NEW PASSIVE VIBRATION CONTROL SYSTEM COMBINING BASE ISOLATION WITH KDAMPER. *Proceedings of the 7th international conference on computational methods in structural dynamics and earthquake engineering (COMPDYN 2019)*, (pp. 5223-5235).

Kapasakalis, K. A., Antoniadis, I. A., & Sapountzakis, E. J. (2019). Implementation of the KDamper as a Stiff Seismic Absorption Base: A Preliminary Assessment. *Vibration and Acoustics Research Journal, 1*(1), 1-26. Retrieved from https://www.cansrg.com/journals/varj/2019/69/

Kapasakalis, K. A., Antoniadis, I. A., & Sapountzakis, E. J. (2019). Performance assessment of the KDamper as a seismic Absorption Base. *Structural Control and Health Monitoring, 27*(4), e2482. doi:https://doi.org/10.1002/stc.2482

Kapasakalis, K. A., Antoniadis, I. A., & Sapountzakis, E. J. (2021). A Soil-Dependent Approach for the Design of Novel Negative Stiffness Seismic Protection Devices. *Applied Sciences, 11*(14), 1-18. doi:10.3390/app11146295

Kapasakalis, K. A., Antoniadis, I. A., & Sapountzakis, E. J. (2021). Constrained optimal design of seismic base absorbers based on an extended KDamper concept. *Engineering Structures, 226*, 111312. doi:https://doi.org/10.1016/j.engstruct.2020.111312

Kapasakalis, K. A., Antoniadis, I. A., & Sapountzakis, E. J. (2021). STIFF vertical seismic absorbers. *Journal of Vibration and Control, 28*(15-16), 1937-1949. doi:10.1177/10775463211001624

Kapasakalis, K. A., Antoniadis, I. A., Sapountzakis, E. J., & Kampitsis, A. E. (2021). Vibration Mitigation of Wind Turbine Towers Using Negative Stiffness Absorbers. *Journal of Civil Engineering and Construction, 10*(3), 123-139. doi:https://doi.org/10.32732/jcec.2021.10.3.123

Kapasakalis, K., Antoniadis, I., & Sapountzakis, E. (2019). Novel vibration absorption systems with negative stiffness elements for the seismic protection of structures. *4th National Conference on Earthquake Engineering and Engineering Seismology (Hellenic Association for Earthquake Engineering - HAEE / ETAM), 2019.*

Kapasakalis, K., Antoniadis, I., & Sapountzakis, E. (2022). Feasibility Assessment of Stiff Seismic Base Absorbers. *Journal of Vibration Engineering & Technologies, 10*(1), 37-53. doi:10.1007/s42417-021-00362-2

Katsikadelis, J. T. (2020). *Dynamic Analysis of Structures.* Cambridge, MA: Academic Press.

Kelly, J. M. (1986). Aseismic base isolation: review and bibliography. *Soil Dynamics and Earthquake Engineering, 5*(4), 202-216. doi:https://doi.org/10.1016/0267-7261(86)90006-0

Kelly, J. M. (1999). The role of damping in seismic isolation. *Earthquake Engineering & Structural Dynamics, 28*(1), 3-20. doi:https://doi.org/10.1002/(SICI)1096-9845(199901)28:1<3::AID-EQE801>3.0.CO;2-D

Kunde, M., & Jangid, R. (2003). Seismic behavior of isolated bridges: A-state-of-the-art review. *Electronic Journal of Structural Engineering, 3*, 140-170. doi:10.56748/ejse.335

Lakes, R. (2001). Extreme Damping in Composite Materials with a Negative Stiffness Phase. *Physical Review Letters, 86*(13), 2897-2900. doi:10.1103/PhysRevLett.86.2897

Lee, C., & Goverdovskiy, V. (2012). A multi-stage high-speed railroad vibration isolation system with “negative” stiffness. *Journal of Sound and Vibration, 331*(4), 914-921. doi:https://doi.org/10.1016/j.jsv.2011.09.014

Lee, K. S., & Geem, Z. W. (2004). A new structural optimization method based on the harmony search algorithm. *Computers & Structures, 82*(9), 781-798. doi:https://doi.org/10.1016/j.compstruc.2004.01.002

Molyneux, W. (1957). *Supports for Vibration Isolation, C.P. No. 322 .* London: MINISTRY OF SUPPLY .

Naeim, F., & Kelly, J. (1999). *Design of Seismic Isolated Structures: From Theory to Practice.* New York: John Wiley & Sons.

Nagarajaiah, S., Pasala, D. T., Reinhorn, A., Constantinou, M., Sirilis, A. A., & Taylor, D. (2013). Adaptive Negative Stiffness: A New Structural Modification Approach for Seismic Protection. *Advanced Materials Research, 639-640*, 54-66. doi: 10.4028/www.scientific.net/AMR.639-640.54

Newmark, N. M. (1959). A Method of Computation for Structural Dynamics. *Journal of the Engineering Mechanics Division, 85*(3), 67-94. doi: 10.1061/JMCEA3.0000098

Paolacci, F., Giannini, R., & De Angelis, M. (2013). Seismic response mitigation of chemical plant components by passive control techniques. *Journal of Loss Prevention in the Process Industries, 26*(5), 924-935. doi:https://doi.org/10.1016/j.jlp.2013.03.003

Platus, D. L. (1992). Negative-stiffness-mechanism vibration isolation systems. *Proc.SPIE, 1619*, 44-54. doi:10.1117/12.56823

Qiao, H., Huang, P., De Domenico, D., & Wang, Q. (2022). Structural control of high-rise buildings subjected to multi-hazard excitations using inerter-based vibration absorbers. *Engineering Structures, 266*, 114666. doi:https://doi.org/10.1016/j.engstruct.2022.114666

Reggio, A., & Angelis, M. D. (2015). Optimal energy-based seismic design of non-conventional Tuned Mass Damper (TMD) implemented via inter-story isolation. *Earthquake Engineering & Structural Dynamics, 44*(10), 1623-1642. doi:https://doi.org/10.1002/eqe.2548

Robertson, W. S., Kidner, M., Cazzolato, B. S., & Zander, A. C. (2009). Theoretical design parameters for a quasi-zero stiffness magnetic spring for vibration isolation. *Journal of Sound and Vibration, 326*(1), 88-103. doi:https://doi.org/10.1016/j.jsv.2009.04.015

Smith, M. (2002). Synthesis of mechanical networks: the inerter. *IEEE Transactions on Automatic Control, 47*(10), 1648-1662. doi:10.1109/TAC.2002.803532

Symans, M., Charney, F., Whittaker, A., Constantinou, M., Kircher, C., Johnson, M., & McNamara, R. (2008). Energy Dissipation Systems for Seismic Applications: Current Practice and Recent Developments. *Journal of Structural Engineering, 134*(1), 3-21. doi:10.1061/(ASCE)0733-9445(2008)134:1(3)

The MathWorks Inc. (2022). MATLAB version: 9.13.0 (R2022b). Natick, Massachusetts, United States. Retrieved from https://www.mathworks.com

Virgin, L., Santillan, S., & Plaut, R. (2008). Vibration isolation using extreme geometric nonlinearity. *Journal of Sound and Vibration, 315*(3), 721-731. doi:https://doi.org/10.1016/j.jsv.2007.12.025

Warn, G. P., & Ryan, K. L. (2012). A Review of Seismic Isolation for Buildings: Historical Development and Research Needs. *Buildings, 2*(3), 300-325. doi:10.3390/buildings2030300

WHITTAKER, A. S., & KUMAR, M. (2014). SEISMIC ISOLATION OF NUCLEAR POWER PLANTS. *Nuclear Engineering and Technology, 46*(5), 569-580. doi:https://doi.org/10.5516/NET.09.2014.715

Winterflood, J., Blair, D., & Slagmolen, B. (2002). High performance vibration isolation using springs in Euler column buckling mode. *Physics Letters A, 300*(2), 122-130. doi:https://doi.org/10.1016/S0375-9601(02)00258-X

Zhou, J., Xu, D., & Bishop, S. (2015). A torsion quasi-zero stiffness vibration isolator. *Journal of Sound and Vibration, 338*, 121-133. doi:https://doi.org/10.1016/j.jsv.2014.10.027

Zhou, N., & Liu, K. (2010). A tunable high-static–low-dynamic stiffness vibration isolator. *Journal of Sound and Vibration, 329*(9), 1254-1273. doi:https://doi.org/10.1016/j.jsv.2009.11.001